The Phonon Entropy of Metals and Alloys: The effects of thermal and chemical disorder

Thesis by

Peter David Bogdanoff

In Partial Fulfillment of the Requirements
for the Degree of
Doctor of Philosophy

California Institute of Technology
Pasadena, California

2001
(Submitted November 30, 2001)

Acknowledgements

I would like to thank my advisor, Brent Fultz, for his encouragement, support and outstanding research group. I count myself fortunate beyond words for having Brent as a research advisor and intellectual collaborator these many years. I also owe an enduring debt to those in whose research footsteps I followed: Lawrence Anthony, Laura Nagel and Heather Frase being chief among these at Caltech.

My research would not have been possible without the help and wisdom of our many collaborators at Argonne and Oak Ridge national labs: Stefan Rosenkranz, Ray Osborn and Lee Robertson. In addition, I owe much to the many people at Caltech who helped with experiments over the years: Channing Ahn, Tab Stephens, Carol Garland, Chuck Witham, Stephen Glade, Adrian Hightower, Andy Waniuk and many others who I have undoubtedly forgotten. Many thanks to my colleague Mike Manley, who contributed much to my understanding of vibrational entropy.

My thanks and best wishes to Alexander Papandrew, Olivier Delaire and Tabitha Swan-Wood for showing an interest in phonons and for many interesting discussions this past year. Good luck!

I would like to thank my long time friend and co-conspirator Adrian Hightower, as well as Stephen Glade, Ben Shapiro, Jason Graetz and others for keeping me sane and productive over the years. Many thanks to Heather Frase for introducing me to swing dancing. To my Harvey Mudd friends: Daniel "Hole" Hyman, Adam "Lithuanian High Command" Rakunas, John "Trager" Trager, Paul "Leo" Parker, Ben Melhuish and many others who I best not identify by name.

To my friend Jeffrey Drummond I offer my heartfelt appreciation and gratitude for his support over the years. I am in your debt.

Lastly, a real special thanks to neutrons 27,890–94,051. These guys did all the real work.

Abstract

Vibrational entropy is important for the thermodynamics of alloying, alloy formation, phase transitions and phase stability at high temperature. Vibrational entropies of alloying and alloy formation were calculated for 32 binary alloys and intermetallic compounds using phonon DOS curves taken from the literature. The vibrational entropies of formation span a wide range from -0.64 to $+0.55$ k_B/atom, and the vibrational entropies of alloying ranged from -0.39 to $+1.0$ k_B/atom. This range exceeds the range of configurational entropy of a binary alloy, which reaches a maximum value of $+0.69$ k_B/atom and a minimum value of 0 k_B/atom.

The vibrational entropy of the NiTi martensitic transition was measured using low-temperature calorimetry and inelastic neutron-scattering. The high-temperature B2 phase of NiTi has a vibrational entropy 0.5 k_B/atom larger than the low-temperature martensitic phase. The difference in vibrational entropy accounts for the total entropy of the austenitic-martensitic phase transition.

Inelastic neutron scattering was used to show that the phonon DOS of V is unchanged between 20 and 1000 °C, inconsistent with the phonon softening expected from thermal expansion. It is found that the effects of volume expansion and rising temperature exert equal and opposite shifts on the phonon DOS. The pure temperature dependence of the phonon DOS is due to strong phonon-phonon scattering, which in turn leads to a large *anharmonic* vibrational entropy contribution at high temperature.

The vibrational entropy of eight chemically disordered Cu-Au alloys was measured using inelastic neutron scattering. The analysis of the phonon entropy of a disordered alloy was performed in a novel way by modeling the partial vibrational entropies of Cu and Au. The partial vibrational entropies of Cu and Au were shown to be slowly varying and smooth functions of composition. The vibrational entropy of disordering in Cu_3Au is calculated as 0.24 ± 0.02 k_B/atom, substantially larger than results

predicted from recent theoretical work.

Contents

List of Figures

List of Tables

Chapter 1 Introduction

1.1 Overview

The measurement and prediction of thermodynamic equilibrium in the solid state is one of the enduring scientific goals of materials science and condensed matter physics. Measuring thermodynamic equilibrium is the everyday work done in characterising new materials: atomic positions and crystal structure are determined by diffraction, microstructural features through electron miscroscopy. Predicting thermodynamic equilibrium has historically been the work of theory and theorists; the minimization of the free energy function with respect to atomic position is the ultimate goal. Much progress has been made towards this goal in the last few decades; the advent of fast, cheap computation has been crucial in this regard. The free energy function has two discrete terms: energy and entropy. The free energy function, F, can be calculated with

$$F = E - TS \tag{1.1}$$

where E is the internal energy, T is the temperature and S is the entropy.

The energy term can now be calculated, in the ground state at zero temperature, for near arbitrary atomic positions. The entropy terms, however, are less well characterised. There are many different possible sources of entropy in a solid: electronic, magnetic, configurational and vibrational:

$$S = S_{\text{electronic}} + S_{\text{magnetic}} + S_{\text{configurational}} + S_{\text{vibrational}} \tag{1.2}$$

More esoteric sources exist, but the ones listed are typically the important ones in metals. Of the four, the electronic and configurational entropies are well understood and accessible through calculation. The magnetic entropy is of importance only in

the handful of materials that exhibit magnetic order. The vibrational entropy is ubiquitous, very difficult to predict computationally and also quite hard to measure experimentally. Ironically, the vibrational entropy comprises most of the entropy of a solid, yet historically is the least well understood.

Some progress has been made in our understanding of the vibrational entropy of materials. Grimvall and J. Rosén have shown that calorimetric entropy differences between TiC, ZrC and HfC are explained entirely by the mass differences of the constituent metals [2]. Langeveld and Niemantsverdriet showed that segregation of Pt to the surface of a bulk Pt-Rh alloy was accounted for by the large vibrational entropy difference between bulk and surface Pt [3]. Clark and Ackland calculated the effect of vacancies and interstitial atoms on the vibrational entropy of silicon [4].

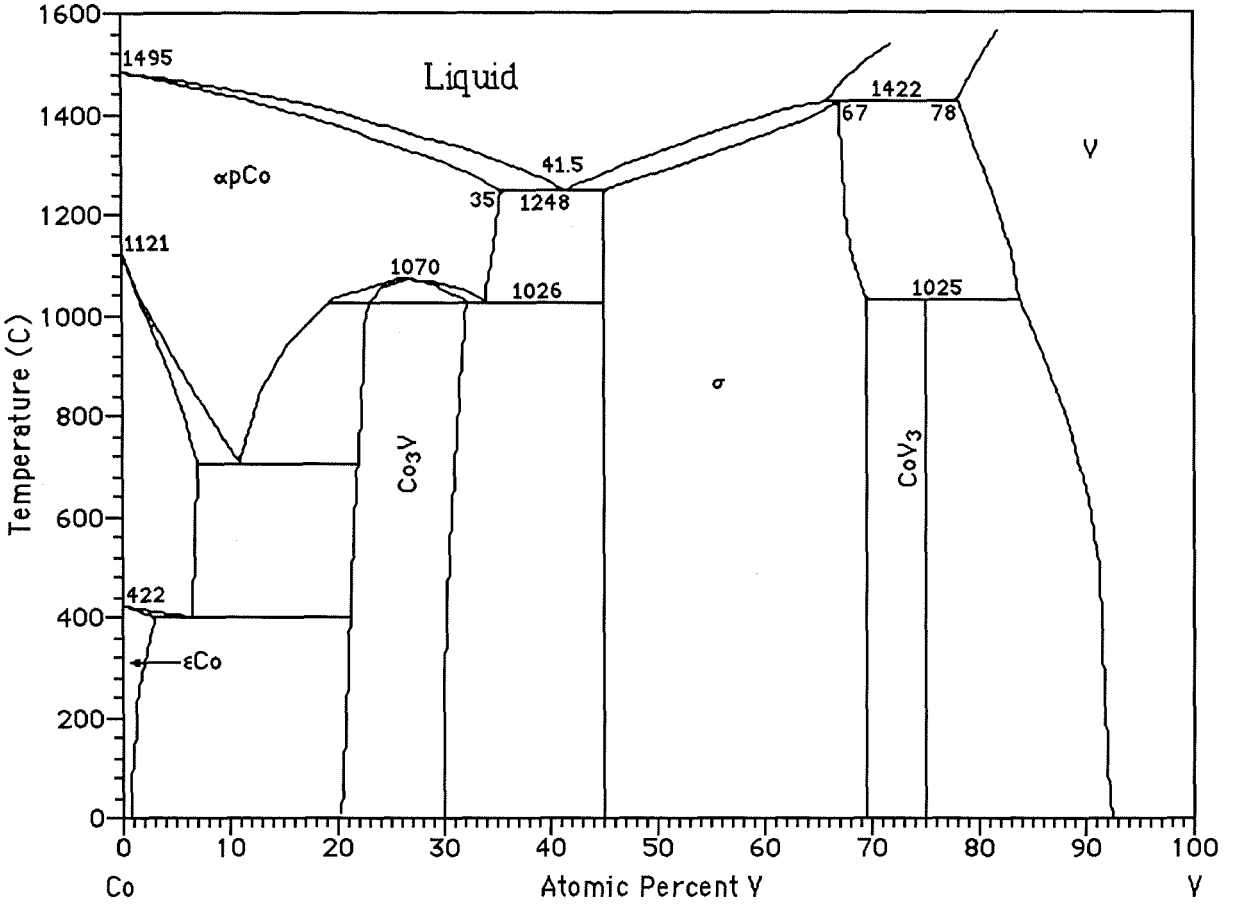

Figure 1.1: Phase diagram of the Co-V alloy system.

The entropy is of special interest in the calculation of alloy phase diagrams. In

figure 1.1 we show the alloy phase diagram for the Co-V system [5]. The solubility of Co in bcc V rises from 8% at ambient to 15% at 1000 °C. The configurational entropy, in the absence of short-range order, averages 0.35 k_B/atom in this concentration range. The contribution to the free energy is arrived at using equation 1.1. We calculate a configurational free energy of −900 J/mol at room temperature and −3700 J/mol at 1000 °C. Clearly, the fourfold increase in the free energy contribution at 1000 °C is responsible for the greater solubility at higher temperature. We arrive at this conclusion by noting that the bcc V solid solution phase competes with the CoV_3 phase up to 1000 °C. For a given temperature and total composition, the relative amounts of bcc V and CoV_3 are determined by the choice that minimizes the total free-energy, F_{total}. The quantity F_{total} is the sum of the free-energies of the two phases

$$F_{total} = F_{bccV} + F_{CoV_3} \tag{1.3}$$

The F_{bccV} term has an entropy contribution that the CoV_3 phase lacks: the configurational entropy. The CoV_3 phase is a stoichiometric intermetallic compound, and thus lacks the configurational degrees of freedom. As the temperature rises, the greater total entropy of the bcc V phase becomes a more important term to the total free energy, and the free energy minimum moves in the direction of more bcc V phase.

Although it is likely that the vibrational entropy as a function of Co concentration contributes to the rising solubility of Co in bcc V, the effect is masked by the configurational entropy. A clear example of the effects of vibrational entropy are in the allotropes of elemental Co. Co undergoes a transition from hcp to fcc crystal structure at 422 °C. The free-energy difference between the two phases must be zero at this temperature, T_c.

$$\Delta F = 0 = \Delta E - T_c \Delta S \tag{1.4}$$

where ΔE is the internal energy difference between the two allotropes and ΔS is the entropy difference between the two allotropes. The energy difference is well understood: the two phases have distinct crystal structures, and therefore different

electronic band structures and total electronic energies. The source of the entropy difference can be arrived at by elimination. Elemental crystalline solids have no configurational entropy, and the magnetic entropy difference is zero since both phases are ferromagnetic. Electronic entropies of transition metals are small at moderate temperatures, typically 1 to 10% of the size of the vibrational entropies. Thus, we expect the electronic entropy difference between the two phases to be small and unable to account for all the entropy of the phase transition. The only possible remaining source of the entropy difference between the phases is vibrational.

The entropy of solid state allotropic phase transitions has attracted much recent interest. Inelastic neutron scattering and calorimetric measurements on Ce showed that the allotropic $\beta - \gamma$ phase transition has a vibrational entropy contribution that accounts for 65% of the total entropy difference [6]. In chapter 3 we show that vibrational entropy accounts for the entire entropy of the ambient martensite transition in NiTi, to within experimental error. At higher temperatures, the electronic entropy can equal the vibrational contribution. Electronic band-structure calculations show that the electronic entropy accounts for 63% and 40% of the hcp-bcc phase transitions in Ti and Zr, respectively [7]. More recent calculations by Moroni, Grimvall and Jarlborg [8] claim the electronic entropy accounts for over 90% of the transition entropy in both these cases. However, the same work show that the high temperature hcp-bcc phase transitions in Sc and Y have electronic entropy differences that accounts for only 32% and 50% of the total entropy, respectively. In the high temperature $\gamma - \delta$ transition in Ce, recent measurements [6] show that the vibrational entropy difference is almost twice as large as the total transition entropy. The electronic entropy difference must be half as large and with the opposite sign in order to account for the measured total entropy.

Allotropic phase changes are an example of first-order phase transitions. First order phase transitions follow the relationship between energy differences, entropy differences and transition temperature shown in equation 1.4. Given a fixed energy difference, the exact value for ΔS is said to determine the transition temperature, T_c. Including the vibrational entropy in phase diagram calculations should lead to better

agreement with experiment and measured transition temperatures. The effect of lattice vibrations improved the agreement between predicted and experimental values of the solubility of Sc in Al [9]. On the other hand, agreement between predicted and experimental values of the order-disorder transition temperatures in Cu-Au alloys worsen when vibrational effects are included [10]. In this case, the lack of agreement with experiment is indicative of our continuing poor methodology for calculating the energies and entropies of the chemically disordered solid.

1.2 Experimental Methods

1.2.1 Calorimetry

Calorimetric data are indispensable in any thermodynamic study. Heat capacity measurements and their corresponding entropies are regarded as the most reliable direct measurements of thermodynamic quantities. However, there exists no way to separate the differing contributions to the heat capacity from all the internal degrees of freedom. Thus, although one can measure the calorimetric entropy of a solid very accurately, one cannot separate the vibrational entropy from the electronic, magnetic and ordering contributions. Vibrational entropies derived from calorimetric studies suffer from both the uncertainty of the measurement and the difficulty in ascertaining other contributions to the entropy. In many cases, the latter overwhelm the former. Calorimetric data is a useful piece of the entropic puzzle, but it fails to give the entire picture.

1.2.2 Inelastic Neutron Scattering

Inelastic neutron scattering provides us with the most direct measurement of the lattice entropy of a solid. Knowledge of the lattice-dynamical excitations of a crystalline solid together with the use of statical mechanics is sufficient to derive the vibrational entropy. The use of neutron scattering allows us to isolate the lattice contribution specifically. However, the accuracy of the derived entropy depends greatly on how

accurately one can measure the vibrational excitations of the solid. In turn, these depend on how well the sample scatters neutrons and the type of neutron spectrometer used. These factors are given further consideration below.

Incoherent and Coherent Scattering

Neutrons can scatter from a solid coherently or incoherently. The former preserves phase between the initial and scattered neutron waves; the latter does not. An important consequence of this distinction is that Bragg peaks are observed only from coherently scattered neutrons. Coherent inelastic scattering occurs when the change in neutron wavevector equals the wavevector of the dynamic excitation in the sample: magnetic, vibrational or otherwise. Incoherent inelastic scattering, on the other hand, has no such conservation. The vibrational entropy can be calculated from measurements of either the incoherent or coherently scattered neutron cross-section. The former is most easily performed using a triple-axis neutron spectrometer and involves no approximations in the data analysis. This technique is unfeasible when the sample exhibits significant coherent scattering. The latter demands the use of a time-of-flight (TOF) neutron spectrometer and involves a number of approximations in the data analysis. As a side note, these approximations can be eliminated by using a lattice dynamics model to interpret the raw data. However, current generation TOF instruments lack the neutron flux and spectrometer resolution to make this a feasible option. The TOF spectrometer method is also appropriate for samples that have significant incoherent scattering.

In theory, every element exhibits some coherent and some incoherent scattering. Practically, most elements, in their naturally found isotopic proportions, exhibit a signicant amount of coherent scattering (see Table 1.1). Therefore, with the exception of a handful of elements and almost no alloys, most materials require time on a TOF neutron spectrometer for measurements of the vibrational entropy. Chapters 3 and 5 both contain measurements done on a TOF neutron spectrometer. Chapter 4 contains measurements on elemental vanadium done on a triple-axis spectrometer.

Element	cross-section (10^{-24}cm^2)	
	coherent	incoherent
Ti	1.48	2.71
V	0.02	5.08
Cr	1.66	1.83
Mn	1.75	0.4
Fe	11.22	0.4
Co	0.78	4.8
Ni	13.3	5.2
Cu	7.48	0.55

Table 1.1: Thermal neutron scattering cross-section of $3d$-transition metals.

Variation in Elemental Scattering Cross-Section

Additional difficulties arise for samples containing more than one element. Differing elements have differing total neutron scattering cross-sections; Ni and Al have, respectively, cross-sections of 18 and 1.3 barns. Individual lattice-dynamical excitations (phonons) scatter neutrons with an efficiency proportional to the quotient of cross-section and atomic mass of the atoms undergoing displacement during the excitation. Practically speaking, this means that the phonons that displace the species with larger cross-sections and samller masses give a much greater signal than the phonons that displace the lesser-scattering elements. The energy spectrum of phonons measured by inelastic neutron scattering is thus weighted by the neutron-scattering cross-sections of the individual atomic species in the sample. This neutron-weighting of the phonon spectrum, or density of states (DOS), prevents a correct derivation of the vibrational entropy. The neutron-weight correction for experimental data is not simple. Chapters 3 and 5 both contain numerous examples of different techniques used to remove the neutron-weighting from the phonon DOS of binary alloy systems. These include using a lattice-dynamical model to fit the neutron-weighted DOS and estimating the element-specific partial DOS from multiple neutron-weighed DOS at similar compositions. These corrections become more elaborate and less reliable for ternary and high-order systems. Chapter 4 contains neutron-scattering data taken from an elemental metal. In this case no neutron-weight correction was needed.

Accounting for the coherent neutron scattering and neutron-weighting of the

phonons is the largest obstacle in any attempt to measure the phonon DOS directly with inelastic neutron scattering. Historically, these obstacles were considered so unmanageable that very few systematic attempts to measure the phonon DOS in coherently scattering multi-atomic systems were made. In part, this thesis deals directly with how to overcome these obstacles, showing in chapters 3 and 5 a consistent methodology for extracting and correcting the neutron-weighted DOS from coherently scattering alloys.

1.3 Anharmonic Entropy

Lattice vibrations are primarily quantum mechanical phenomena at low temperature and classical phenomena at high temperature. The classical nature of phonons at finite temperature is responsible for the existence of a quantity known as anharmonic entropy. Simply put, anharmonic entropy is the entropy due to deviations from harmonicity of the interatomic forces. The cubic and quartic terms in the interatomic forces are responsible for the existence of thermal expansion; the anharmonic entropy has often been loosely defined as the excess vibrational entropy associated with the thermal expansion of the solid. This definition is strictly incorrect because the thermal expansion of the solid accounts for both a volume and a temperature effect on the phonon energies. Furthermore, changes in the electronic entropy with specific volume can also drive thermal expansion. It can be shown that the anharmonic entropy is identified solely with the temperature effect on the phonon energies, to first order.

The relationship between phonon energies and anharmonic interatomic forces is straightforward. Theory tells us that the anharmonic nature of the interatomic forces leads to phonon-phonon scattering [11]. In turn, phonon-phonon scattering leads to shifts in the energies of individual phonon modes. Lastly, phonon-phonon scattering is strongly temperature dependent; at low temperatures few phonons are present so little phonon-phonon scattering occurs, while at high temperatures phonon-phonon scattering is commonplace. This quantum-mechanical viewpoint has a direct classical counterpart; at low temperatures atomic displacements due to vibrations are

low and thus the atoms mostly see harmonic interatomic forces. At high temperatures vibrational displacements are large and atoms see large anharmonic interatomic forces.

By using phonon energies modified by phonon-phonon scattering to calculate the vibrational entropy we can account for the anharmonic contribution. This method is exact to first order in the vibrational entropy [11]. If the anharmonic effects are large and the phonon energy shifts are large, it is unclear how well this method accounts for the anharmonic entropy. Thus, at very high temperatures it is unclear whether using the temperature dependent phonon DOS with the standard formula is sufficient to capture the entire anharmonic contribution to the vibrational entropy. In chapter 4 it is shown that for V the temperature dependent phonon DOS captures the anharmonic contribution to at least 1400 °C.

1.4 Chemically Disordered Materials

The measurement of phonons and phonon entropy in chemically disordered materials continues to be of interest. This interest results from the theoretical and computational difficulties in treating chemically and topologicaly disordered materials. In the absence of adequate theory, experiments assume enormous importance. The difficulty with chemically disordered materials is twofold: lack of translational periodicity and local relaxations. The first removes the wave-vector as a good quantum number for both electronic and vibrational quantum states. Modern *ab-initio* electronic structure computations require a crystal with a translationally-periodic unit cell. In its absence, these computations become unmanageable. Furthermore, the effect of local relaxations compounds the computational difficulties. In a chemically-disordered material, the atomic nuclei deviate from the lattice sites measured by diffraction. These atomic relaxations away from the average lattice sites are a function of the local chemical environment, which is heterogeneous in the presence of chemical disorder. An accurate treatment of local relaxations requires each atom to be moved until the net forces on it are zero. Ideally, the entire crystal would have to be relaxed

simultaneously in order to account for the long range of the forces in metals. This methodology is not possible using the most accurate *ab-inito* calculation codes, which requires days or weeks to calculate the energy of one crystal configuration.

Two theoretical approaches have shown some success in dealing with chemical disorder. The cluster variation method (CVM), refined by Zunger and others [10], was first formulated to calculate the configurational entropy in the presence of short range order [12, 13]. Using this method, the vibrational entropy of a chemically disordered material can be calculated by computing the entropy of a large number of chemically ordered materials. The chemically disordered alloy is then approximated by a suitable average over the ordered materials, taking into account short-range chemical correlations to arbitrary distances. Our measurements of disorderd Cu-Au alloys in chapter 5 show good agreement with this method. The drawback of this method is that the phonon DOS of the disordered material is never computed, only the vibrational entropy and free energy.

The second approach uses special quasi-random structures (SQS) to approximate the disordered material [14]. Using this method, an artificial unit cell (SQS) is constructed that has the property that the resultant crystal has some of the same short-range chemical correlations of the disordered material. The SQS crystal has long-range translation periodicity and is amenable to *ab-initio* computation, unlike the real disordered material. The properties of the SQS crystal are then assumed to be the same as the disordered material. The drawback of this approach is that the SQS crystal matches only a handful of the short-range chemical correlations in the disordered material. It is unclear if the SQS crystal handles local relaxations in the same way as the real disordered material. In contrast, the CVM method can abritrarily extend the range of the chemical correlations that are matched by including more ordered materials in the computation.

Of the two approaches, we prefer the CVM methodology. In chapter 5 we measure the neutron-weighted DOS and vibrational entropy of six chemically disordered Cu-Au alloys and show fair agreement with existing theoretical predictions using CVM.

1.5 Summary

In this chapter we have briefly touched upon the justification, methodology and scientific focus of this thesis. The thermodynamic consequences of the phonon entropy in metals and alloys are enormous, both in size and scope. We further this assertion in chapter 2, where we tabulate the vibrational entropy differences of alloying and formation for 32 alloys and intermetallic compounds. In chapter 3 we demonstrate the largest measured vibrational entropy difference for a polymorphic solid-state phase transition. In chapters 4 and 5 we explore the effects of thermal and chemical disorder in elemental V and Cu-Au alloys.

Chapter 2 Experimental Trends in Vibrational Entropy

2.1 Introduction

There has been a steady growth in our understanding of alloy phase diagrams from ab-initio calculations [15] and more phenomenological approaches [16, 17, 18, 19]. From the work of Ising [20] and Bragg and Williams [21, 22] to the present day, the free energies of alloy phases have been largely understood as an internal energy plus a *configurational entropy* [23, 24, 25, 26, 27, 15]. There were indications that *vibrational entropy* could also be important to alloy phase stability [28, 29, 30, 31, 32, 33] but experimental proof of this has been available only recently [34, 35, 36, 37, 38, 39].

In the harmonic approximation, differences in the phonon density of states (DOS) can be used to identify the reasons for differences in vibrational entropies of alloy phases. There have been recent attempts to calculate the lattice dynamics of intermetallic phases [4, 40, 41, 42] and some alloys were chosen for these calculations in part to provide comparisons with experimental vibrational entropies of order-disorder transformations. The difficulty with such comparisons is calculating the phonon DOS of the disordered alloy. The state of disorder involves chemical and spatial disorder of atoms on crystal lattice sites, and the details of this disorder may differ between experiments and calculations. For example, disordered alloys of Ni_3Al show a wide range of lattice parameters [43, 44, 45, 46], suggesting that Ni_3Al is not a reliable alloy for experimental comparisons.

More reliable comparisons between theory and experiment should be possible with vibrational entropies of formation, defined here as the entropy per mole of the intermetallic compound minus the total vibrational entropy of its two elemental metals. The advantage of studying vibrational entropies of formation is that the unit cells

of both the initial state (two crystalline elemental metals) and the final state (intermetallic compound) are translationally periodic, so well-defined phonon modes exist. An advantage for experimental studies of vibrational entropies of formation is that the lattice dynamics for the phonon DOS should be obtained reliably from coherent neutron inelastic scattering experiments on single crystals. In contrast, coherent neutron inelastic scattering experiments on disordered alloys are typically interpreted with the assumption of a virtual crystal, an assumption that has been shown to be unreliable [38, 47, 41, 42].

Here we report differences in vibrational entropies of formation, ΔS_{vib}^{form} , for intermetallic compounds and alloys in the harmonic approximation. We performed a search of the literature for data on phonon densities of states for alloys and compounds, and their elemental constituents [48, 49, 50, 51, 52, 53, 54, 55, 56, 57]. The vibrational entropies of formation can be large and range from 0.64 to +0.55 k_B/atom. It is interesting that this range is larger than is possible for the range of the configurational entropy of mixing for a binary alloy, $\Delta S_{config}(c)$:

$$\Delta S_{config}(c) = k_B[c \ln c + (1-c)\ln(1-c)] \tag{2.1}$$

which has a maximum value of 0.693 k_B/atom when $c = 0.5$, and has a minimum value of 0.

We attempted many correlations of vibrational entropies of formation to thermophysical properties of the compounds and the constituent elements. Many of the parameters were chosen because of their relationship to the masses of atoms and forces between them, since these masses and forces are the basis for lattice dynamics. Structural differences between phases are also expected to be important, so most systematic comparisons were made within the $L1_2$ and A15 families of compounds. We report a good correlation of the vibrational entropy of formation to the difference in metallic radii of the two species. For the related problem of alloy formation, considered here as substituting solute atoms for atoms of the matrix, we report some success in correlating the vibrational entropy of alloying to the mass ratio of the solute and

matrix atoms.

2.2 Methods and Results

In the high temperature limit, the vibrational entropy of formation can be obtained from the phonon densities of states as

$$\Delta S_{vib}^{form} = -3k_B \int_0^\infty \Delta g(E) \ln(E) dE \tag{2.2}$$

where $\Delta g(E)$ is defined as the difference in phonon DOS of the intermetallic compound, $g(E)$, and the elemental constituents, $g_i(E)$:

$$\Delta g(E) \equiv g(E) - \sum_i f_i \, g_i(E) \tag{2.3}$$

where f_i is the atom fraction of the elemental constituent, i, in the intermetallic compound. The f_i sum to unity. To calculate the vibrational entropy of alloying, ΔS_{vib}^{alloy}, we use the following definition of $\Delta g(E)$:

$$\Delta g(E) = g(E) - g_I(E) \tag{2.4}$$

where $g_I(E)$ is the DOS of the majority constituent element — the element with the largest f_i. To compare the success of the many different correlations and models, we use the parameter, R, the standard error of estimate, as a measure of the quality of the fit to a straight line through the origin. We define R as

$$R \equiv \sqrt{\frac{\sum_{i=1}^{n} \left(\Delta S_i^{exp} - \Delta S_i^{fit}\right)^2}{n-2}} \tag{2.5}$$

where the index i sums over all the data points, ΔS_i^{exp} is the measured value of the vibrational entropy difference for data point i, ΔS_i^{fit} is the best fit or model value of the vibrational entropy for data point i, and n is the number of data points. The value R can be used to compare the quality of correlation between different models.

To calculate vibrational entropies, we used the phonon DOS curves for 32 com-

pounds and alloys and their 21 elemental constituents compiled in the Landolt-Börnstein tables [51, 52] and other references [48, 49, 50, 53, 56, 58, 54, 59, 36]. All neutron scattering measurements were performed at room temperature, with the exceptions of elemental Ge (80 K), Pb (80 K) and Pt (90 K). Most phonon DOS curves were obtained from coherent inelastic neutron scattering measurements of phonon dispersion curves from single crystals. The original authors fit their measured phonon dispersion curves to predictions from a Born-von Kármán model of lattice dynamics. This model was then used to calculate the phonon DOS. Exceptions were the DOS curves for the A15 intermetallics, bcc alloys and the $MgZn_2$ Laves compound, which were obtained by neutron scattering from polycrystalline samples. For these polycrystalline samples, the neutron data were interpreted in the incoherent approximation [60, 61], but without correcting for the different constituent scattering lengths. This correction is in principle impossible without prior knowledge of the lattice dynamics, but it could be important. Results for the A15 intermetallics, bcc alloys and the $MgZn_2$ Laves compound should therefore be treated with caution.

For the present study, we used two methods for obtaining phonon DOS curves. In the first method, the interatomic force constants provided by the original authors were used to calculate the phonon DOS, as described previously [57, 36]. In the second method, we converted the published graphs of the phonon DOS curves into digital form using the software package Datathief 2.0b. Although the number of original points in the data was not preserved, the shape of the DOS curve was reproduced faithfully after digitization. The digitization process provided essentially the same phonon DOS curves that we calculated from the force constants, and nearly the same values of ΔS_{vib}^{form} that we calculated directly with the Born-von Kármán model for $L1_2$ Cu_3Au, Fe_3Ni, Ni_3Al, Ni_3Fe, Pt_3Fe, and their elemental constituents. The discrepancies were used to provide the error bars for our estimates of ΔS_{vib}^{form}. All digitized DOS curves were normalized to unity, which typically required corrections of less than one part per thousand. Results for ΔS_{vib}^{form} and ΔS_{vib}^{alloy} for 32 intermetallic compounds and alloys are presented in Table 2.2. We expect that ΔS_{vib}^{alloy} is physically meaningful only when the minority constituent does not change the structure of the

underlying lattice. We therefore do not present ΔS_{vib}^{alloy} for the A15 and Laves phase compounds.

2.3 Correlations

2.3.1 Vibrational Entropy of Formation

We correlated the values of ΔS_{vib}^{form} in Table 2.2 to the standard thermochemical properties of the elements suggested by Hume-Rothery and others, i.e., differences in metallic radius, mass, electronegativity, the enthalpy of mixing [62, 63, 64, 65] and Mendeleev number [66]. Some of the more interesting correlations are reported here.

It might be expected that differences in vibrational entropy would correlate to changes in Debye temperature, Θ_D , which we obtained from measured values of the bulk modulus [67, 68, 69, 70, 71]. We used the following relationship to find the Debye temperature, Θ_D :

$$\Theta_D \propto \sqrt{\frac{B}{M}}\,\rho^{1/3} \tag{2.6}$$

where B is the bulk modulus, M is the atomic mass and ρ is the density. The value of M for the compound was the compositionally-weighted mean of the elemental atomic masses. From equation 2.6 we calculated the vibrational entropy of formation as

$$\Delta S_{vib}^{form} = -3\,k_B \ln\left(\frac{\Theta_D^{alloy}}{\prod_{i=1}^{n}\left(\Theta_D^{i}\right)^{f_i}}\right) \tag{2.7}$$

where Θ_D^i is the Debye temperature of the i^{th} constituent element. Note that any constant of proportionality in equation 2.6 would cancel in equation 2.7. The results, presented in figure 2.1, show that the Debye approximation is unsuccessful for predicting vibrational entropies of formation.

Although the Debye temperature does provide an average of phonon energies, determinations of Debye temperatures from low temperature heat capacities or from

Alloy	Structure	ΔS_{vib}^{alloy} (k_B/atom)	ΔS_{vib}^{form} (k_B/atom)
$CeSn_3$	$L1_2$	NA	-0.54 ± 0.09
$LaSn_3$	$L1_2$	NA	-043 ± 0.09
Ni_3Al	$L1_2$	-0.20	-0.20
Ni_3Fe	$L1_2$	0.02	0.09
$Ni_{0.7}Pt_{0.3}$	$L1_2$	0.24	-0.24
Pt_3Fe	$L1_2$	-0.23	0.14
Pd_3Fe	$L1_2$	-0.27	0.05
Pt_3Mn	$L1_2$	-0.25	NA
Cu_3Zn	$L1_2$	0.23	-0.01
Cu_3Au	$L1_2$	0.51	0.07
Fe_3Pt	$L1_2$	1.0	0.55
Fe_3Al	$D0_3$	-0.01	-0.06
Nb_3Al	A15	NA	-0.28
Nb_3Sn	A15	NA	-0.59
V_3Si	A15	NA	-0.31
V_3Ge	A15	NA	-0.25
$Ni_{0.3}Fe_{0.7}$	A1 (fcc)	0.13	0.32
$Ni_{0.55}Pd_{0.45}$	A1	0.48	0.02
$Nb_{0.75}Zr_{0.25}$	A2 (bcc)	0.32	0.23
$Nb_{0.2}Zr_{0.8}$	A2	0.54	0.21
$V_{0.75}Ti_{0.25}$	A2	0.37	0.31 ± 0.07
$V_{0.75}Cr_{0.25}$	A2	-0.19	-0.03 ± 0.07
$V_{0.93}Pt_{0.07}$	A2	-0.39	-0.56 ± 0.09
$V_{0.95}Pt_{0.05}$	A2	-0.26	-0.42 ± 0.09
$V_{0.95}Cr_{0.05}$	A2	-0.02	-0.10 ± 0.09
$Zn_{0.47}Cu_{0.53}$	B2	NA	0.04
$CeAl_2$	C15	NA	-0.64
$LaAl_2$	C15	NA	-0.41
YAl_2	C15	NA	-0.33
$MgZn_2$	C14	NA	0.19
Mg_2Pb	C1	NA	-0.57

Table 2.1: Vibrational entropies of alloying and formation. Entropies are in high temperature limit. NA means 'not applicable' or 'not available' , as appropriate. Unless otherwise stated, the uncertainties of ΔS_{vib}^{alloy} and ΔS_{vib}^{form} are ± 0.03 k_B/atom. The phonon DOS for elemental Sn, Ce and La were taken from the β, γ-fcc and hcp structures, respectively.

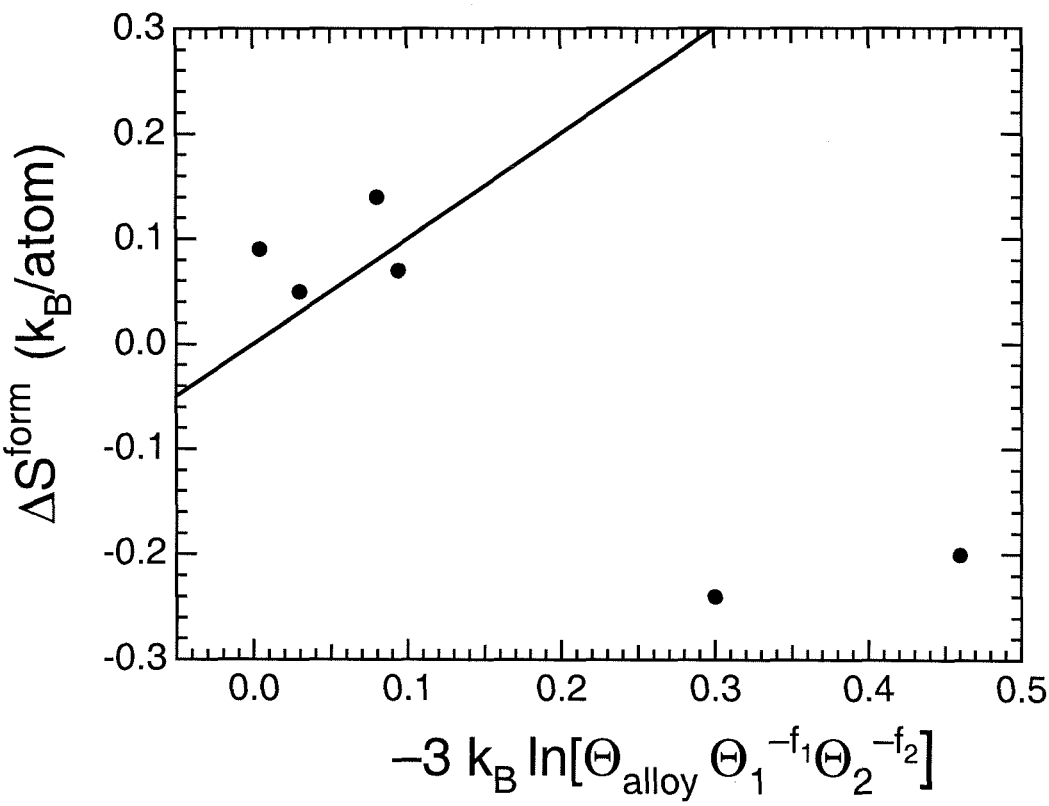

Figure 2.1: Comparison of the measured vibrational entropy of formation with that calculated from the bulk modulus in the Debye approximation (equation 2.6) for selected $L1_2$ alloys. R = 0.430.

elastic constants emphasize the low energy phonons. At modest temperatures the higher energy phonons account for most of the heat capacity, however, and the elements and compounds discussed here showed large differences in the structure of the higher energy part of their phonon DOS. The structure of the phonon DOS at higher energies is expected to depend more sensitively on the local structure of the alloy [72] than the low energy part of the DOS.

Of the correlations performed with other thermochemical parameters, the most successful involved the difference in metallic radius [73] between the majority and minority species. This correlation is shown in figure 2.2 for $L1_2$ compounds.

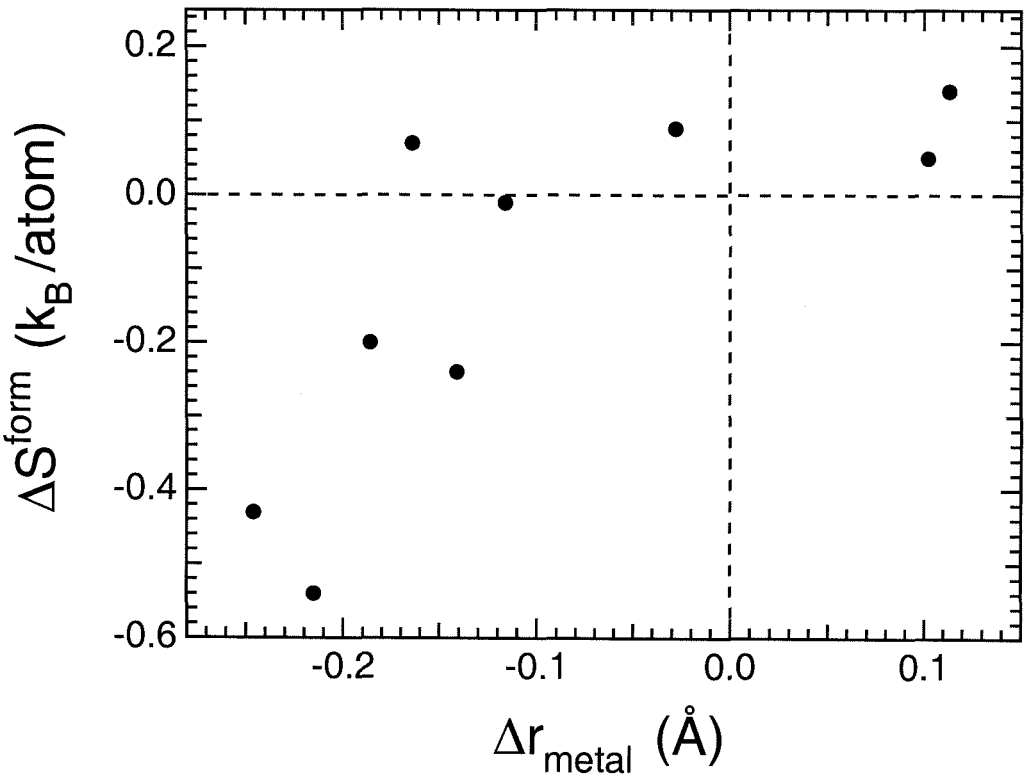

Figure 2.2: Vibrational entropies of formation of $L1_2$ alloys as a function of difference in metallic radius between the majority species and the minority species. The difference, Δr_{metal}, is positive when the majority species is larger than the minority species.

When the minority species has a significantly larger metallic radius than the majority species, the lattice becomes stiffer, so ΔS_{vib}^{form} becomes strongly negative. The same type of graph as figure 2.2 was prepared for the four A15 compounds in Table 2.2, and

a similar trend was found, although the entropy values for the A15 compounds were all strongly offset negative by about 0.36 k_B/atom. This offset may originate with the difference between bcc and A15 structures, probably because the A15 structure includes compressed chains of atoms. The $L1_2$ data of figure 2.2 lack this offset because the underlying lattice has not changed (fcc to ordered fcc).

The success of the correlation of ΔS_{vib}^{form} with differences in metallic radius seems consistent with interatomic force constants determined from coherent inelastic neutron scattering. Consider first the case where the B-atom is larger than the A-atom. The condition for axially-symmetric 1nn force constants, $C_{1xx} - C_{1xy} = C_{1zz}$, is satisfied reasonably well for both A-A pairs and A-B pairs in most $L1_2$ alloys of A_3B stoichiometry [51]. Furthermore, the force constants C_{1zz}^{A-B} are usually small, indicating that the dominant forces between A-B 1nn pairs are radial. This suggests an intuitive picture of the lattice dynamics involving spheres that interact by stiff first-neighbor central forces. First consider the case of an A_3B alloy with the $L1_2$ structure, where the larger B atoms fit tightly into a matrix of smaller A atoms. The general trend of finding large force constants C_{1xx}^{A-B} and C_{1xy}^{A-B} is consistent with this stiff sphere picture. When the larger B-atoms are squeezed onto the A-lattice without causing much change in lattice parameter, the amplitudes of the atomic vibrations are expected to be constrained, and the vibrational frequencies increased. This effect is consistent with the large slope of the curve of ΔS_{vib}^{form} versus Δr at increasingly negative Δr. (The exception to the trend in figure 2.2 was the invar alloy Fe_3Pt, not shown on figure 2.2, which has a positive ΔS_{vib}^{form} of +0.5 k_B/atom. The force constants for Fe-Pt neighbors showed by far the largest deviations from central force character of any $L1_2$ alloy. Invar alloys are generally expected to show anomalous vibrational modes.)

On the other hand, figure 2.2 shows that ΔS_{vib}^{form} is small and slightly positive when the minority atom is smaller than (or only slightly larger than) the majority atom. When the minority B-atom is smaller than the majority A-atom, we expect poor contact between the B-atom and its neighbors, and weak A-B force constants. For stiff spheres, once contact is lost, the A-B force constant is not sensitive to the

metallic radius of the B-atom. This is consistent with the flattening of the curve in figure 2.2 for small and positive values of Δr. As a corollary, we suggest that when the B-atoms are smaller than the A-atoms, the phonon DOS of the $L1_2$ alloy should be less sensitive to the state of chemical order in the alloy.

2.3.2 Vibrational Entropy of Alloying

It is well-known that mass disorder has no effect on vibrational entropy, assuming the force constants remain unchanged. It is therefore unreasonable to make a model for the effect of atomic mass on the vibrational entropies of formation of intermetallic compounds from their constituent elements. In alloying, however, substituting atoms of one mass for atoms of a different mass will alter the vibrational entropy even when the interatomic force constants remain unchanged. At a fixed temperature such a substitution will have no effect on the mean-squared interatomic displacement (in the harmonic approximation), which is set by the force constants. The substituted alloy will explore a different range in its momentum coordinates, p, however. Since $p^2/2M \propto k_B T$, the range in momentum coordinates will increase as the square root of the increased mass of the alloy. The change in vibrational entropy will be (per substituted atom):

$$\Delta S_{vib}^{mass} = 3/2\, k_B \ln\left(\frac{M_{solute}}{M_{matrix}}\right) \tag{2.8}$$

where the masses of the solute and matrix atoms are M_{solute} and M_{matrix}. The correlation between the vibrational entropy of alloying and $\ln(M_{solute}/M_{matrix})$ is shown in figure 2.3. This mass correlation, without adjustable parameters, seems reasonably successful with $R = 0.212$.

In alloying there will also be changes in interatomic force constants. A proper estimation of this contribution requires knowledge of the interatomic potential, but we attempt a simple correlation here. For $L1_2$ compounds the lattice parameters are known. We obtain the change in phonon frequencies through the Grüneisen relation:

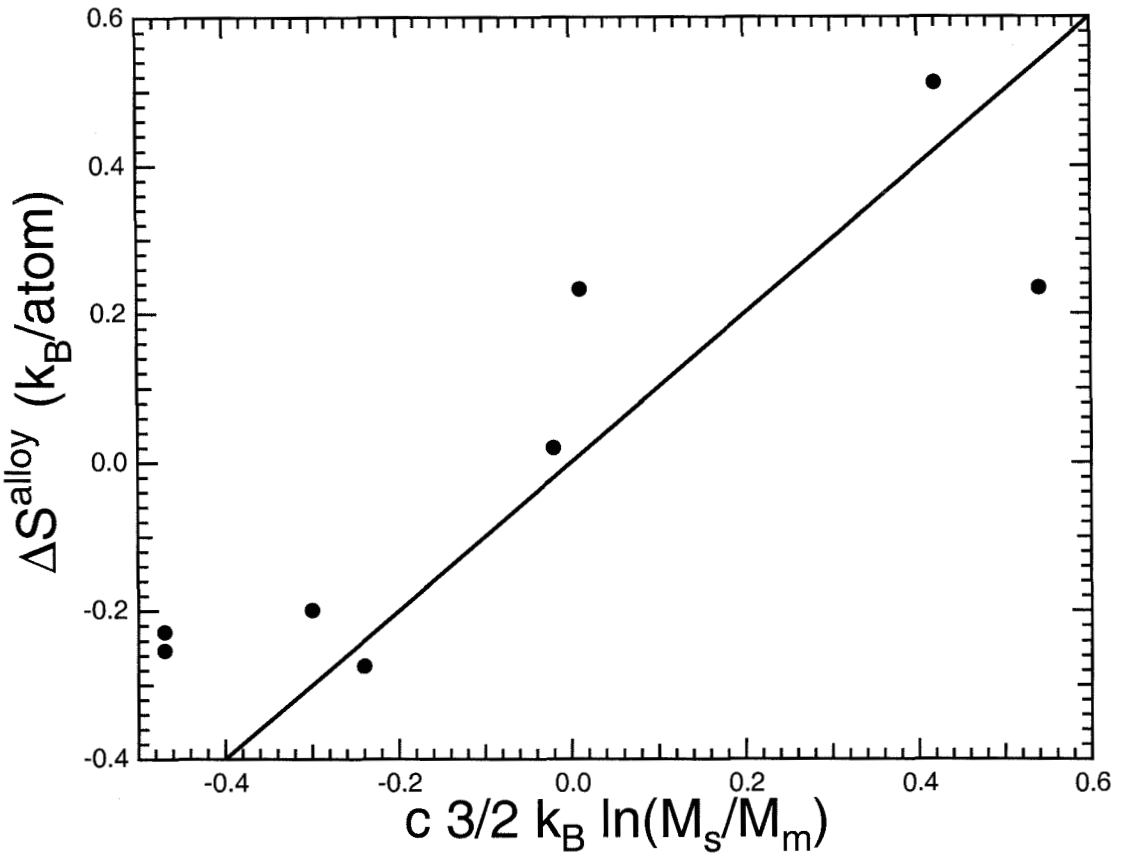

Figure 2.3: Vibrational entropy of alloying of $L1_2$ alloys compared to predictions of mass correlation in equation 2.8. The bottom axis scales linearly with c, the concentration of the minority constituent.

$$\gamma_i = -\frac{\partial \ln \omega_i}{\partial \ln V} \tag{2.9}$$

where γ_i is the mode Grüneisen parameter. Using ω_{norm} as a constant of normalization, the force constant effect on the vibrational entropy, ΔS_{vib}^{force} , can then be evaluated as

$$\Delta S_{vib}^{force} = -k_B \sum_{i=1}^{3N} \ln\left(\frac{\omega_i}{\omega_{norm}}\right) \tag{2.10}$$

$$\frac{\partial \Delta S_{vib}^{force}}{\partial \ln V} = -k_B \sum_{i=1}^{3N} \frac{\partial \ln \omega_i}{\partial \ln V} - \frac{\partial \ln \omega_{norm}}{\partial \ln V} \tag{2.11}$$

$$\Delta S_{vib}^{force} = +k_B \sum_{i=1}^{3N} \gamma_i \Delta \ln V \tag{2.12}$$

We assume the Grüneisen parameter is the same for all phonon modes. For the contribution to the vibrational entropy change upon substituting the minority species for the majority species, we attempt to use x-ray lattice parameter data [69, 74] for the change in volume upon alloying. The change in entropy of the alloy owing to changes in force constant is (per atom):

$$\Delta S_{vib}^{force} = 3\, k_B\, \gamma\, [\ln(V_{alloy}) - \ln(V_{matrix})] \tag{2.13}$$

$$\Delta S_{vib}^{force} = 3\, \gamma\, k_B \ln\left(\frac{V_{alloy}}{V_{matrix}}\right) \tag{2.14}$$

where V_{alloy} is the volume per atom of the alloy, and V_{matrix} is the volume per atom of the elemental metal of the majority species.

Combining the mass effect of alloying, equation 2.8, with the force constant effects predicted by equation 2.14, and setting $\gamma = 2$, we obtain for an alloy with solute concentration, c:

$$\Delta S_{vib}^{alloy} = c\,\frac{3}{2} k_B \ln\left(\frac{M_{solute}}{M_{matrix}}\right) + 6\, k_B \ln\left(\frac{V_{alloy}}{V_{matrix}}\right) \tag{2.15}$$

For $L1_2$ alloys, the correlation with equation 2.15 is less successful than the mass effect alone (equation 2.8 and figure 2.3). The theoretical fit overestimated the measured entropy change by a factor of 2 to 3 in most cases. The change in unit cell volume may be unsuccessful as a parameterization of the change in vibrational modes because some interatomic separations are reduced, and some are expanded beyond their equilibrium separations when an atom of different size is inserted into the matrix. Upon alloying, some of the interatomic forces are therefore increased, and some decreased. The expected trend for correlation of vibrational modes to the unit cell volume is uncertain. We may expect equation 2.15 to be more appropriate for the vibrational entropy of substitution between the same crystal structures. Figure 2.4 shows the vibrational entropy difference between similar Laves, $L1_2$ and A15 phases as a function of minority constituent and volume difference [69, 74]. The same data plotted versus equation 2.8 (mass term only) gives a moderately better correlation (not shown) with an R value of 0.316.

In figure 2.5 we plot the vibrational entropy of alloying for $L1_2$ alloys against the Debye model approximation of equations 2.6 and 2.7. As was the case for the vibrational entropy of compound formation, the Debye temperature is not very successful for predicting the vibrational entropy of alloying. The emphasis of the Debye temperature on low energy phonons makes it less relevant for most of the phonon DOS.

Finally, in figure 2.6 we plot the vibrational entropy of alloying for eight $L1_2$ compounds versus the atomic volume change associated with alloying. The correlation is good, with an R value of 0.190. Atomic mass and atomic volume are correlated, however, and an examination of the data in figure 2.6 shows that to a large extent the correlation shown is similar to that of figure 2.3. Although the R values of the mass and volume correlations are comparable, the mass correlation is more impressive, since it involved no adjustable parameters. For the volume correlation in figure 2.6, the slope of the line was a free parameter. Using the slope of the best fit line and a value of 13 $Å^3$/atom for V_{matrix}, the Grüneisen constant for figure 3.6 was determined to be 1.2. The average Grüneisen constant calculated from the bulk modulus, thermal

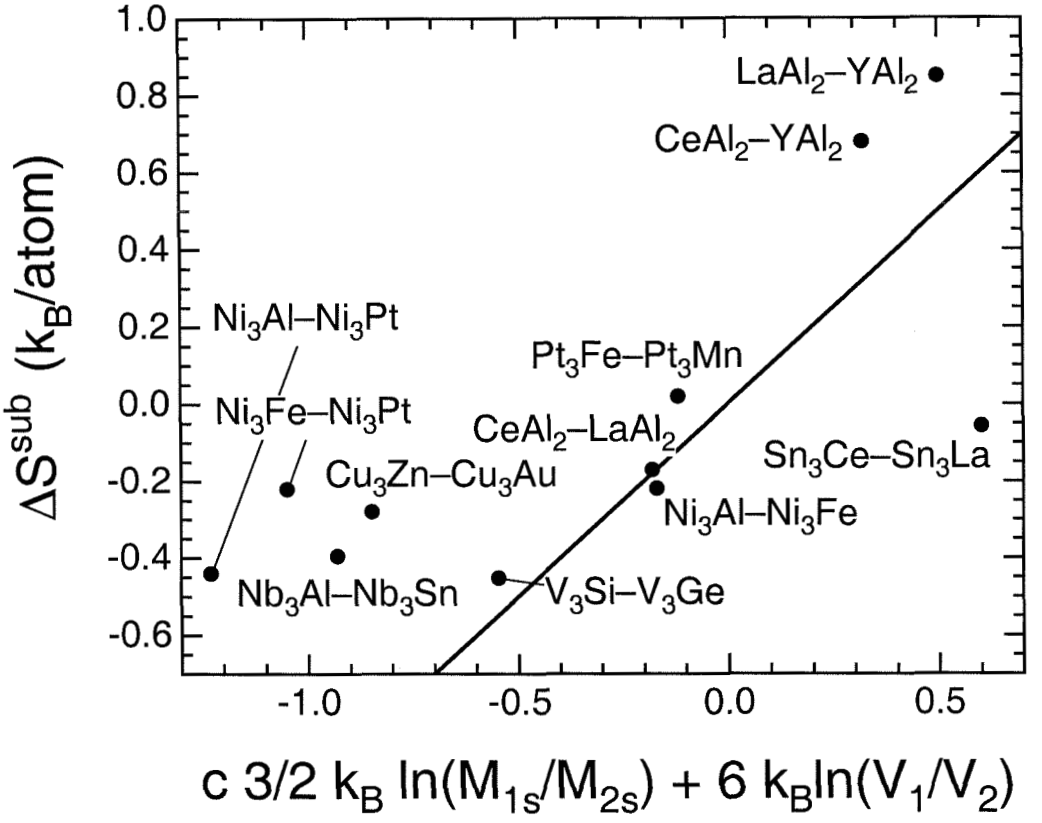

Figure 2.4: The vibrational entropy difference of substitution for Laves, A15 and $L1_2$ alloys versus the prediction from equation 2.15. The specific intermetallics being compared are indicated for each data point. The variables M_{1s} and M_{2s} are the atomic masses of the minority constituents of the final and initial states, respectively. R = 0.541.

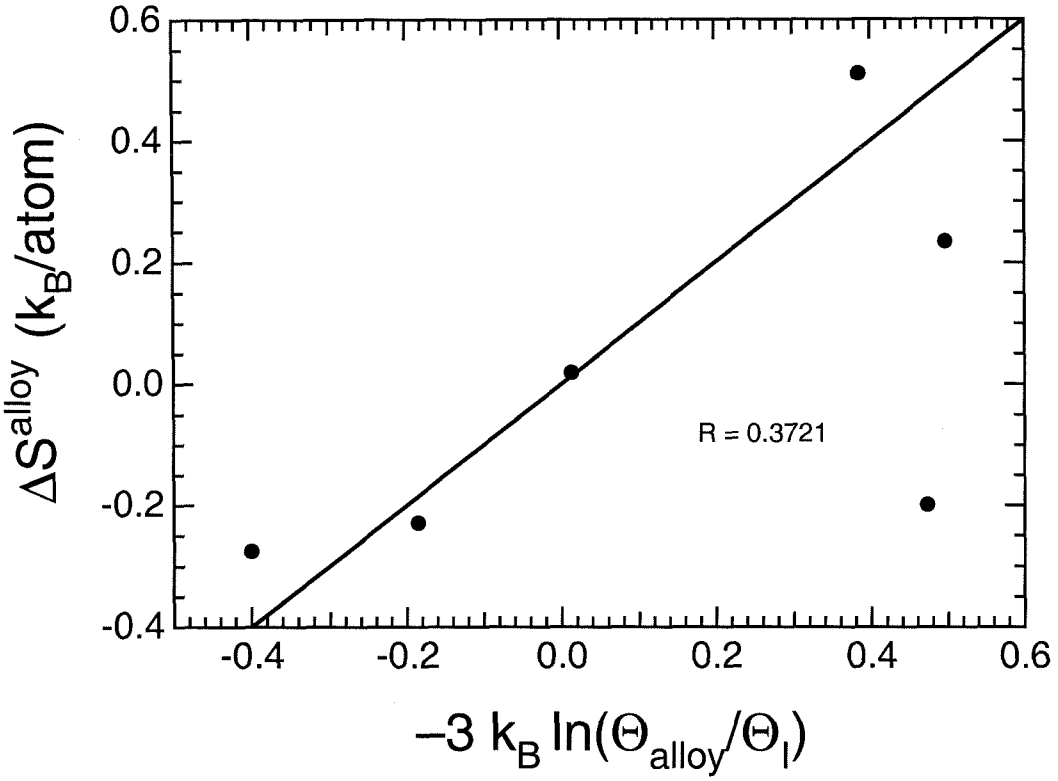

Figure 2.5: The vibrational entropy of alloying for six $L1_2$ alloys compared to the entropy predicted from the bulk modulus in the Debye approximation. Θ_I is the Debye temperature of the majority constituent element. R = 0.372.

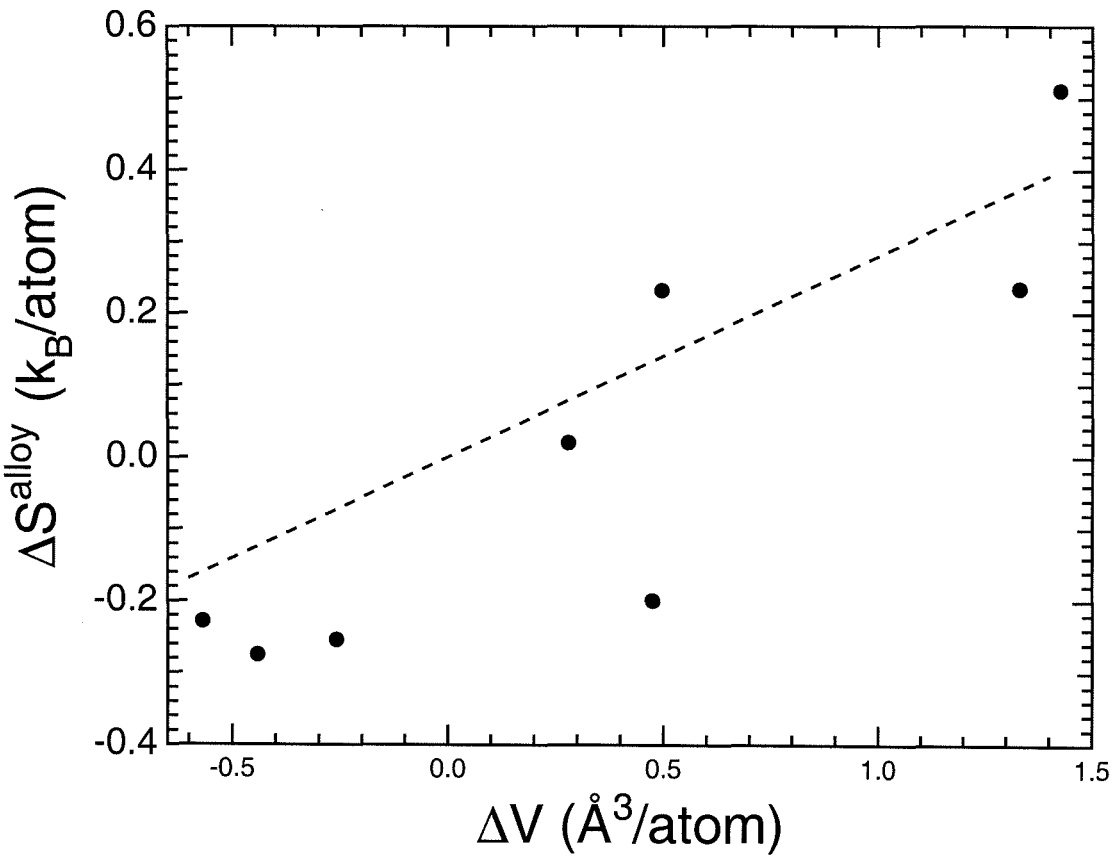

Figure 2.6: The vibrational entropy of alloying for eight $L1_2$ alloys as a function of the difference ΔV in atomic volume (from x-ray lattice parameter) before and after alloying, where $\Delta V \equiv V_{alloy} - V_{majority\ species}$. Dashed line is the best fit through the origin.

Correlation	Model	R
Debye (equation 2.7)	$-3\,k_B \ln\left(\frac{\Theta_D^{alloy}}{\Theta_D^{majority}}\right)$	0.372
Mass (equation 2.8)	$c\,3/2 \ln\left(\frac{M_s}{M_m}\right)$	0.208
Mass plus Grüneisen (equation 2.15)	$c\,3/2 \ln\left(\frac{M_s}{M_m}\right) + 6 \ln\left(\frac{V_{alloy}}{V_{matrix}}\right)$	0.637
Change in atomic volume (Å^3/atom)	linear regression through origin	0.207
Difference in metallic radius (Å)	linear regression through origin	0.280

Notes: For consistency, R values for all correlations were calculated with six $L1_2$ compounds for which all physical parameters were available.

Table 2.2: Correlations with entropy of alloying.

expansion [75] and classical heat capacity for five $L1_2$ compounds was 1.82 ± 0.46. The average Grüneisen constant (derived from best fit line to ΔV, see figure 2.6) for the same 5 $L1_2$ compounds was 1.04. The lack of agreement is a good indication that equation 2.13 fails to model the observed entropy of alloying, and that the correlation in figure 2.6 may, as stated above, reflect the correlation between atomic volume and atomic mass.

Some comparison of the success of the various correlations for the entropy of alloying are presented in Table 2.2. Six $L1_2$ compounds were chosen for the results of Table 2.2 because bulk moduli were available for them. For consistency, these same six compounds were used for all correlations in Table 2.2.

It is important to note some limitations of the experimental measurements of the phonon DOS curves. The phonon DOS curves for the A15 compounds (Fawcett, et al. 1983) were determined in the incoherent scattering approximation, but no attempt was made to correct the experimental DOS curve for differences in neutron scattering cross-sections and masses of the elements. The relative strength of scattering of each element is determined by the quotient of total scattering cross-section and atomic mass. Those phonons that involve primarily the motions of atoms having a small value of this ratio will be under-represented in the experimental phonon DOS. For example, the ratios of total scattering cross-section to mass differ by 60% for Nb and Sn in Nb_3Sn, but differ by only about 20 - 25% for the other A15 compounds. The entropy of formation of Nb_3Sn may therefore be in error. The phonon DOS

curves for the bcc alloys listed in Table 2.2 were also obtained in the incoherent scattering approximation (Fawcett et al. 1983), suggesting problems with the V-Ni alloy. Finally, we point out that the phonon DOS curves used for the data of Table 2.2 were obtained at temperatures of 300 K and below. For phase transformations at elevated temperatures, anharmonic effects could alter considerably the vibrational entropies.

2.4 Summary

Using all available data on phonon densities of states of intermetallic compounds, alloys, and their elemental metals, we calculated and tabulated the vibrational entropies of formation of the alloys and compounds in the harmonic approximation. The range of these entropies of formation, from -0.64 to $+0.55$ k_B/atom, is larger than the maximum possible range for the configurational entropy of formation of a binary alloy. Vibrational entropies of alloying ranged from -0.35 to 1.0 k_B/atom.

We correlated the vibrational entropies of formation to several thermophysical properties of the atoms. The Debye approximation does not account adequately for the structure of the phonon DOS, and the Debye model made poor predictions of the vibrational entropy of formation and the vibrational entropy of alloying. For $L1_2$ compounds and A15 compounds, we found that the vibrational entropy of formation correlated best to the difference in metallic radius of the two atomic species. We also modeled the vibrational entropy of alloying in terms of atomic mass and volume effects. The correlation between the vibrational entropy of alloying and the mass ratio of the solute and matrix atoms was most successful, although correlations involving the volume and metallic radius were also good.

Chapter 3 The Role of Phonons in the Thermodynamics of the NiTi Martensitic Transformation

3.1 Introduction

The intermetallic compound NiTi exhibits the shape memory effect near room temperature. This phenomenon involves large, reversible strains, and is closely related to the martensitic transformation that occurs spontaneously upon heating or cooling. The high temperature 'austenite' has the cubic B2 structure (CsCl prototype), and the low temperature 'martensite' has a monoclinic B19′ structure [76]. Since this martensitic phase transformation is reversible, we expect the austenite to have larger energy and larger entropy than the martensite. The present investigation addresses the entropy. Since the atom motions during the transformation occur by a cooperative process, no significant change in configurational entropy can occur. The phase transformation involves no known chemical, electronic or magnetic ordering; hence the entropy should be entirely vibrational.

Calorimetric methods were used in several previous investigations of the martensitic transformation in NiTi. McCormick and Liu [77], using the temperature dependence of the transformation stress, measured an entropy gain of 0.41 k_B/atom upon transforming to austenite. Johari and coworkers [78] measured values of 0.44 ± 0.09 k_B/atom and 0.37 k_B/atom using pressure-dependent resistivity and calorimetry, respectively. Smaller values were reported by Obradó, Mañosa and Planes for Cu-Al-Mn alloys [79]. Calorimetry can provide useful numbers, but it does not address the atomistic origin of the transformation entropy. There have been several previous investigations using coherent inelastic neutron scattering to measure phonon soften-

ing in the austenite near the martensitic transformation temperature. These studies on NiTi [80, 81, 82, 83], with a single exception [84], were single-crystal experiments measuring a few phonon dispersion curves. Their focus was on the mechanism by which the phase transformation occurs, not the vibrational entropy. More recently, there have been several experimental and theoretical investigations on the role of vibrational entropy in solid-state phase transformations [34, 35, 38, 10]. The emphasis of this work has been on how differences in vibrational entropy originate from differences in the phonon density of states (DOS) of the different phases. The present investigation has this same emphasis.

We performed measurements of the phonon DOS, heat capacity, transformation enthalpy, thermal expansion, and performed calculations of Born-von Kármán lattice dynamics to investigate the vibrational entropy of the martensitic transformation. The neutron scattering and latent heat data gave independent measurements of the entropy. The heat capacity measurements and lattice dynamics simulations were used to check the reliability of the phonon DOS measured by neutron scattering. The phonons implicated in the mechanism of the martensitic transformation, the $\mathbf{k} = \frac{1}{3}[110]\,2\pi/a$ transverse acoustic phonons, are not sufficient in number to account for the entropy of the transformation. On the other hand, the softness of the acoustic branches in the B2 austenite phase is shown to be responsible for most of the vibrational entropy of the phase transformation. The stability of this bcc-like B2 phase seems related to the transverse force constant between first-nearest neighbors.

3.2 Experimental Methods

A NiTi plate of 0.125 cm thickness was obtained from Shape Memory Applications, Inc., and annealed for 15 min at 700 °C. This annealed plate provided all samples for the present study. The sample for differential scanning calorimetry was ground into a 0.2613 g disc of approximately 0.20 cm diameter. Nickel metal of 99.99% purity was selected as a reference material, and the Ni sample was cold-rolled and ground to a 0.3293 g disc. The masses were chosen so the two samples had approximately

the same number of atoms.

Low-temperature heat capacity measurements were performed with a Perkin-Elmer DSC-4 differential scanning calorimeter that had been modified by installing its sample head in a liquid helium dewar. The latent heat measurements were taken using liquid nitrogen as the cryogen. Heating scans were performed from −90 °C to +100 °C, at heating rates of 10, 5 and 3 °C per second. Cooling scans were taken from +100 °C to −90 °C at cooling rates of 10 and 5 °C per second. All measurements were repeated with the two samples interchanged in the sample pans. Representative data are shown in figure 3.1.

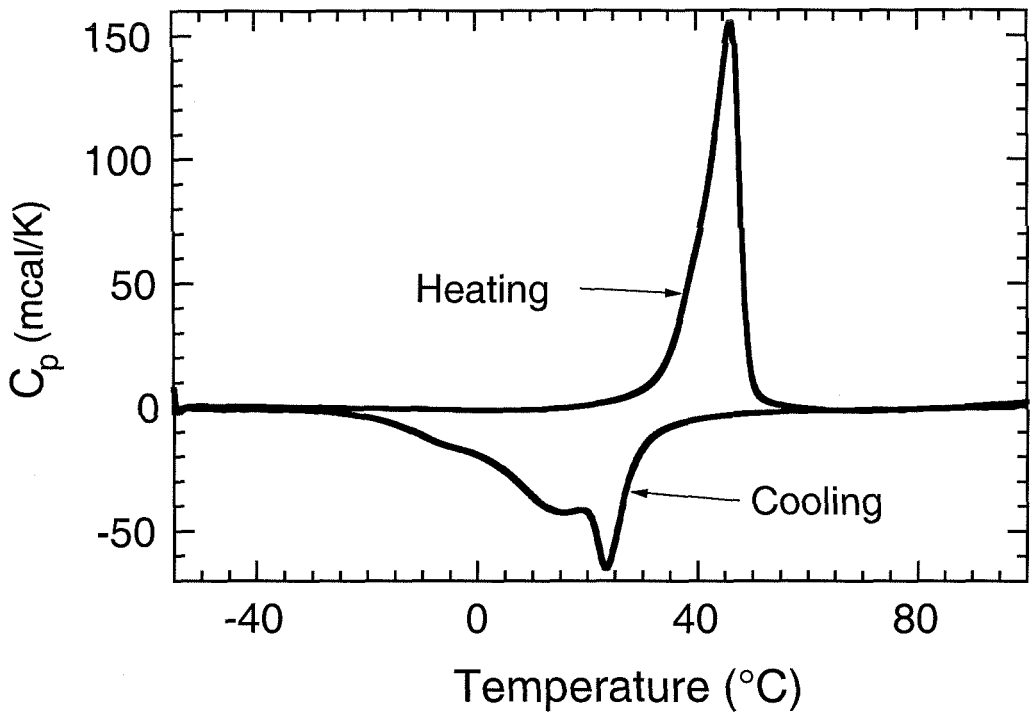

Figure 3.1: Representative data of the latent heat upon cooling and heating of the martensite–austenite phase transformation in NiTi. In both cases a background has been subtracted from the raw data.

Using the same samples and calorimeter, the differential low temperature heat capacity of martensitic NiTi was measured with respect to Ni. Liquid nitrogen was used as the cryogen, allowing measurements of the differential heat capacity from −170 to −50 °C. Data were taken with a heating rate of 20 °C/min in 30 °C intervals with 10 °C overlaps. Scans were repeated with samples interchanged in the sample

pans. The difference between the pairs of data with samples interchanged is equal to twice the differential heat flow, from which the differential heat capacity was found. The differential heat capacity was added to the heat capacity of Ni [85] to obtain the absolute heat capacity for martensitic NiTi. The result is shown in figure 3.2.

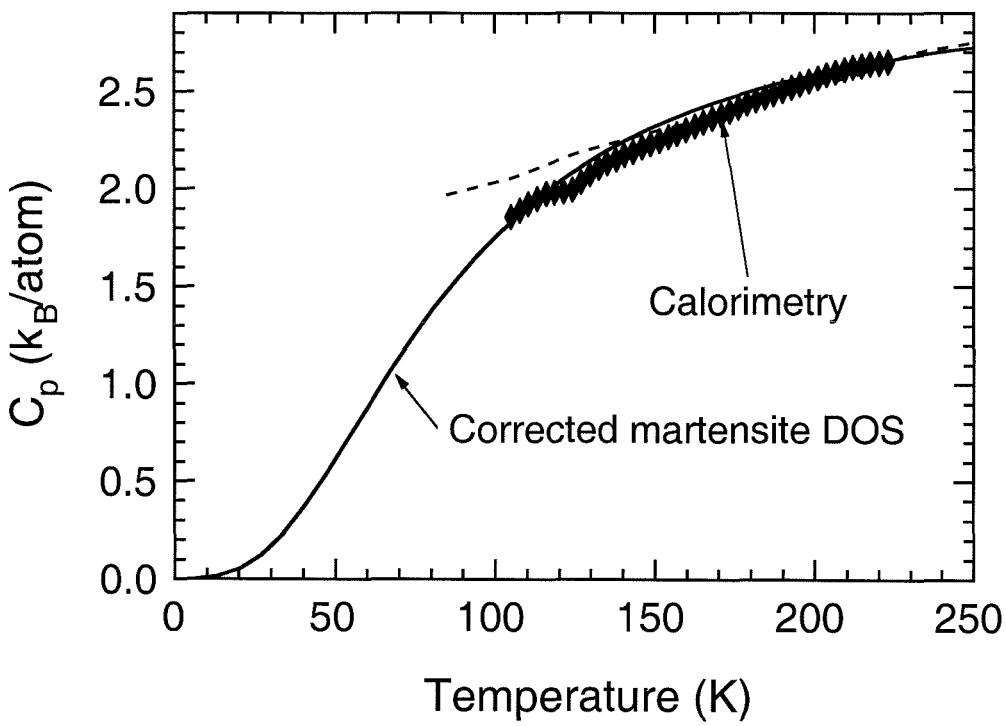

Figure 3.2: The low-temperature heat capacity of martensitic NiTi. The filled diamonds are our calorimetric results. The thin curve was calculated from the neutron-weight corrected martensite phonon DOS derived from low temperature neutron inelastic scattering (shown in figure 3.6). Dashed line is heat capacity taken from Herget, et al. [84].

Three samples for thermal expansion measurements were cut with a water-cooled diamond saw into rectangular prisms of typically 0.5 × 0.7 × 0.125 cm. A Perkin-Elmer TMA 7 with liquid nitrogen as the cryogen was used for measuring the linear thermal expansion from −160 to +100 °C. Samples were cycled typically between −160 and +100 °C at heating (cooling) rates of 20, 10 and 5 °C/min. Our best data were obtained at 5 °C/min, and these are shown in figure 3.3.

Inelastic neutron scattering spectra were measured with a time-of-flight (TOF) chopper spectrometer (LRMECS) at the Intense Pulsed Neutron Source (IPNS) at the Argonne National Laboratory. The sample for inelastic neutron scattering was a

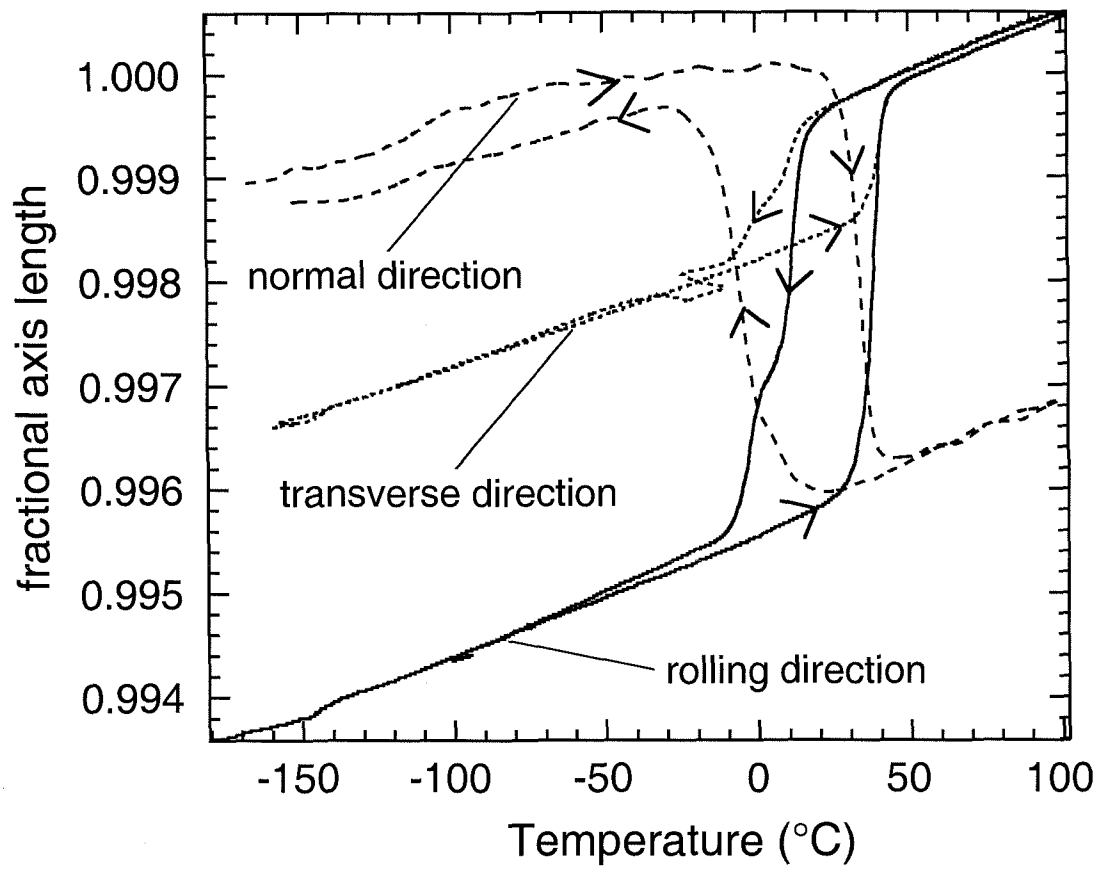

Figure 3.3: Thermal expansion of NiTi plate in three orthogonal directions. The long dashed line is linear expansion in the direction perpendicular to the plane of the plate. The continuous and short dashed lines are linear expansion in orthogonal directions within the plate plane. Data were taken with the sample at low temperature, proceeding to 100 °C and then returning to low temperature. Heating and cooling are indicated by arrows.

plate of 7 × 9 × 0.125 cm encased in thin-walled Al pans and mounted at a 45 ° angle normal to the incident beam to minimize self shielding. Total scattering was 13%. Spectra with an incident energy of 50 meV were measured at 8, 77, 127, 177, 300 and 573 K. The 300 and 573 K data were taken with the sample in the IPNS "drylid" furnace, while the 8, 77, 127 and 177 K data were obtained with a displex refrigerator. Background spectra were measured from the empty can both in the furnace and in the refrigerator at 300 K. The broad detector coverage of LRMECS, ranging from 3 ° to 117 °, allowed measurements over a range of momentum and energy transfer $(\mathbf{k}, \hbar\omega)$, with $\mid \mathbf{k}(\omega) \mid$ varying between 0.5 and 8.3 Å^{-1} when $\hbar\omega$ varied from 0 to +50 meV.

Method	ΔS (k_B/atom)	ΔH (J/mol)
Calorimetric heating	$\geq 0.41 \pm 0.04$	1070 ± 100
Calorimetric cooling	$\leq 0.56 \pm 0.1$	-1300 ± 200
Calorimetric (section 3.3.1)	0.47 ± 0.09	NA†
Neutron scattering	0.57 ± 0.03	NA†

†not available.

Table 3.1: Enthalpy and entropy of martensite transformation. Calorimetric error bounds were obtained from the statistical variation of the repeated measurements for both heating and cooling.

3.3 Results

3.3.1 Calorimetry

The enthalpy of the martensitic transformation is obtained from the area under the heating and cooling curves in figure 3.1. The entropy can then be calculated by integrating dQ/T, where dQ is the measured heat input, over the temperature range of the phase transformation. A reversible process should provide the same values of ΔH and ΔS for heating and cooling, but Table 3.1 shows a discrepancy between the heating and cooling results slightly beyond the error bars.

This hysteresis of the phase transformation implies that the transformation to martensite is more dissipative. Assuming this is so, the values of ΔS in Table 3.1 are upper and lower bounds as indicated. Alternatively, by assuming that the heating and cooling enthalpies are in substantial agreement (within error bars), we can calculate $\Delta S = \Delta H/T_c$, where the equilibrium transformation temperature, T_c, is assumed to lie equidistant between the heating and cooling transformation start temperatures. This provides a value for ΔS of 0.47 ± 0.09 k_B/atom.

The calorimetry curves of figure 3.1 did not vary with cooling and heating rate, but they did change with cycling. This effect has been reported previously [86, 87, 77], and has been attributed to increasing defect densities and internal stresses in the martensite. Perhaps such microstructural dissipation mechanisms could be responsible for the small discrepancy between the heating and cooling results of Table 3.1.

3.3.2 Thermal Expansion

Figure 3.3 presents the fractional sample dilatation versus temperature along each orthogonal sample dimension. The anisotropy of the B19′ martensite structure and the strong crystallographic texture of the samples caused different dilatations in each direction. The martensitic transformation is evident between −30 and +50 °C, where the linear thermal expansion is interrupted by a large contraction or expansion, depending on the axis. Summing the linear transformation dilatations gives a volumetric expansion of −0.2% (i.e., a contraction) upon transformation to martensite.

The transformation start and stop temperatures for heating and cooling agree well with those observed in the calorimetric measurements of the latent heat (figure 3.1). The complicated kinetics observed upon cooling, which appear as the three separate peaks in the cooling curves in figure 3.1, are also observed in the thermal expansion data. The linear expansions measured within the plane of the rolled plate (short dashed and solid lines, figure 3.3) show a kink in slope between 0 and 10 °C upon cooling, corresponding to the region between the peaks in latent heat of cooling at −4 and +12 °C (figure 3.1).

The linear thermal expansion was determined by measuring the slopes of the curves in the straight regions above and below the transformation temperature (figure 3.3). For martensite this depends on the crystallographic direction. Summing the linear thermal expansion in all three plate dimensions gives the volumetric thermal expansion, which is independent of the crystallographic texture in the sample. The coefficients of volume thermal expansion are $36 \pm 3 \times 10^{-6}\mathrm{K}^{-1}$ for the austenite and $30 \pm 2 \times 10^{-6}\mathrm{K}^{-1}$ for the martensite.

3.3.3 Neutron Scattering

All TOF spectra were first normalized and corrected for detector efficiency and time-independent background following standard procedures. In this step, the detector counts were grouped into 10 ° ranges of scattering angles having average angles from 5 ° to 115 °. The scattering contribution of the container and displex (or furnace)

was removed using the runs on the empty container. The data below 3–4 meV are dominated by the large elastic peak, which was stripped from the data by assuming the raw data were linear in energy at small energy transfer.

The first step in obtaining a phonon DOS from the corrected spectra used an iterative procedure to calculate the multiphonon contribution to the measured scattering, and this multiphonon contribution was subtracted from the data [88]. The 'neutron-weighted' phonon DOS, $g_{NW}(E)$, is obtained easily from the remaining 1-phonon cross-section. When using this procedure with data from LRMECS, we accounted for the fact that the TOF spectra were obtained at constant scattering angle, not constant scattering vector. The scattering vector and multiphonon correction therefore vary with energy transfer, and this dependence is different for the energy spectra from the different angle banks. The sum of the corrected intensities from the upper 6 angle banks was used to obtain the phonon DOS. Disallowing the data from the lower 6 angle banks eliminates any possible contribution from magnetic scattering, which is greatly suppressed at high Q. Summing over the highest angle banks ensures that a large portion of reciprocal space is sampled at each phonon energy. Figure 3.4 shows that the calculated 1–5 phonon contribution fits well a typical TOF spectrum of austenite. The amount of the multi-phonon (2–5 phonon) contribution is large at this temperature.

These background, elastic and multi-phonon corrections are sufficient when the sample contains only one species of scatterer. When applied to an alloy, however, these procedures provide a 'neutron-weighted' phonon DOS, $g_{NW}(E)$. The weighting originates with the following phenomenon: Ni and Ti scatter neutrons with different cross-sections, so each vibrational mode scatters neutrons with an efficiency that depends on the displacement amplitudes of Ni and Ti atoms. Failing to correct for this phenomenon leads to errors in the calculated phonon DOS. A rigorous correction is possible if the partial phonon densities of states $g_d(E)$ is known for each atom, d, where

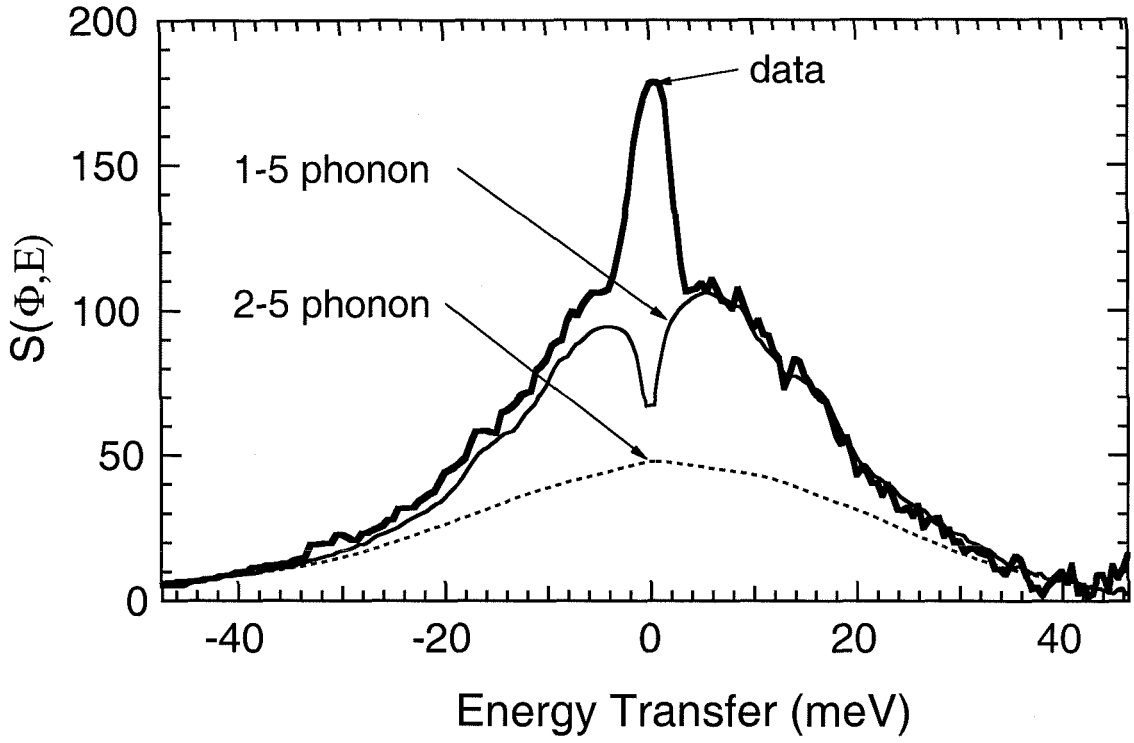

Figure 3.4: Raw TOF data compared with the self-convergent multiphonon expansion. The background corrected TOF spectra, at the 12th angle bank, of NiTi at 573 K is the bold line. The thin line is the 1–5 phonon contribution as calculated with the procedure of Bogdanoff, Fultz and Rosenkranz [88]. The dashed line is the 2–5 phonon contribution.

$$g_d(E) = \sum_{q,j} | e^d_{q,j} |^2 \, \delta(\hbar\omega_{q,j} - E) \tag{3.1}$$

and $\mathbf{q}$ and j are the phonon wave vectors and polarization branch that specify a single vibrational mode. Here $e^d_{q,j}$ and $\omega_{q,j}$ are the polarization vector for atom d and frequency of mode $\mathbf{q}$,j. Note that $g(E) = \sum_d g_d(E)$ but the neutron-weighted phonon DOS $g_{NW}(E)$ is given by

$$g_{NW}(E) \propto \sum_d g_d(E) \exp(-2W_d) \exp(2W) \frac{\sigma_d}{m_d} \tag{3.2}$$

where $\exp(-2W_d)$,σ_d and m_d are the Debye-Waller factor, total scattering cross-section and mass of atom d. The Debye-Waller factor is an explicit function of $g_d(E)$. The term exp(2W) is the average Debye-Waller correction; this is calculated from the

self-consistent neutron-weighted DOS. The factor $\exp[2(W - W_d)]$ is approximately unity. For the case where σ_d/m_d is the same for all species d, $g_{NW}(E) \approx g(E)$. For the case of NiTi, the quotient of σ_{Ni}/m_{Ni} and σ_{Ti}/m_{Ti} is 3.6, so the correction is potentially large. We need a correction function F(E), where

$$g(E) = g_{NW}(E)\, F(E) \tag{3.3}$$

The correction function F(E) for the austenite DOS was obtained by a Born-von Kármán lattice dynamics simulation. Such simulations are often used to generate interatomic force constants by fitting to experimental phonon dispersions. In turn, the force constants can be used to calculate complete lattice dynamics information for the crystal, including the partial DOS, the neutron-weighted DOS, and arbitrary phonon dispersions. The acoustic phonon dispersions in the high symmetry directions are well documented in the literature [80, 81, 82, 89], and the neutron-weighted phonon DOS is known from our measurements. These data provide adequate constraints on the force constants to allow a hybrid least-squares fit procedure. Our model generates the dispersions of acoustic phonons, which are well-documented, but also generates the neutron-weighted phonon DOS by sampling the phonon frequencies and polarization vectors over the irreducible portion of the Brillouin zone of the B2 structure. The best 16 independent force constants out to 4^{th} nearest neighbors are shown in Table 3.2. These force constants produce a good fit to the neutron-weighted phonon DOS and a fair fit to the known acoustic dispersions. [1]

Using the force constants of Table 3.2, the correction function F(E) is calculated from the lattice dynamics simulations by taking the ratio of the real and neutron-weighted DOS, both of which are generated by the simulation. As with any optimization scheme, the uniqueness of the fitted force constants is unclear. Nevertheless, the shape and magnitude of the calculated F(E) itself proved rather insensitive to the choice of force constants. This correction function is shown in figure 3.5.

[1] Previous Born-von Kármán simulations [90, 89] have focused exclusively on the acoustic phonon dispersions, and the force constants obtained give very poor results for the optical (high-energy) modes.

	Force Constants (10^3dyne/cm)		
	Ni-Ni	Ti-Ti	Ni-Ti
1XX			8.3
1XY			14.0
2XX	7.3	21.4	
2YY	-1.4	2.0	
3XX	0.0	-0.4	
3ZZ	5.2	-1.2	
3XY	0.6	-4.0	
4XX			0.0
4YY			0.0
4XZ			0.9
4YZ			-0.8

Table 3.2: Best fit Born-von Kármán force constants to NiTi neutron-weighted phonon DOS.

The correction is physically reasonable. Given the lower mass of Ti compared to Ni, we expect the higher-energy modes to have more Ti displacements and the lower-energy modes to have more Ni displacements. Since the scattering is stronger for Ni, the higher-energy modes are under-emphasized in the neutron-weighted DOS. The correction, F(E), should enhance the high energy modes at the expense of the low energy modes. We also expect the correction to become a constant in E at low energies in the hydrodynamic limit. We use the same F(E) to correct the martensite neutron-weighted DOS. Although the real correction function for martensite is most likely different in detail, we note below that the F(E) for austenite is successful in providing a martensite phonon DOS that is consistent with the heat capacity measurements on martensite. The corrected and uncorrected (neutron-weighted) martensite DOS are shown in figure 3.5. The corrected austenite and martensite DOS are shown in figure 3.6.

As a test for the reliability of applying the austenite correction function to the $g_{NW}(E)$ of the martensite, the heat capacity calculated from the corrected martensite DOS is shown by the solid curve in figure 3.2. The agreement with the experimental data is quite good. Herget, et al. [84] measured the neutron-weighted phonon DOS of $Ni_{50.5}Ti_{49.5}$ at 200, 296 and 406 K using a TOF spectrometer with an incident neutron

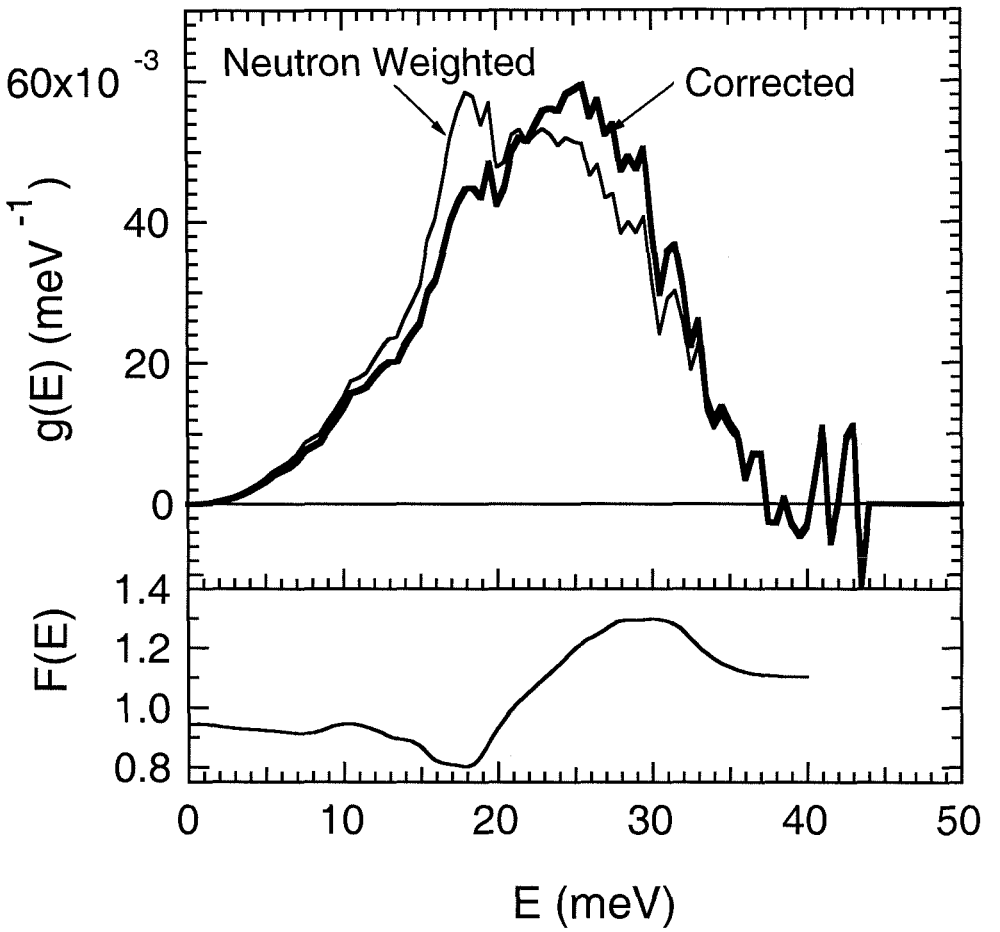

Figure 3.5: The upper curves show the uncorrected and corrected martensite DOS. The thin curve is the neutron-weighted martensite DOS, obtained by averaging the measurements at 127 and 177 K. The thick curve is the neutron-weighted DOS multiplied by the correction function F(E). The lower plot shows the correction function F(E), derived from Born-von Kármán lattice dynamics simulation.

energy of 52 meV. They compared the heat capacity taken from the literature to the heat capacity generated from their neutron-weighted martensite DOS. Although the two are in rough agreement, it is clear that their heat capacity curve, shown in figure 3.2, is in error because it exhibits a linear dependence on temperature at low temperatures where it should be decreasing much more rapidly. As noted above, a substantial correction, F(E) of equation 3.3, is required if the neutron-weighted DOS is to be consistent with the calorimetric heat capacity. Our neutron-weighted DOS agrees very well with the curves of Herget, et al. The shapes of our corrected phonon DOS curves are different, of course, as shown in figure 3.5. Unlike this earlier study,

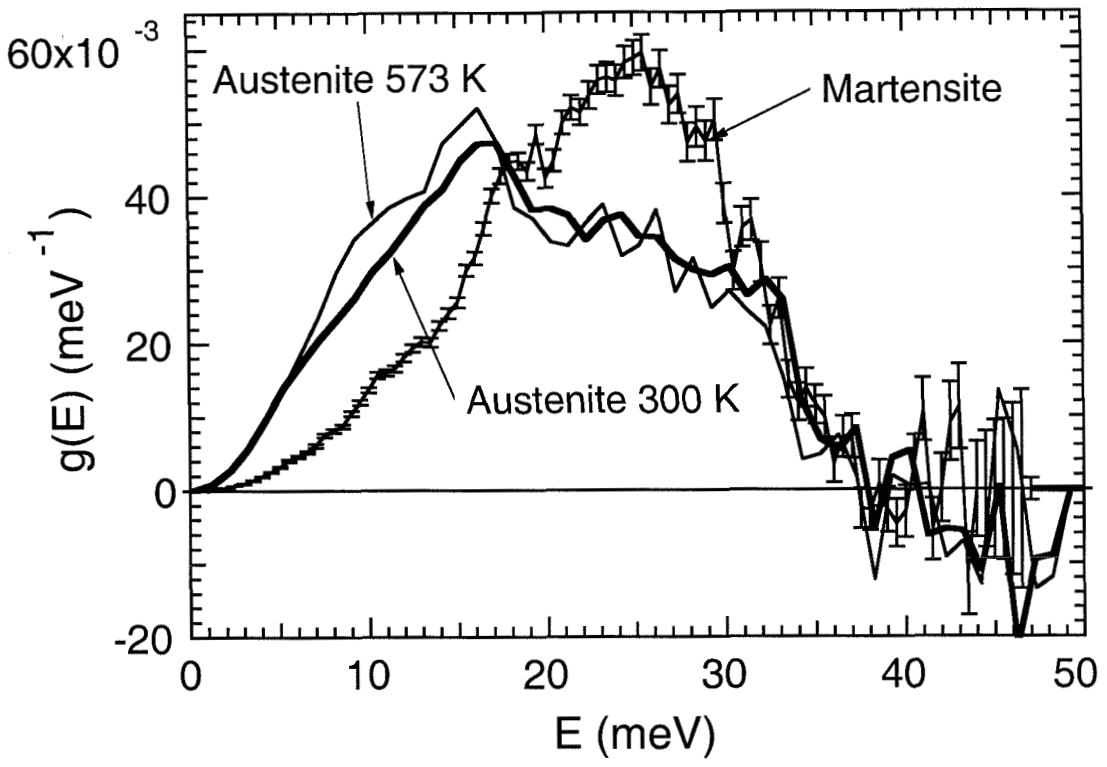

Figure 3.6: Phonon DOS of NiTi from 8 to 573 K. The thin curve with error bars is the average of the DOS curves from 127 to 177 K, the bold curve is the 300 K DOS, and the unadorned thin curve is the 573 K DOS.

which found no statistically significant softening between the 296 and 406 K data, our measurements to 573 K seem to show a softening in the DOS.

3.4 Discussion

3.4.1 Vibrational Entropy

In the quasi-harmonic approximation, the vibrational entropy of phase A, $S^A_{vib}(T)$, is calculated from the DOS of phase A at temperature T, $g^A_T(E)$:

$$S^A_{vib}(T) = -3\,k_B \int_0^\infty g^A_T(E)[(n_E+1)\ln(n_E+1) - n_E \ln(n_E)]\,dE \qquad (3.4)$$

where n_E is the Bose-Einstein distribution. The vibrational entropy of the martensite-austenite phase transformation can be calculated from the respective DOS curves as

$$\Delta S_{vib}^{m-a} = S_{vib}^{austenite}(T_c) - S_{vib}^{martensite}(T_c) \tag{3.5}$$

where T_c is the transformation temperature and $S_{vib}^{A}(T_c)$ is given by equation 3.4 using $g_{T_c}^{A}(E)$ of phase A. From the phonon DOS curves of figure 3.6, ΔS_{vib}^{m-a} 0.57 $\pm$ 0.03 k_B/atom at 300 K. This value falls within the bounds on ΔS^{m-a} as measured by calorimetry (see Table 3.1). Contributions to ΔS^{m-a} from non-vibrational sources are either small or mutually-cancelling.

By using phonon DOS curves obtained at different temperatures T, equation 3.4 can account for the anharmonic contributions to the vibrational entropy. For our two DOS curves of the austenite phase obtained at 300 and 573 K, ΔS_{vib}^{anh} can be calculated as

$$\Delta S_{vib}^{anh}(\Delta T) = S_{vib}^{573K}(573K) - S_{vib}^{300K}(573K) = 0.15 k_B/atom \tag{3.6}$$

The anharmonic contribution to the vibrational entropy of an individual phase can be calculated with the classical formula

$$S_{vib}^{anh}(T) = \int_0^T B(T)\,\nu(T)\,[\beta(T)]^2\,dT \tag{3.7}$$

where B, ν and β are the temperature-dependent bulk modulus, specific volume and coefficient of volume thermal expansion. We evaluated equation 3.7 at 300 K using our measured coefficients of volume thermal expansion: $36 \pm 2 \times 10^{-6}K^{-1}$ for austenite and $30 \pm 2 \times 10^{-6}K^{-1}$ for martensite. Values for B and ν were taken from the literature [91, 92]. Lacking data on the temperature dependence of B, ν and β, we assume them constant. The anharmonic contribution to the total entropy of either state at 300 K is on the order of 0.02 k_B/atom. The anharmonic contribution to ΔS_{vib}^{m-a} is the difference between two very small numbers, and is negligible. A similar analysis provides a value of 0.05 k_B/atom for the anharmonic vibrational entropy change in austenite from 300 to 500 K. This anharmonic contribution to the entropy of the austenite is smaller than that obtained from the phonon DOS. The discrepancy

could originate with errors in β or in an exaggerated difference between the austenite phonon DOS at 300 and 570 K.

3.4.2 Premartensitic Phonon Softening

Previous neutron scattering investigations on NiTi have studied the premartensitic phonon softening of the austenite phase. It was reported that the softest mode in the [$\xi\xi$0] transverse acoustic (TA_2) phonon dispersion branch, the mode at

$$\mathbf{k}_0 = \frac{1}{3}[110]\,2\pi/a \tag{3.8}$$

softens from 4 meV at 623 K to 0 meV as the martensite transformation temperature is approached upon cooling. Our phonon DOS curves do not show this softening, but we do not expect to see it. We estimated the number of modes involved in the softening by assuming they occupied a spherical volume in k-space with a diameter equal to the width of soft phonons in the [110] TA_2 branch. We find that at most a half percent of the total number of phonons in NiTi participate in this softening, and thus the premartensitic phonon softening at $\mathbf{k}_0$ is imperceptible in the total phonon DOS. Furthermore, the relevant phonon energies lie entirely beneath the elastic peak footprint of our TOF data, so the relevant featues would have been eliminated by our stripping of the elastic peak.

3.4.3 Soft Acoustic Phonons in B2 Austenite

The martensite and austenite have very similar DOS at the highest phonon energies. The high energy cutoffs are identical, within the limits of experimental resolution. Our lattice dynamics simulations using the force constants of Table 3.2 show that the optical phonons do not account for any modes below 20 meV, but account for most of the modes above this energy. Changes in the optical modes do not have much thermodynamic significance for the martensitic transformation.

The martensite and austenite DOS differ most significantly in the low-energy region. The softer acoustic branches in B2 NiTi contribute sufficient entropy to

stabilize the austenite with respect to the martensite at modest temperatures. From the many studies of soft acoustic modes in the bcc and B2 structures [93, 94, 95, 96, 97], we know that although the TA_2 phonon branch at $\mathbf{k}_0$ undergoes the most dramatic change near the martensitic transformation, the entire [110] TA_2 phonon branch undergoes a significant softening with decreasing temperature [80]. According to Zhao and Harmon [89], the peculiar temperature behavior of this phonon branch originates with a strong coupling between its phonon modes and nested electronic states on the Fermi surface. The Fermi surface smearing that occurs with higher temperatures reduces the strength of the electronic nesting, and thus reduces the phonon softening. Nevertheless, the difference between the austenite and martensite DOS shown in figure 3.6 covers the energy range up to 17 meV, which also involves the longitudinal acoustic (LA) phonon branch.

Our lattice dynamics simulations showed that the [$\xi\xi$0] TA_2 dispersion is most sensitive to the axially-symmetric first nearest-neighbor (1nn) transverse force constant (Φ_T^{1nn}). In bcc structures, small perturbations in Φ_T^{1nn} lead to large changes in the [$\xi\xi$0] TA_2 dispersions and smaller changes in the other high symmetry acoustic phonons. In B2 structures the 1nn radial force constant, Φ_R^{1nn}, also has a large effect on the [$\xi\xi$0] LA dispersion, and small effects on the optical modes. Zhao and Harmon [89] asserted that only the [$\xi\xi$0] TA_2 and LA modes couple strongly with the nested Fermi states in NiTi, which lends credence to the suggestion that the Φ_T^{1nn} force constant displays the strongest temperature dependence in NiTi and related alloys. This phenomenon can be seen in the data of Heiming and coauthors [98], who measured phonon dispersions in bcc zirconium at 915, 1210 and 1610 °C, and fitted them to a 5^{th} nearest-neighbor Born-von Kármán model. The [$\xi\xi$0] TA_1 dispersion in bcc Zr shows the same anomalous temperature behavior as in NiTi. Furthermore, examination of their force constants for Zr, converted from tensorial to axial form, shows that Φ_T^{1nn} decreases in the sequence 0.147, 0.543 and 1.215 N/m at 1610, 1210 and 915 °C. In contrast, the first nearest-neighbor radial axial-symmetric force constant Φ_R^{1nn} stays unchanged at 24.12, 24.482 and 24.481 N/m over the same temperature range. The softening of the TA_1 and LA branches are visible in the full phonon DOS,

with the modes in the lowest energy van-Hove singularity (approximately 10% of the total) softening 2–3 meV as the temperature decreases, while the rest of the DOS remains stationary.

3.5 Conclusions

Inelastic neutron scattering measurements of the phonon DOS of NiTi were accompanied with ancillary measurements of heat capacity and thermal expansion. We developed a Born-von Kármán lattice dynamics simulation to calculate a neutron deweighting correction for the neutron-weighted austenite DOS. The correction function proved robust, and reasonably insensitive to the choice of force constants in the lattice dynamics model. There is a large entropy difference of 0.5 ± 0.05 k_B/atom between the austenite and martensite phases at the martensitic transformation temperature of NiTi. The entropy is nearly all vibrational in origin. More specifically, it originates with the relative softness of the acoustic modes of austenite compared to those of martensite. We found that the acoustic phonon branches are most sensitive to the axially symmetric first nearest-neighbor transverse force constant. Changes in this Φ_T^{1nn} could also be responsible for the mode softenings that provide the mechanism for the martensitic transformation in NiTi and in bcc Zr.

Chapter 4 The Temperature Dependence of the Phonon Entropy of Vanadium

4.1 Introduction

Although there have been many measurements of macroscopic equations of state of solids [99], there is, unfortunately, much less experimental data on the temperature and volume dependence of the phonon density-of-states (DOS). A few studies on the temperature dependencies of phonon dispersions have been performed [98, 100, 101, 102], but they were presented in the context of diffusion and kinetic mechanisms of structural phase transitions, not of phonon thermodynamics. Ultimately there should be a rationalization of macroscopic equations of state in terms of the specific changes in phonons and electrons that underlie the relationships between pressure, temperature, and volume. The present investigation was undertaken to help identify the individual thermal contributions to the entropy of phonons and electrons.

Calculations of the electron entropy and its effect on heat capacities of transition metals were reported by Eriksson, Wills and Wallace [7]. By calculating the full electronic entropy, S_{el}, and using heat capacity data and phonon DOS measurements in the literature, these authors deduced the phonon anharmonicity from the simple relationship for the total entropy, S_{tot}:

$$S_{tot} = S_{el} + S_{har} + S_{anh} \tag{4.1}$$

where S_{har} is the harmonic phonon entropy. This S_{har} originates from the part of the phonon DOS that is unchanged with temperature. The anharmonic contribution, S_{anh}, originates with the temperature-dependence of the phonon DOS, and is typically represented by cubic and quartic terms in the interatomic potentials that lead to

phonon-phonon scattering and shifts in the energies of individual phonon states. The "quasi-harmonic" approximation used in this paper captures most of the effect of anharmonicity on the phonon entropy of a solid. This approximation assumes harmonic vibrations, but with a phonon DOS characteristic of the elevated temperature.

Vanadium is an ideal element for measuring a phonon DOS because it scatters neutrons incoherently and has a cubic crystal structure. These properties allow its phonon density of states (DOS) to be obtained rigorously from inelastic neutron scattering spectra. A recent measurement of the phonon DOS of vanadium at ambient conditions [1] was undertaken with little complication, and many previous measurements have been performed with generally good success [103, 104, 105, 106, 107, 108, 109, 110, 111, 112, 113, 114, 115]. Using similar techniques, we measured the phonon DOS of vanadium at 293, 873, 1273 and 1673 K. We assess the thermal broadening of the phonon DOS, and interpret it as phonon lifetime broadening. We also assess the temperature dependence of the phonon DOS in terms of the phonon softening predicted under thermal expansion. This volume dependence of the phonon DOS overestimates significantly the observed thermal softening of the DOS. A pure temperature dependence of the phonon DOS, comparable in size to the volume dependence, is deduced. Using phonon data from the literature, we perform similar assessments of the anharmonic contributions to the entropy of chromium, niobium, titanium and zirconium.

4.2 Experimental

Vanadium slugs of 99.9% purity were arc melted into 7 button ingots of 10 g mass. The ingots were stacked vertically within a thin-walled vanadium can to provide a sample with cylindrical geometry, prior to mounting within an AS Scientific furnace that was kept under high vacuum for all measurement. Inelastic neutron scattering spectra were measured on the HB2 and HB1 triple-axis spectrometers at the HFIR research reactor at Oak Ridge National Laboratory. The magnitude of the scattering vector Q and final neutron energy E_f were fixed at 4.6 $Å^{-1}$ and 14.8 meV. The incident

neutron energy was varied to provide an energy transfer from 50 to −2 meV. A total of 7 scans on the HB2 spectrometer were taken at temperatures of 293, 873 and 1273 K, including an empty furnace measurement at 293 K. Two more scans were taken on the HB1 spectrometer at 293 and 1673 K. The spectrometer energy resolution was estimated as 1 meV.

4.3 Analysis and Results

4.3.1 Phonon Density of States

The individual scans were corrected for the scattering from the furnace using the empty-can runs. The data below 2 meV were dominated by the large elastic peak, but this peak was easily deleted. The raw data are featureless and linear in energy transfer at low energies, which allowed for the inelastic portion of the scattering below 2 meV to be estimated. Data so corrected were analyzed in the incoherent approximation to obtain the phonon DOS. Our iterative procedure generates a self-consistent multiphonon scattering contribution, and for an incoherent scatterer with cubic symmetry it involves no approximations [88]. An advantage of a triple axis scan is that the scattering vector **Q** is fixed, so the **Q**-dependence of the energy transfer is eliminated. The **Q**-space is sampled over only a very small range, but for an incoherently-scattering sample this does not pose a problem, and the phonon DOS can be extracted reliably. The final phonon DOS curves are shown in figure 4.1.

4.3.2 Vibrational Entropy

In the quasi-harmonic approximation the phonon DOS at temperature T and volume V, $g_{T,V}(E)$, provides the the phonon entropy at temperature T, $S_{ph}(T)$:

$$S_{ph}(T) = -3\,k_B \int_0^\infty g_{T,V}(E)\,[(n_E+1)\ln(n_E+1) - n_E \ln(n_E)]\,dE \qquad (4.2)$$

where n_E is the Bose-Einstein distribution at temperature T. A generalized version

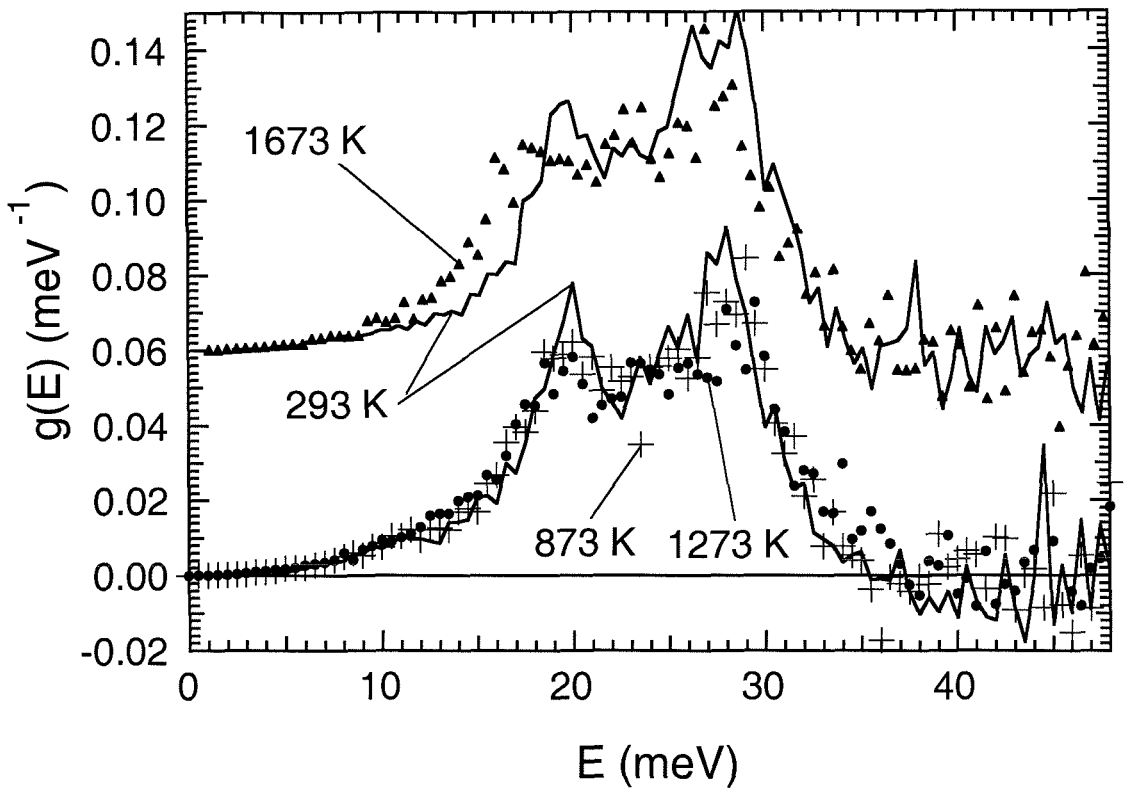

Figure 4.1: Phonon DOS of vanadium at 293, 873, 1273 and 1673 K. Temperatures are as labeled. Measurements at 293, 873 and 1273 K were taken on spectrometer HB2, shown in the bottom half of figure. Measurements taken on spectrometer HB1 at 1673 and again at 293 K are shown in the top half of figure.

of equation 4.2 provides $S_{ph}(V, T_i, T_j)$, where the phonon DOS $g_{T_i,V}(E)$ is measured at temperature T_i and volume V, and n_E is evaluated at temperature T_j.

A conventional textbook analysis of anharmonic behavior reconciles the observed softening of the phonon DOS with the thermal expansion. This is done by minimizing a free energy comprising a positive elastic energy from expansion against the bulk modulus, and a phonon entropy that increases as the phonon DOS softens under thermal expansion. This anharmonic entropy is

$$S_{ph}^{\Delta V,\Delta T}(T_1) = S_{ph}(V_1, T_1, T_1) - S_{ph}(V_0, T_0, T_1) \tag{4.3}$$

where the entropies on the right-hand side are obtained from phonon DOS curves measured at volumes and temperatures V_1, T_1 and V_0, T_0. Using our experimentally-determined phonon DOS curves, the results for vanadium are shown as the crosses in

figure 4.2, where $T_0 = 293\,K$, V_0 is the volume at 293 K, and T_1 is along the abscissa. The near-zero values at 873 and 1273 K reflect the negligible shifts in the vanadium phonon DOS between 293 and 1273 K. The large value of $S_{ph}^{\Delta V,\Delta T}$ at 1673 K originates with the large softening of the DOS between 1273 and 1673 K (seen in figure 4.1). The uncertainty in the values of $S_{ph}^{\Delta V,\Delta T}$ are from counting statistics.

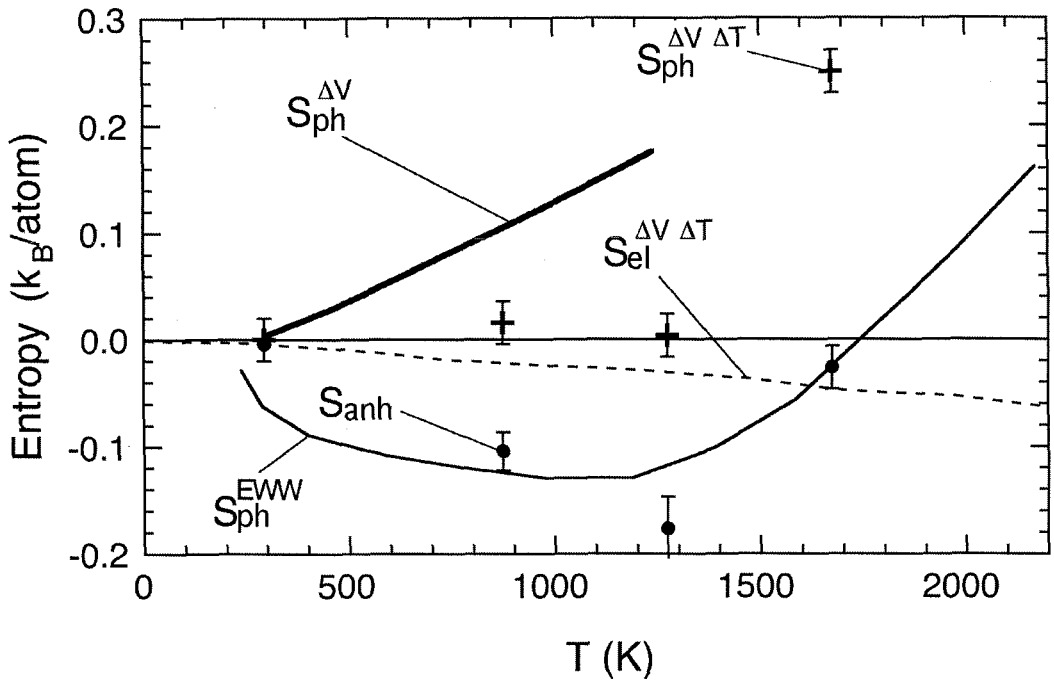

Figure 4.2: Anharmonic entropy contributions to V. Bold curve is as computed from equation 4.5. Crosses are computed from the phonon DOS of vanadium using equation 4.3. The solid circles are the difference between the bold curve and the crosses (the solid circle at 1673 K is obtained by extrapolating the bold curve to higher temperatures). The solid curve is the quantity of equation 4.10. The other curves are labeled with notation used in the text.

A similar quantity, $S_{tot}^{\Delta V,\Delta T}$, can be calculated for the total thermodynamic entropy. Like the anharmonic phonon entropy, it originates with the thermal expansion against the bulk modulus, but includes the effects of thermal expansion on all entropy contributions, including the electronic ones. Classical thermodynamics provides the relationship between the heat capacities at constant pressure and volume, C_P and C_V, which when divided by T and integrated from T_0 to T_1 gives

$$S_{tot}(V_1, T_1) - S_{tot}(V_0, T_1) = \int_{T_0}^{T_1} B\, v\, \beta^2\, dT \tag{4.4}$$

where B, v and β are, respectively, the bulk modulus, the specific volume and the coefficient of volume thermal expansion. The quantity $S_{tot}(V, T)$ is the total entropy at volume V and temperature T, and $V(P, T')$ is the volume at fixed pressure P and temperature T'. Thus $V_1 = V(P, T_1)$ and $V_0 = V(P, T_0)$. Equation 4.4 accounts for the volume dependence of the total entropy, not just the phonon entropy. Subtracting an electronic contribution, $S_{el}^{\Delta V, \Delta T}$, we obtain:

$$S_{ph}(V_1, T_1) - S_{ph}(V_0, T_1) = \int_{T_0}^{T_1} B\, v\, \beta^2\, dT - S_{el}^{\Delta V, \Delta T} \tag{4.5}$$

We rewrite equation 4.5 with the generalized notation presented earlier:

$$S_{ph}(V_1, T_1) - S_{ph}(V_0, T_1) = S_{ph}(V_1, T_1, T_1) - S_{ph}(V_0, T_1, T_1) \tag{4.6}$$

$$\equiv S_{ph}^{\Delta V}(T_1) \tag{4.7}$$

The electronic term, $S_{el}^{\Delta V, \Delta T}$, is the difference in electronic entropy at constant pressure versus constant volume over the temperature range ΔT. It is obtained by comparing the electronic density of states at V_0, T_0 with that at V_1, T_1. This electronic term is typically small compared to the total anharmonic entropy, and can have either positive or negative sign. Evaluating $S_{ph}^{\Delta V}$ for elemental vanadium using variables taken from the literature [75], we obtain the bold curve in figure 4.2. The electronic term in equation 4.5 was calculated using the electronic Grüneisen parameters provided by Eriksson, Wills and Wallace [7], with the experimental thermal expansion. It is shown as the dashed curve in figure 4.2.

The discrepancy between the bold curve and the crosses on figure 4.2 is quite large up to 1273 K. A comparison of equations 4.7 and 4.3 shows that the discrepancy between $S_{ph}^{\Delta V, \Delta T}(T_1)$ and $S_{ph}^{\Delta V}(T_1)$ likely originates with the difference between the quantities $S_{ph}(V_0, T_1, T_1)$ and $S_{ph}(V_0, T_0, T_1)$. The significance of this difference is

discussed in section 4.4.2.

4.3.3 Phonon Broadening

One effect of temperature on phonons is to reduce their lifetimes, and thus broaden their energies. This is commonly attributed to increased phonon-phonon scattering due to the increase in phonon occupations at high temperature. This energy broadening is observed in the DOS as a general smearing of features such as van Hove singularities and the high energy cutoff [116]. The energy broadening of a single phonon mode at energy ϵ is expected to have the form of a damped harmonic oscillator, $D_{\epsilon'}(\epsilon)$

$$D_{\epsilon'}(\epsilon) = \frac{1}{\pi \mathcal{Q} \epsilon'} \frac{1}{(\frac{\epsilon'}{\epsilon} - \frac{\epsilon}{\epsilon'})^2 + \frac{1}{\mathcal{Q}^2}} \tag{4.8}$$

The only free parameter in equation 4.8 is $\mathcal{Q}$, the quality factor of the oscillator. Convolving equation 4.8 with the DOS obtained at the lowest temperature of 293 K, we adjusted $\mathcal{Q}$ to give the best fit to the DOS obtained at 873 and 1273 K. Figure 4.3 shows the excellent agreement between the measured 873 and 1273 K DOS curves and the best fits generated by broadening the 293 K DOS with equation 4.8. Figure 4.4 shows the optimal (inverse) $\mathcal{Q}$ versus temperature. The behavior of inverse $\mathcal{Q}$ as a function of temperature shows a large broadening of phonon energy with rising temperature, but we cannot state conclusively that the temperature dependence is linear or quadratic.

4.4 Discussion

4.4.1 Phonon DOS Curves

Figure 4.5 shows that our phonon DOS of vanadium at 293 K agrees well with the earlier result of Sears, Svensson and Powell [1]. We do not find the small peak at 5 meV seen by Sears, et al., but this is a small feature about which these investigators

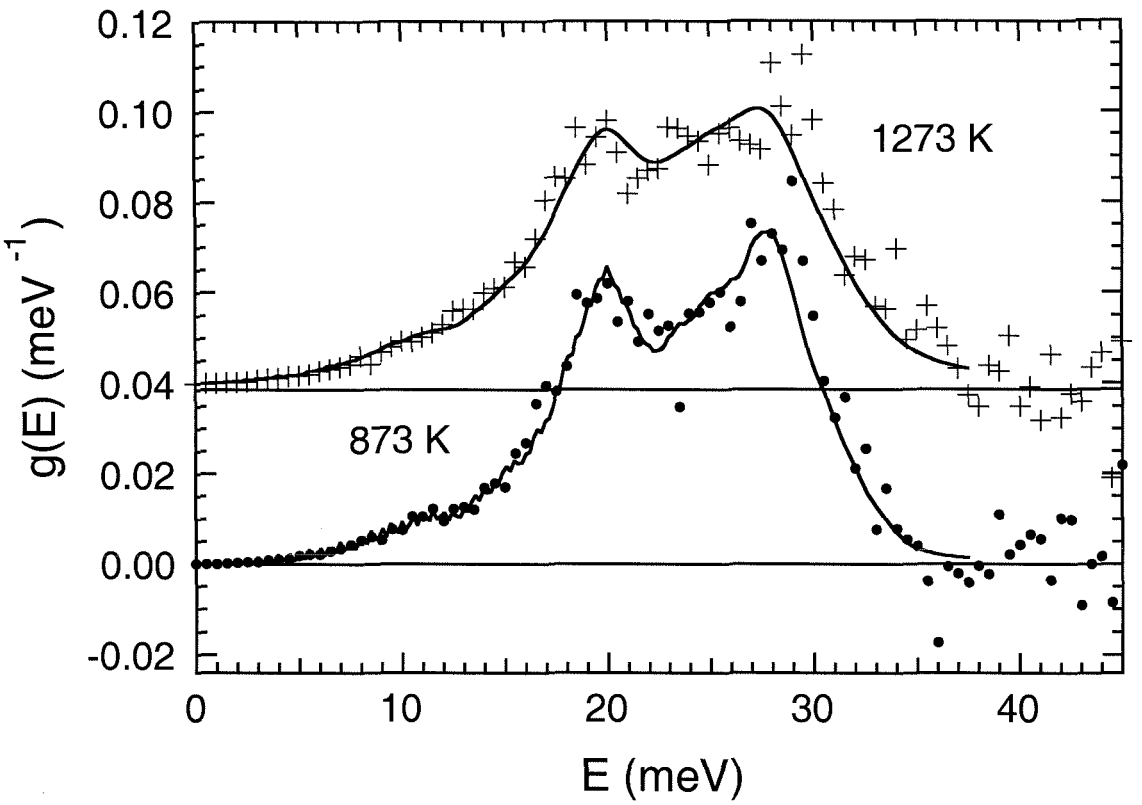

Figure 4.3: Symbols are phonon DOS of vanadium at 873 and 1273 K. Solid curves are 293 K DOS broadened by convoluting with the damped harmonic oscillator function of equation 4.8.

were uncertain. The phonon DOS of vanadium is essentially constant up to 1273 K, subject only to broadening. Between 1273 and 1673 K, the DOS undergoes a large softening in energy. The temperature behavior of the DOS is inconsistent with what is expected from equation 4.5, which suggests that the DOS should soften gradually between 293 and 1673 K.

4.4.2 Anharmonic Entropy

The high temperature behavior of the vanadium phonon DOS is troubling because it is inconsistent with the predicted increase in volumetric phonon entropy, $S_{ph}^{\Delta V}$, given by equation 4.5. This discrepancy can be accounted for on the basis of the difference between equations 4.3 and 4.5. A difference between $S_{ph}^{\Delta V}(T)$ and $S_{ph}^{\Delta V,\Delta T}(T)$ requires an explicit temperature dependence of the phonon DOS, countering the common

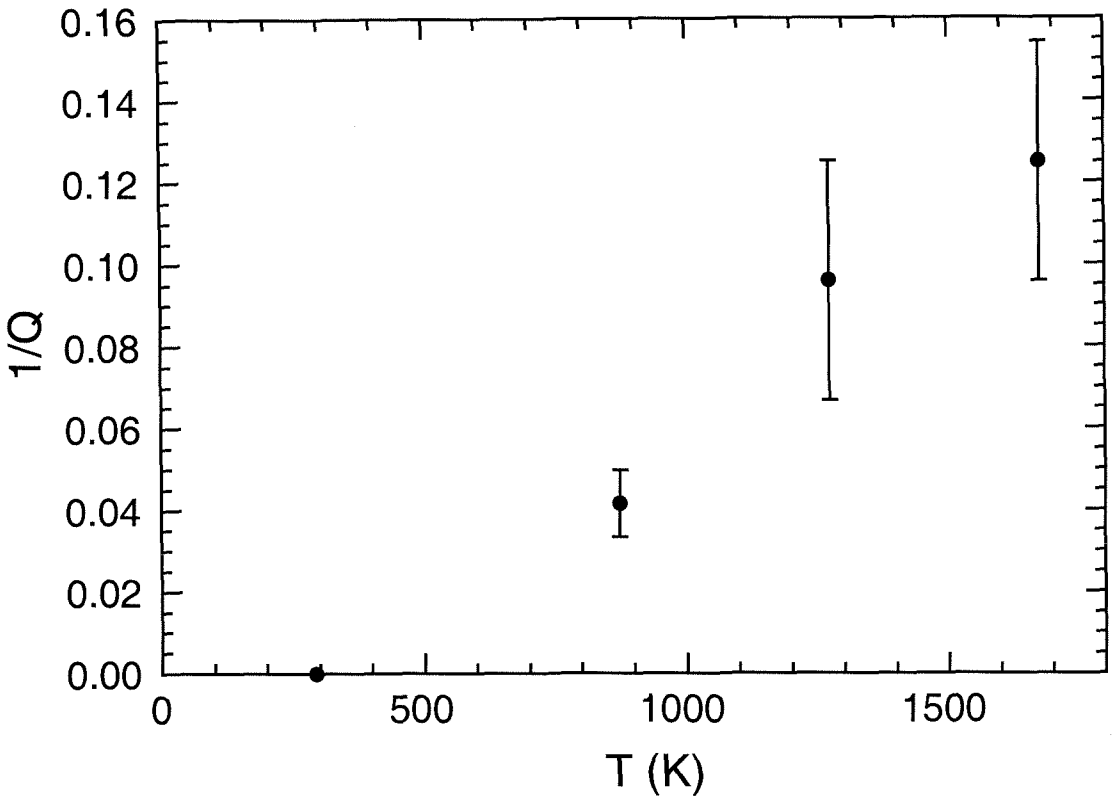

Figure 4.4: Best-fit inverse $\mathcal{Q}$ versus temperature.

assumption that phonon frequencies depend only on volume. For vanadium a temperature dependence of the phonon DOS is needed to reconcile the negligible phonon softening of the DOS with that expected from thermal expansion.

The difference between equations 4.3 and 4.7 is the entropy overlooked by ignoring the temperature dependence of the DOS. We call it S_{anh}, where

$$S_{anh}(T_1) = S_{ph}(V_0, T_1, T_1) - S_{ph}(V_0, T_0, T_1) \tag{4.9}$$

Equation 4.9 is nonzero only if $S_{ph}(V, T, T')$ has a functional dependence on T. This occurs only if the phonon DOS varies with temperature at a fixed volume. The quantity S_{anh} is plotted as the solid circles on figure 4.2, and is the difference between the crosses and the bold solid curve of figure 4.2.

Eriksson, Wills and Wallace used a different approach to obtain the anharmonic vibrational entropy of elemental vanadium at high temperature [7]. They calculated

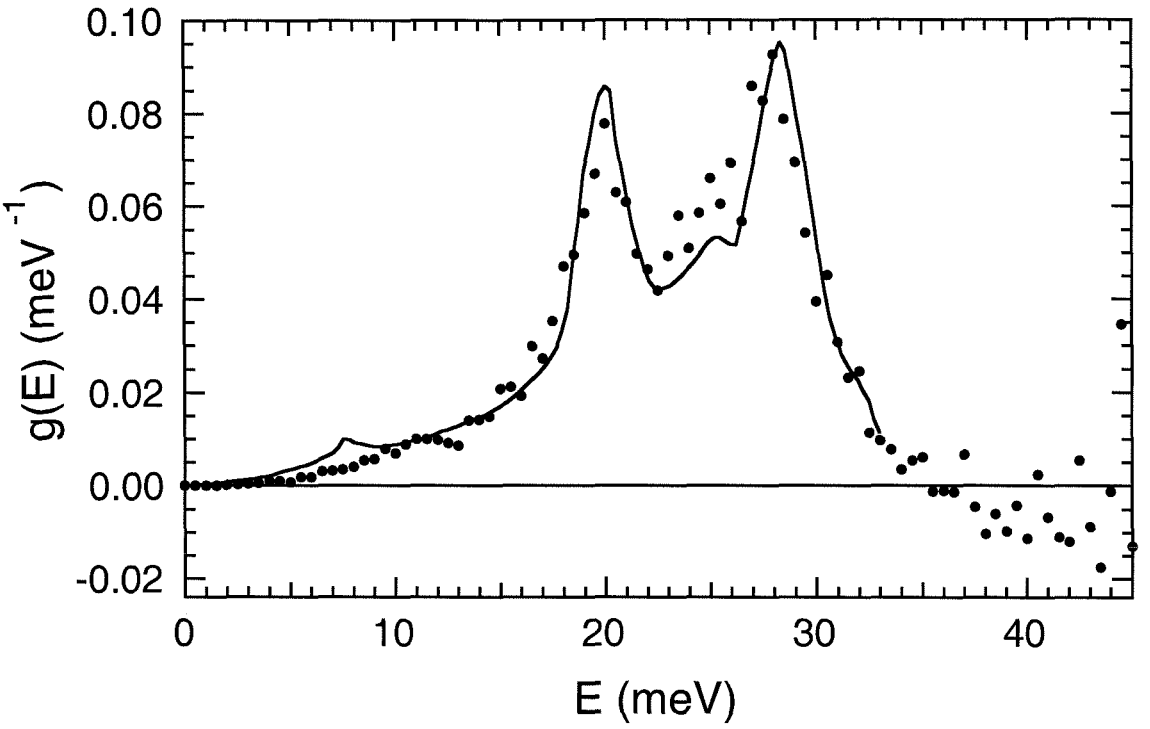

Figure 4.5: Phonon DOS of vanadium at 293 K. Present data are the solid circles and solid curve is from Sears, et al. [1].

the electronic entropy from first principles, and obtained the harmonic vibrational entropy from a volume-corrected phonon DOS taken from the literature. By subtracting the electronic and vibrational entropy contributions from calorimetric measurements of the total entropy, they arrive at the anharmonic entropy:

$$S_{anh}^{EWW}(T_1) = S_{ph}(V_0, T_1, T_1) - S_{ph}(V_0, 0, T_1) \tag{4.10}$$

Equations 4.9 and 4.10 are near-identical, differing only insofar as the temperature T_0 differs from zero. The anharmonic entropy calculated by Eriksson, Wills and Wallace is shown as the thin solid curve in figure 4.2. The quantity S_{anh} of equation 4.9 is shown as the solid circles in figure 4.2. In principle, the two curves should differ only insofar as the phonon DOS of vanadium differs between 0 and 293 K. We note that the solid circles and the thin solid curve coincide almost exactly. This agreement between equations 4.9 and 4.10 is impressive, considering that S_{anh} was constructed using a temperature-dependent phonon DOS and measured elastic constants, whereas

S_{anh}^{EWW} was derived from heat capacity data and electronic structure calculations. The calculation by Eriksson, Wills and Wallace even captures the large softening of the phonon DOS near 1673 K — Eriksson's curve goes from negative to positive near this temperature.

Eriksson, Wills and Wallace's work lends support to our assertion that the stationary behavior of the phonon DOS of vanadium up to 1273 K is caused by a pure temperature dependence of the phonon energies. The strongly-positive bold curve in figure 4.2 (from classical thermodynamics with a small correction for electronic entropy) shows that expanding the crystal volume at constant temperature causes a softening of the phonon DOS. The phonon DOS of vanadium is nearly unchanged up to 1273 K, however, even though the crystal expands. We therefore conclude that the volume and temperature effects on the phonon energies are nearly equal and opposite from 293 to 1273 K. The phonon DOS of vanadium hardens with increasing temperature at fixed volume. The most likely source of a pure temperature effect on the phonon energies is phonon-phonon scattering because $S_{anh} \simeq S_{anh}^{EWW}$, and S_{anh}^{EWW} is unambiguously identified as originating with phonon anharmonicity.

4.4.3 Chromium, Niobium, Titanium and Zirconium

Results from a number of investigations performed over the past decade suggest similar or related behavior in other bcc transition metals at high temperature. The behavior of the phonon DOS of chromium, titanium, niobium and zirconium at high temperature are all in disagreement from what is expected from measured thermal expansions, even when corrected for the electronic entropy. These discrepancies can be quantified by taking the difference of equations 4.7 and 4.3. This difference is S_{anh}, as calculated in equation 4.9. The values of S_{anh} for these elements, shown on figure 4.6, are nonzero and increase monotonically with temperature.

A high-temperature DOS consistent with equation 4.5 would yield negligibly small values of S_{anh}. Evaluating equation 4.5 required the use of thermal expansion coefficients taken from the literature [75] and elastic constants extracted from the phonon

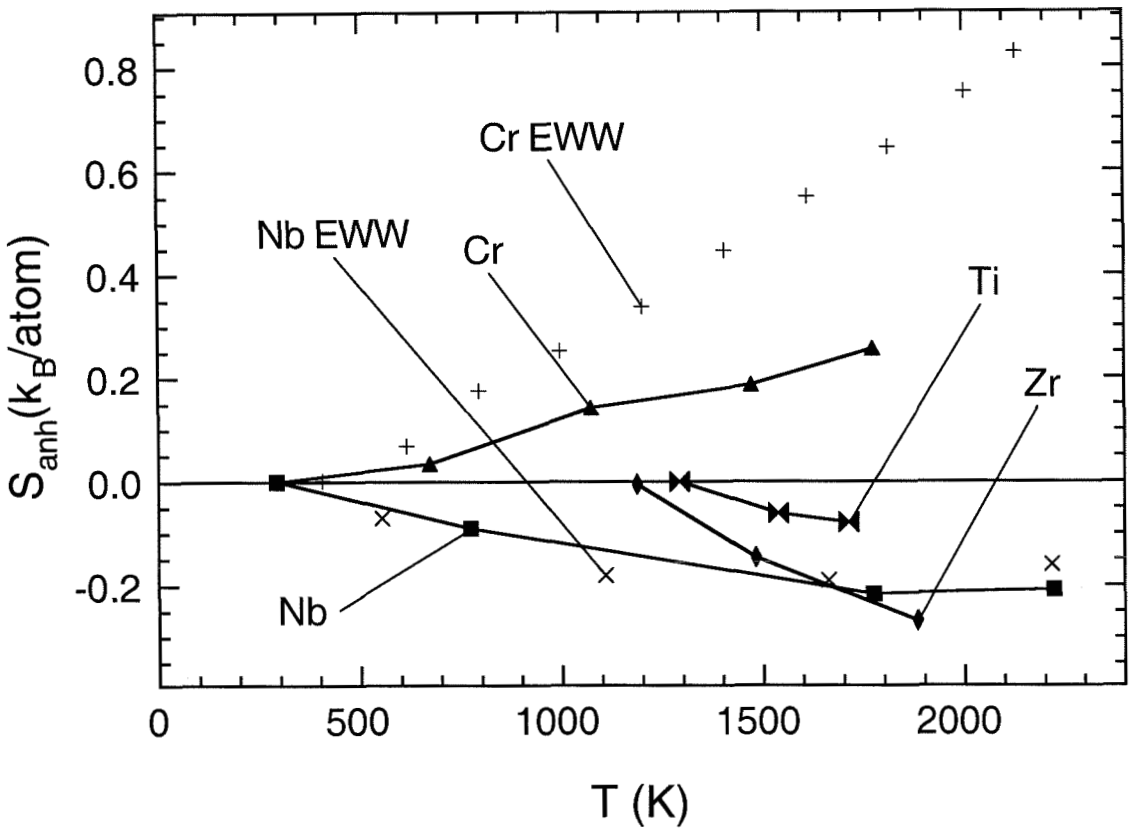

Figure 4.6: Anharmonic entropy of elemental chromium, niobium, titanium and zirconium as calculated from equation 4.9. Results labeled "EWW" are from Eriksson, Wills and Wallace [7].

.

dispersion measurements.

Measurements by Heiming and coworkers [98] showed that the phonon DOS of bcc zirconium hardens significantly with increasing temperature (figure 4.7). Evaluation of equation 4.5 for bcc zirconium suggests, however, that the phonon DOS should exhibit the opposite behavior. The discrepancy can be quantified with the anharmonic entropy of equation 4.9, shown in figure 4.6. The electronic anharmonic entropy needed for equation 4.5 is unavailable for zirconium. Although our evaluation of equation 4.9 for zirconium neglects this term, we expect it to change our result by at most 25 %, as estimated from niobium. The vibrational anharmonic entropy, S_{anh}, of zirconium is large and negative in the high temperature bcc phase. A large thermal hardening of the phonon DOS at constant volume is required to explain the temperature-dependence of the phonon DOS. Our conclusion is supported by ab-initio

calculations of the effect of phonon-phonon scattering on the energies of five unstable phonon states in bcc Zr [117]. Ye and coauthors showed that fourth order phonon anharmonicites made enormous positive shifts to the energies of selected modes at high temperature.

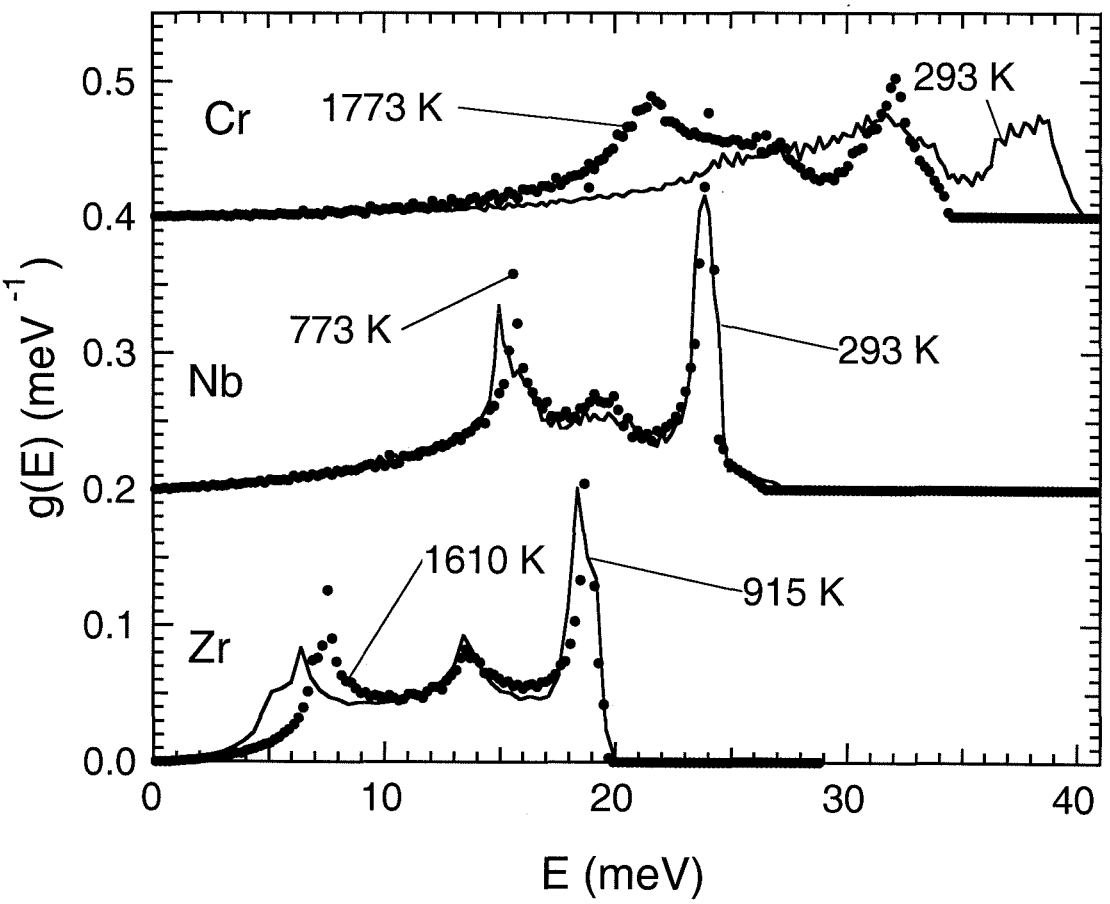

Figure 4.7: Phonon DOS of bcc zirconium, niobium and chromium at various temperatures from Heiming, et al. [98], Güthoff, et al. [100] and Trampenau, et al. [101]. The DOS are offset vertically for clarity.

Similar but less complete work on bcc titanium [102] also shows anomalous temperature behavior — the phonon DOS of bcc titanium hardens noticeably between 1208 and 1713 K. Evaluating equation 4.9 for titanium gives the anharmonic entropy shown in figure 4.6. The anharmonic entropy of bcc titanium is negative, and about half the size of that of zirconium, which lies in the same column of the periodic table. The unknown electronic contribution to equations 4.5 and 4.9 could modify our result substantially, but probably not qualitatively.

The phonon dispersions and DOS of bcc niobium at high temperature are also available from the literature [100]. A close examination of the temperature-dependent DOS in bcc niobium, reproduced in figure 4.7, shows that many acoustic modes near 15 meV harden significantly between 293 and 773 K. Accordingly, the agreement between equations 4.5 and 4.3 is poor, and the anharmonic entropy calculated with equation 4.9 is substantially negative. The electronic contribution to equation 4.5 was calculated using the DOS and electronic Grüneisen parameters provided by Eriksson, Wills and Wallace [7]. Our result is in excellent agreement with the previous estimates by Eriksson, Wills and Wallace [7], as marked in figure 4.6. The temperature behavior of the niobium DOS is very similar to that of vanadium, with little change up to 1000 K. (Vanadium and niobium both lie in the same column of the periodic table.) The case of niobium is important because it points out that the average phonon energy shifts, as inferred by evaluating equations 4.5 and 4.9, can be quite different from the energy shifts of individual phonon modes. For the case of bcc niobium, a large number of transverse phonons harden with temperature, but a similar number of longitudinal phonons soften with temperature, leading to zero average shift of phonon energies.

The phonon DOS of bcc chromium has been measured from 293 to 1773 K [101]. In contrast with zirconium and titanium, the DOS of chromium softens enormously over this temperature range, as shown in figure 4.7. The anharmonic vibrational entropy as calculated with equation 4.3 is twice as large as that calculated from equation 4.5. The discrepancy is accounted for by the explicit temperature dependence of the phonon energies. For chromium, however, this is a pure thermal softening of the DOS, instead of the hardening that occurs for vanadium, niobium, zirconium and titanium. The anharmonic entropy of bcc chromium as given by equation 4.10 was calculated by Eriksson, Wills and Wallace [7], and is shown in figure 4.6 as solid crosses. The electronic contribution to equation 4.5 was calculated using the DOS and electronic Grüneisen parameters provided by Eriksson, Wills and Wallace [7]. The anharmonic entropy calculated using equation 4.9 is shown in figure 4.6. Our result is half that obtained by Eriksson, et al., but we are encouraged by the agreement in sign and

magnitude. Perhaps local magnetic effects play a role in the thermodynamics of chromium, even at these high temperatures.

4.5 Conclusions

The phonon DOS of bcc vanadium was measured using the time-of-flight triple axis spectrometers on the HB2 and HB1 beam lines on the HFIR reactor at the Oak Ridge National Laboratory. The DOS showed little change up to 1273 K, and a large softening at 1673 K. The behavior of the phonon DOS leads us to conclude that volume expansion and rising temperature exert equal and opposite shifts in the phonon energies up to 1273 K. In practice, the phonon DOS depends as strongly on temperature as it does on volume. The most likely physical explanation for this pure temperature dependence is phonon-phonon scattering. Similar effects are also found by analyzing previous high-temperature data on bcc chromium, zirconium, niobium and titanium.

4.6 Acknowledgements

This work was supported by the U.S. Department of Energy under contract DE-FG03-96ER45572 and BES-MS, W-31-109-ENG-38.

Chapter 5 The Vibrational Entropy of Alloying and Ordering in Cu-Au

5.1 Introduction

5.1.1 Alloying in Cu-Au

The Cu-Au binary alloy system has long been of interest in the study of metals. Cu and Au form a face-centered cubic (fcc) single-phase solid solution at arbitrary compositions. Near the compositions Cu_3Au, CuAu and $CuAu_3$ the stable phase at low-temperature is a chemically ordered one: $L1_0$ for CuAu and $L1_2$ for the remaining two. The chemical ordering can be suppressed by quenching the alloys from high temperature. The ordering transformations in Cu-Au have made it a model system for both theoretical and experimental studies of ordering. Early interest in ordering has also led to the study of many different properties in Cu-Au: elastic constants [118], heat capacity [119] and lattice dynamics [56]. These studies have focused upon the differences between the ordered and disordered phases at specific compositions. Among these studies is a recent measurement of the vibrational entropy of ordering in Cu_3Au using low-temperature heat capacity [37]. There has been no study focused exclusively on the vibrational entropy of the chemically disordered phase. The presence of a common chemically disordered phase throughout the phase diagram of Cu-Au allows for a model experiment: we can measure the composition dependence of the vibrational entropy in the absence of changes in crystal structure and chemical order. Because this phase is chemically-disordered, the study offers challenges and opportunities.

The presence of chemical disorder presents enormous difficulties to computational and theoretical studies. Without long-range chemical order, Bloch's theorem no

longer applies and states (electronic and vibrational) can no longer be labeled by wave-vector. Without the simplifications allowed for by Bloch's theorem, and in the presence of unknown local relaxations, true *ab-initio* calculations are prohibitively expensive and methodologically uncertain. Presently, *ab-initio* efforts to calculate the electronic energy (a pre-requisite to calculating the phonon energies) of the disordered phase use a number of approximations. Approximations such as the special quasi-random structure (SQS) [14] or the cluster variation model [10] attempt to match the short-range chemical correlations present in the disordered phase using calculations done on chemically ordered phases. These approaches introduce errors of unknown magnitude because not all chemical correlations are included in the matching process. Empirical models such as the embedded-atom method (EAM) overcome these obstacles by performing calculations on large chemically disordered supercells, including local relaxations. However, these calculations are only as good as the potential model being used. Typically, the EAM method gives good results for some alloy properties but poor results for others. In the absence of a reliable theory, experiments on chemically-disordered alloys are especially important.

The measurement of the vibrational entropy in chemically-disordered Cu-Au presents challenges not encountered in chapters 2, 3 and 4. The presence of chemical disorder disallows the use of a Born-von Kármán model to extract the DOS and entropy from triple-axis measurements of the phonon dispersions, as was done in chapter 2. Cu and Au are strong coherent scatterers of neutrons, and this prevents us from measuring the phonon DOS directly using a triple-axis spectrometer, as we did in chapter 4. In this alloy system with strong chemical disorder, the instrument of choice is a time-of-flight (TOF) spectrometer. However, Cu phonons scatter neutrons more than three times as efficiently as Au phonons, which gives rise to the problematic neutron-weight correction to the phonon DOS. A very similar difficulty was observed in chapter 3 with NiTi, which was solved using Born-von Kármán lattice dynamics to estimate the neutron-weight correction. The presence of chemical disorder prevents us from following the same approach with Cu-Au. Much of this chapter is devoted to developing a reliable methodology for deriving the vibrational entropy from the

neutron-weighted phonon DOS. In the process, we learn much about the *composition* dependence of the partial vibrational entropies of Cu and Au.

5.1.2 Ordering in Cu_3Au

Alloys near the composition Cu_3Au undergo an order-disorder transition at high temperature. The low-temperature phase has the ordered $L1_2$ structure, while the high temperature phase is a chemically disordered face-centered cubic (fcc) phase. In both cases the parent lattice is fcc. The first-order transition from chemical order to disorder occurs at 390 °C. This critical temperature (T_c) is determined by the energy and entropy difference between the two phases. The energy difference between the two phases can be estimated by modern electronic structure calculations (more accurately for the ordered than disordered phase), and the *configurational* entropy is well understood through cluster-variation calculations or Monte-Carlo simulations. The vibrational component of the transition entropy, ΔS_{vib}^{ord}, is less accessible by theory. Nagel, Anthony and Fultz obtained a ΔS_{vib}^{ord} value of 0.14 ± 0.05 k_B/atom at 300 K using low-temperature calorimetry, where

$$\Delta S_{vib}^{ord} = S^{dis} - S^{ord} \tag{5.1}$$

and S^{dis}, S^{ord} are the entropies of the disordered and ordered phases. Using a Born-von Kármán model with force constants taken from phonon dispersion measurements of the ordered and disordered phases [56], the phonon entropy difference ΔS_{vib}^{ord} is estimated as 0.23 k_B/atom at 300 K. This measurement by Katano is the most direct, yet suffers seriously from the use of the virtual-crystal approximation to interpret the disordered phase lattice dynamics within the Born-von Kármán model. The calorimetric measurement has a large uncertainty that stems from the difficulty of measuring the difference in heat capacities of the two phases. Ozoliņš, Wolverton and Zunger calculated a ΔS_{vib}^{ord} value of 0.06 k_B/atom at 300 K using the cluster-variation method to model the vibrational entropy of the disordered phase from *ab-inito* calculations of the lattice dynamics of ordered Cu-Au phases. Both experimental

values are substantially larger than the value calculated by Ozoliņš, Wolverton and Zunger. However, the vibrational entropy difference at 300 K is not necessarily the same as the vibrational entropy difference at T_c. The vibrational entropy difference within the quasiharmonic approximation is a function of the phonon DOS, and the phonon DOS of either or both phases change as the phases expand and absorb heat between 300 and 663 K. If the phonon DOS of the two phases change unequally, then the vibrational entropy difference between the two phases will not remain the same between 300 and 663 K.

The use of a time-of-flight (TOF) spectrometer to measure the differences in vibrational entropy between the ordered and disordered phases of Cu_3Au has distinct advantages and distinct challenges. Through our measurement of the phonon excitations, our value of the phonon entropy is more direct than calorimetry. Additionally, by direct measurement of the phonon spectrum, we avoid the use of a Born-von Kármán model and the unreliable virtual crystal approximation. The TOF spectrometer data can be corrected to obtain the DOS directly. The challenge for this method is the uncertain neutron-weight correction needed to obtain the phonon DOS from the neutron-weighted DOS (see section 3.3.3).

5.2 Experimental Methods

5.2.1 Disordered Cu-Au Alloys

Six Cu-Au alloys of varying composition were prepared for neutron scattering. Au shot of 99.99% purity and Cu shot of 99.999% purity were arc-melted in the right proportions as to provide ingots with composition Cu_xAu_{1-x}, where x are nominally 96, 82, 75, 68, 50 and 25 atom %. Ingots were flipped in the crucible and arc-melted repeatedly to ensure homogeneity. The ingot masses ranged from 35 to 88 g. Ingot sizes were chosen so that the final specimens would scatter less than 10% of the incident neutron beam. Total mass lost during arc-melting ranged from 0.05 to 0.02 g, and there was no evidence of a surface oxide. Without knowledge of how much Cu

and Au accounted for mass lost during melting, we are unable to quantify this effect on the final ingot composition. However, we can make a worst case estimate (assume all the mass lost came from the minority element). Doing this, we get effects on the composition x of a few parts per ten thousand. Final ingot Cu concentrations were estimated as follows: 95.99, 81.99, 67.98, 50.00 and 24.99%. For simplicity we shall refer to these concentrations by their nominal values.

Each ingot was subsequently cold-rolled to a thickness of approximately 0.76 mm. Each cold-rolled ingot was cut and assembled into a mosaic sample of uniform thickness of dimensions 7 by 9 cm, preparatory to mounting for neutron scattering. The $Cu_{50}Au_{50}$ sample was annealed briefly at 550 °C to eliminate work hardening during cold-rolling. Subsequent to final cold-rolling and cutting, each specimen was annealed for 45 minutes at 850 °C in evacuated quartz ampoules, then quenched into ice-brine to preserve chemical disorder.

Chemical order was measured by x-ray diffractometry with Co Kα radiation using an Inel CPS-120 position sensitive detector. A representative diffraction pattern of the quenched material, presented in figure 5.1, shows an fcc material with no long range order.

Inelastic neutron scattering spectra were measured with the time-of-flight (TOF) chopper spectrometer LRMECS, at the IPNS spallation neutron source at Argonne National Laboratory. All samples were encased in thin-walled Al pans for mounting in the displex refrigerator of the LRMECS spectrometer. The plates and powder samples were mounted at a 45 degree angle normal to the incident beam to minimize self shielding. Spectra with an incident energy E_i of 35 meV were measured at 300 K for all samples and an empty container. A run with a "black absorber" cadmium sheet in the sample position was measured at room temperature to improve the background correction. Detector response was calibrated with a run performed on a vanadium sample at room temperature, using broadband radiation without a fermi chopper. The instrument resolution function was determined with a vanadium run taken with $E_i = 35$ meV. The continuous detector coverage on LRMECS, ranging from 3 to 117 °, allowed a simultaneous probe of the spectral response over a large range of momentum

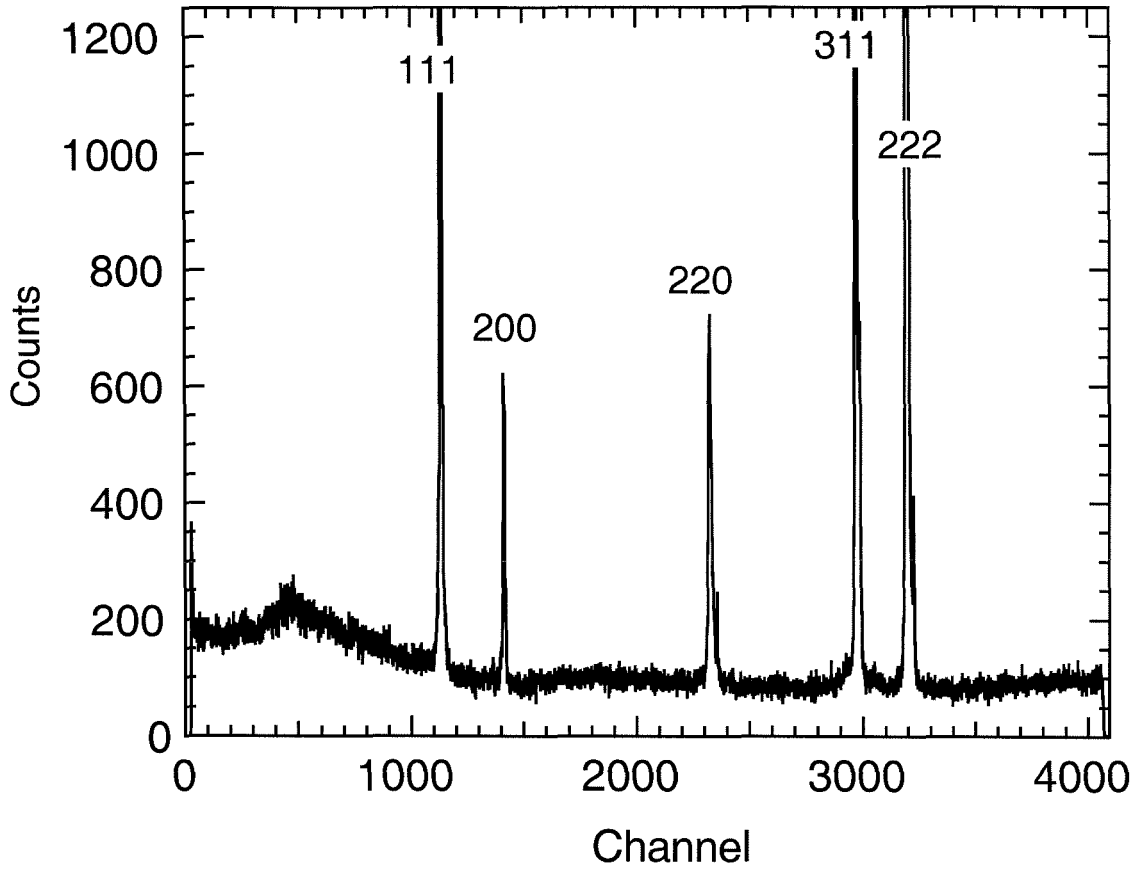

Figure 5.1: X-ray diffraction patterns of disordered $Cu_{68}Au_{32}$. Peak diffraction indices are labeled.

and energy transfer (κ, $\hbar\omega$), with $|\kappa(w)|$ varying between 0.2 and 7 Å^{-1} at zero energy transfer.

5.2.2 Ordered Cu_3Au

Neutron scattering spectra were measured on ordered and disordered Cu_3Au using the same neutron TOF spectrometer with the same incident neutron energy. Representative x-ray diffraction patterns are shown in figure 5.2. The presence of the extra (100)-family of superlattice diffractions is evident in the ordered family.

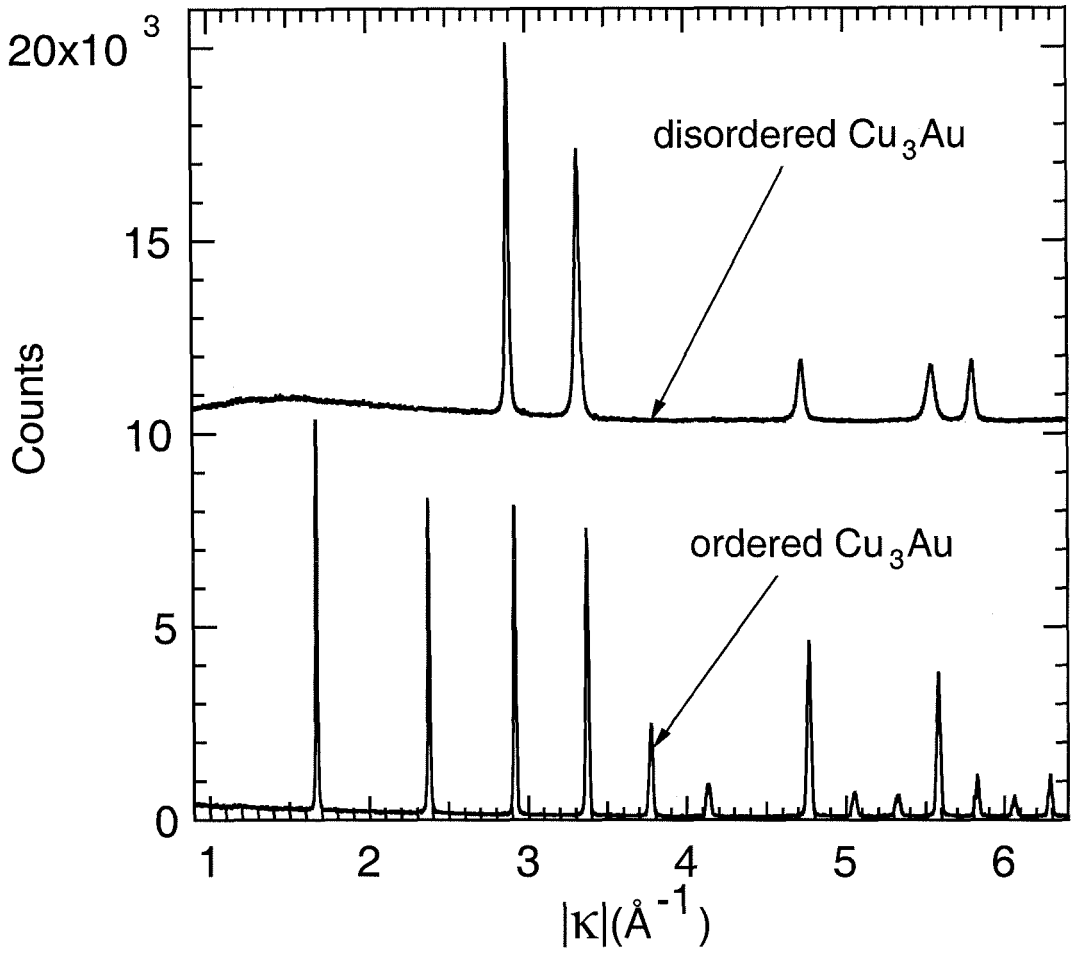

Figure 5.2: X-ray diffraction patterns of ordered and disordered Cu_3Au.

5.3 Analysis and Results

5.3.1 Phonon Density of States

All TOF spectra were first normalized and corrected for detector efficiency and time-independent background following standard procedures. In this step, the detectors were combined into groups spanning 10 ° each with average angles from 5 to 115 °. The scattering contribution of the container and spectrometer hardware to the observed spectra was determined using the runs on the empty container and Cd sample, and taking into account the sample absorption. The data below 3–4 meV are dominated by the large elastic peak, which was stripped from the data. The raw data are featureless and linear in energy transfer at small energy transfer in the hydrodynamic limit,

and thus are estimated easily. The neutron-weighted phonon density of states was determined from the corrected spectra with the procedure described in Appendix A. The final neutron-weighted phonon DOS curves are shown in figure 5.3.

The neutron-weighted phonon DOS have in principle a significant neutron-weight correction. The quotient of σ_{Cu}/m_{Cu} and σ_{Au}/m_{Au} is 3.21, which implies that some parts of the neutron-weighted DOS could be underweighted by a factor of 3.21 compared to the true phonon DOS. The neutron-weight correction, as described in equation 3.3, is different for each of the six alloys. We are unable to perform a Born-von Kármán lattice-dynamics simulation, as we did in chapter 3, because the alloys are chemically disordered. In the next section we show that the neutron-weight correction, although quite difficult for the phonon DOS, can be performed reliably and accurately for the vibrational entropy.

5.3.2 Neutron-Weighted Vibrational Entropy

Using equation 4.2, we can calculate the vibrational entropy from the phonon DOS. If we evaluate equation 4.2 using the neutron-weighted DOS instead of the true phonon DOS, we arrive at a quantity we call the neutron-weighted vibrational entropy, S_{vib}^{NW}, where

$$S_{vib}^{NW} = -3\,k_B \int_0^\infty g_{NW}(E)[(n_E+1)\ln(n_E+1) - n_E \ln(n_E)]\,dE \tag{5.2}$$

where $g_{NW}(E)$ is the neutron-weighted phonon DOS. Does the quantity S_{vib}^{NW} have any physical significance or theoretical usefulness? The answer is yes. Substituting equation 3.2 into equation 5.2 and allowing $\exp[-2(W - W_d)] = 1$, we arrive at

$$\begin{aligned} S_{vib}^{NW} &\propto -3\,k_B \int_0^\infty \sum_d g_d(E)\frac{\sigma_d}{m_d}[(n_E+1)\ln(n_E+1) - n_E\ln(n_E)]\,dE & (5.3)\\ &\propto \sum_d \frac{\sigma_d}{m_d}(-3)\,k_B \int_0^\infty g_d(E)[(n_E+1)\ln(n_E+1) - n_E\ln(n_E)]\,dE & (5.4)\\ &\propto \sum_d S_{vib}^d\left(\frac{\sigma_d}{m_d}\right) & (5.5) \end{aligned}$$

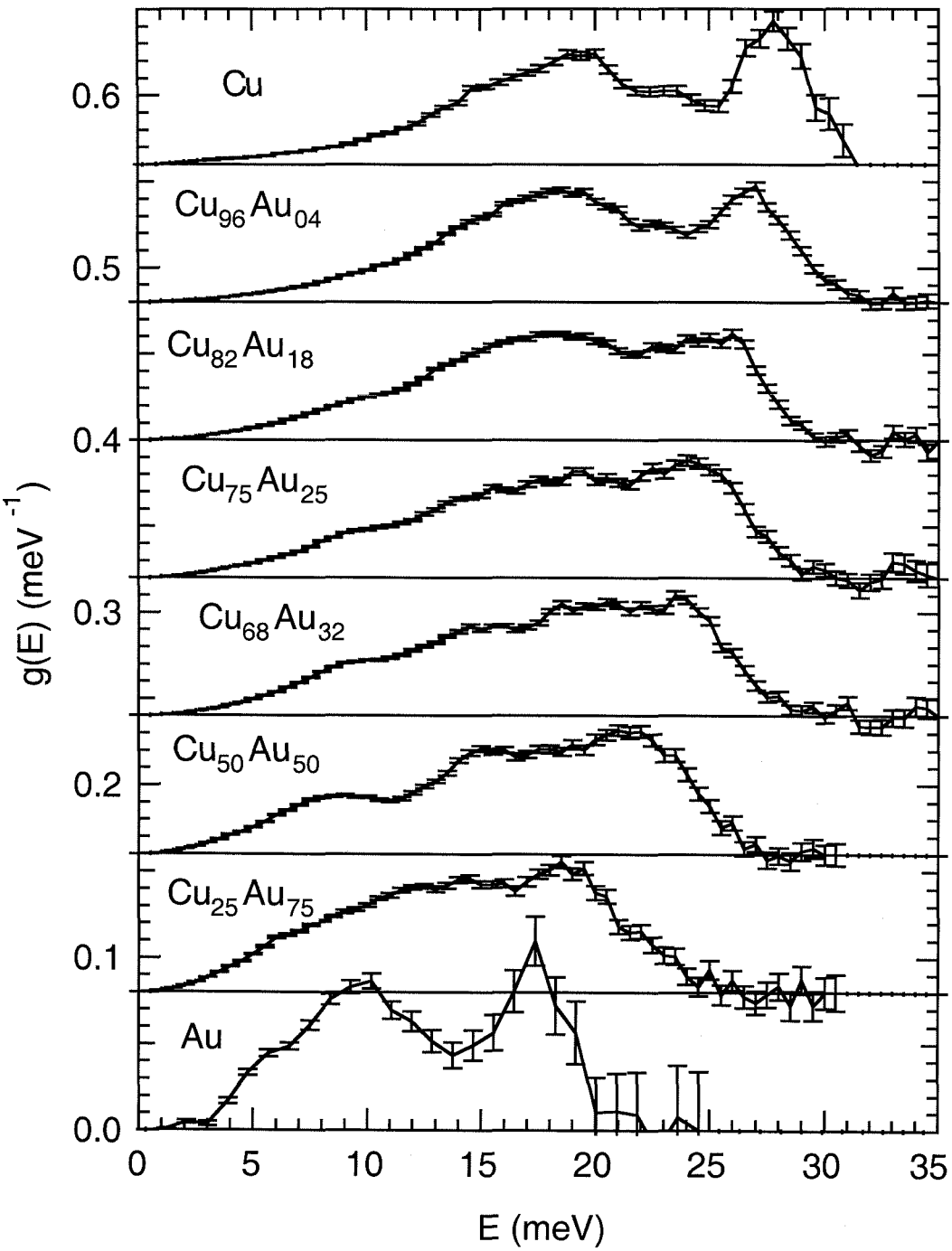

Figure 5.3: Neutron-weighted phonon DOS of disordered Cu_xAu_{1-x} alloys and elements.

where S^{d}_{vib} is the vibrational entropy of atom d. By definition $S^{total}_{vib} = \sum_{d} S^{d}_{vib}$. For the case of Cu_xAu_{1-x}

$$S^{NW}_{vib} = C\left(3.21S^{Cu}_{vib}(x) + S^{Au}_{vib}(1-x)\right) \tag{5.6}$$

where $S^{Cu}_{vib}(x)$ and $S^{Au}_{vib}(1-x)$ are unknown functions of the concentration variable x. C is the normalization constant for the neutron-weighted DOS:

$$\begin{aligned} C &= \left(\int_0^\infty [3.21g_{Cu}(E) + g_{Au}(E)]\,dE\right)^{-1} && (5.7)\\ &= [3.21x + (1-x)]^{-1} && (5.8)\end{aligned}$$

The notation $S^{d}_{vib}(x)$ refers to the vibrational entropy of species d *within an alloy* where species d is at concentration x. By definition $S^{Cu_xAu_{(1-x)}}_{vib} = S^{Cu}_{vib}(x) + S^{Au}_{vib}(1-x)$. The neutron-weighted entropy is thus a neutron-weighted sum of the partial entropies, S^{d}_{vib}.

In figure 5.4 we show the neutron-weighted vibrational entropies at 300 K of elemental Cu, Au and six disordered Cu-Au alloys. These values are as calculated from the neutron-weighted phonon DOS of figure 5.3. The values for elemental Cu and Au were taken from previous work [88], and the DOS are reproduced in figure 5.3. The entropies of elemental Cu and Au were measured in substantially the same manner as the Cu-Au alloys: the vibrational entropy was calculated from phonon DOS measured by TOF inelastic neutron scattering from bulk polycrystalline samples. In addition, the vibrational entropy of Cu and Au were verified by comparing with results from single-crystal phonon dispersion measurements [56]. These comparisons are shown in figure 5.5.

Our approach to neutron-deweighting the vibrational entropy consists of inferring the real partial entropies from the neutron-weighted entropies, and from these constructing the true vibrational entropy. In the next section we show a variety of different methods for accomplishing this task.

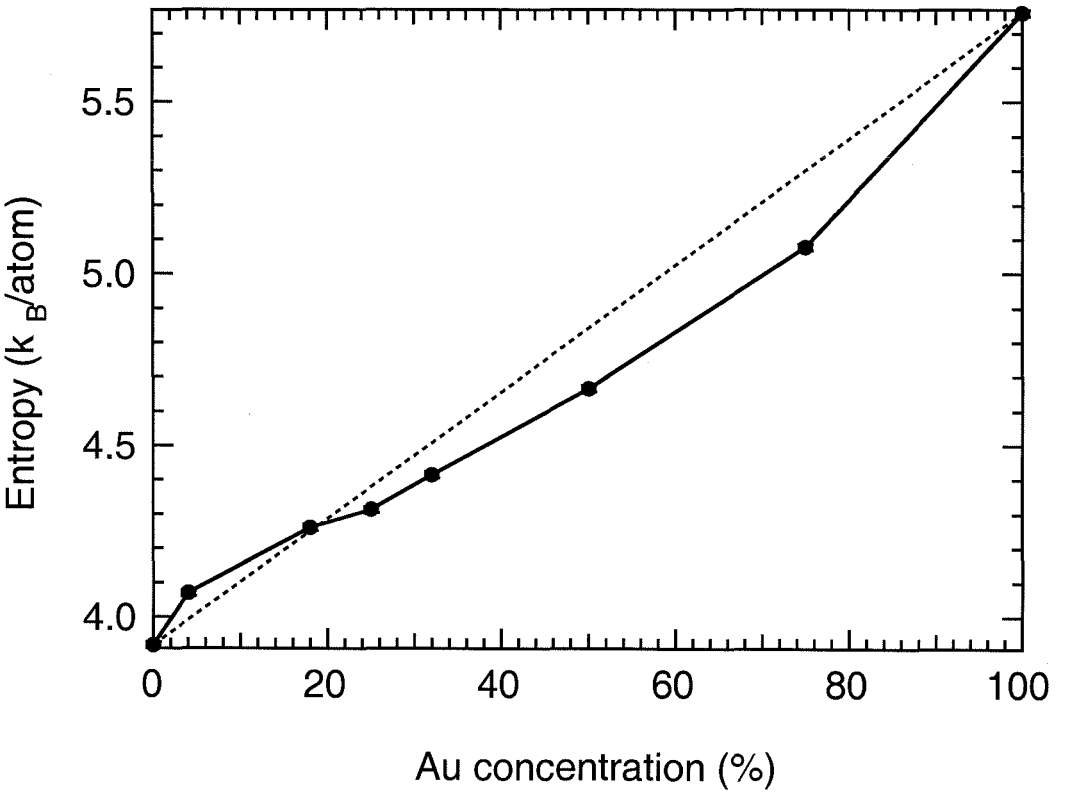

Figure 5.4: Neutron-weighted vibrational entropies of disordered Cu-Au alloys at 300 K. The dashed line is the straight line connecting the vibrational entropies of elemental Au and Cu.

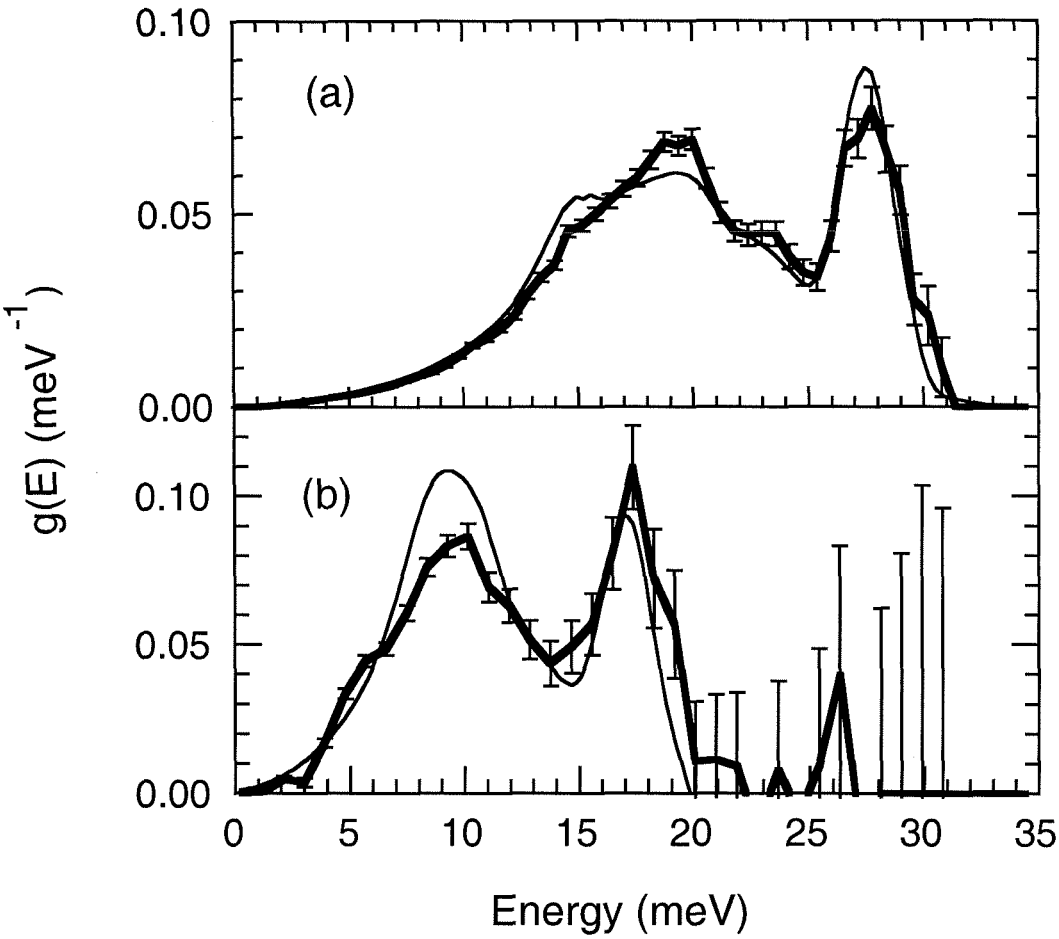

Figure 5.5: (a) Phonon DOS of elemental Cu at 300 K. (b) Phonon DOS of elemental Au at 300 K. The bold lines are TOF results, and the thin lines are taken from triple-axis phonon dispersion measurements [120, 121].

5.3.3 Neutron-Weight Corrections for Disordered Alloys

Our goal is to derive the true vibrational entropies from the neutron-weighted vibrational entropies. We shall proceed from the simplest corrections to the most complicated.

Point Approximation

The simplest chemical model of vibrational entropy assumes the point approximation:

$$S_{vib}^{Cu_x Au_{(1-x)}} = x\, S_{vib}^{Cu} + (1-x)\, S_{vib}^{Au} \tag{5.9}$$

where $0 \leq x \leq 1$ and neither S_{vib}^{Cu} or S_{vib}^{Au} are functions of x. Consolidating equations 5.6 and 5.8 we arrive at

$$S_{vib}^{NW}(x) = k\, \hat{S}_{vib}^{Cu} + (1-k)\hat{S}_{vib}^{Au} \tag{5.10}$$

where

$$k = \frac{x}{x + (1-x)\frac{1}{3.21}} \tag{5.11}$$

and

$$\hat{S}_{vib}^{d} = \frac{S_{vib}^{d}}{\int_0^\infty g_d(E)\, dE} \tag{5.12}$$

Thus, $S_{vib}^{Cu} = x\, \hat{S}_{vib}^{Cu}$ and $S_{vib}^{Au} = (1\text{-}x)\hat{S}_{vib}^{Au}$. We note that equation 5.10 has the form of the point approximation, equation 5.9, where x = k. Thus, we assert that $S_{vib}(k) = S_{vib}^{NW}(x)$. Using this scheme, the S_{vib}^{NW} for $Cu_{50}Au_{50}$ becomes the true value of S_{vib} for $Cu_{76}Au_{24}$. The point approximation correction is shown in figure 5.6.

The point approximation is strictly correct only if the partial entropies (and partial DOS) of Au and Cu stay unchanged as the alloy varies in composition between Cu_xAu_{1-x} and Cu_kAu_{1-k}. For x and k far apart, this approximation is likely to have large errors. We can better make use of the point approximation by choosing alloys where x and k are close in value, as in the following procedure.

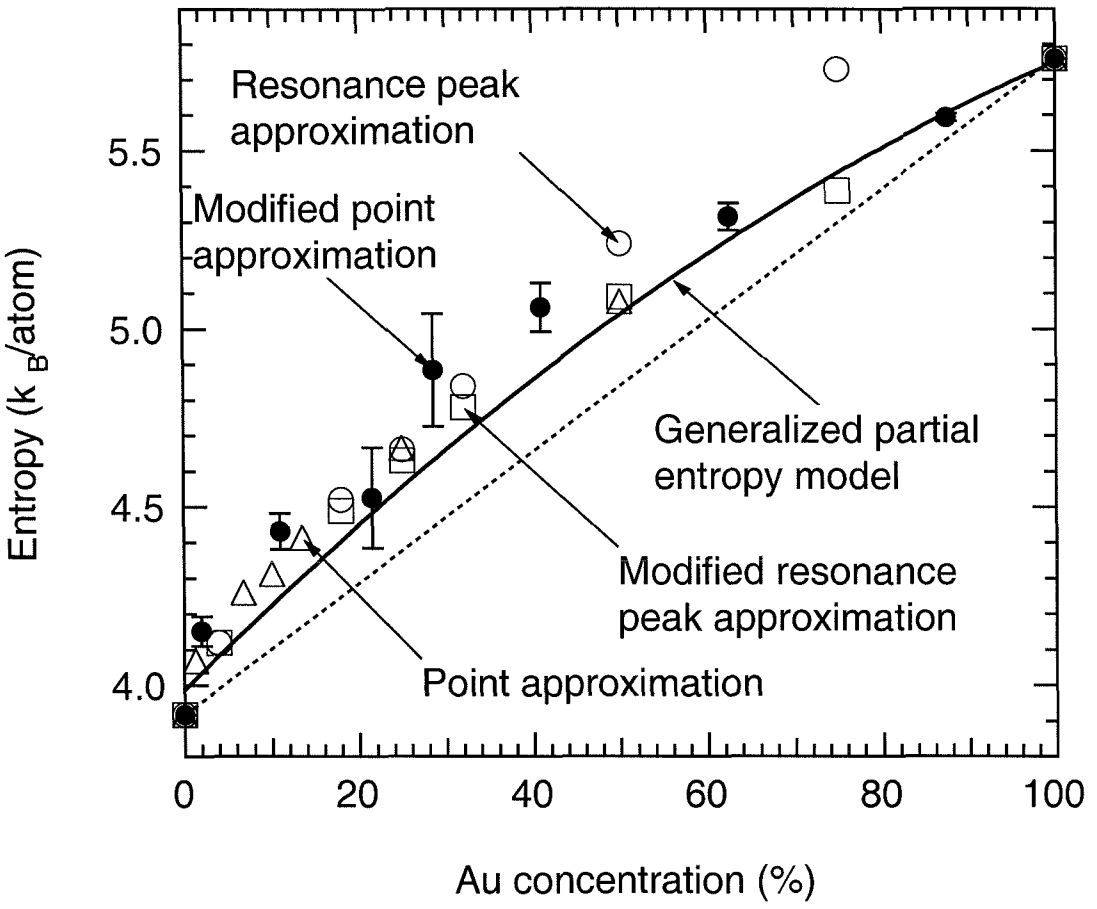

Figure 5.6: Neutron-weight corrected vibrational entropies of disordered Cu-Au alloys at 300 K. The dashed line is the straight line connecting the vibrational entropies of elemental Au and Cu.

Modified Point Approximation

In equation 5.10 the left-hand side is known and the right-hand side is unknown. This is a linear equation where there are two unknowns. Two such equations with the same two unknowns would allow us to solve for the partial entropies, and thus the real vibrational entropy. Each alloy composition provides us with one equation of form equation 5.10. We choose two adjacent alloy compositions, assume the partial entropies are the same for each composition, then solve. By choosing compositions that are close to each other, we can improve upon our previous point approximation. The partial entropies, $\hat{S}^{Cu}_{vib}$ and $\hat{S}^{Au}_{vib}$, calculated in this fashion are an average of the two somewhat different partial entropies at each adjacent alloy composition. Thus, we

assume the partial entropies derived in this fashion are most accurate not at the two compositions, but at the average composition. Using the neutron-weighted entropies of the $Cu_{68}Au_{32}$ and $Cu_{50}Au_{50}$ alloys, we calculate the average partial entropies $\hat{S}^{Cu}_{vib}$ = 4.12 k_B and $\hat{S}^{Au}_{vib}$ = 6.41 k_B. From these values we calculate the vibrational entropy of the alloy at composition $Cu_{59}Au_{41}$. The partial entropies of Au and Cu, calculated from pairs of adjacent compositions, are shown on figure 5.7.

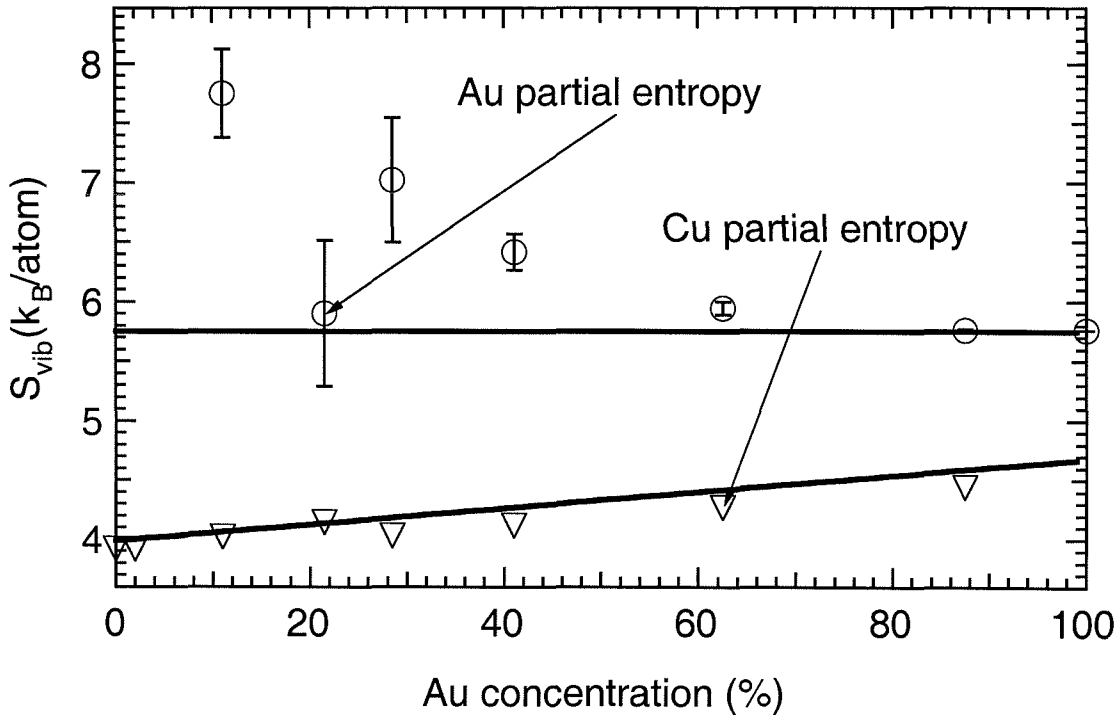

Figure 5.7: Partial vibrational entropies of Cu and Au in Cu-Au alloys. Open symbols are obtained in the modified point approximation. Bold lines are taken from a three-parameter generalized partial entropy model.

The total vibrational entropies, calculated from the partial entropies of figure 5.7, are shown on figure 5.6. We note that these agree well with the values computed from the point approximation. Although this method is in principle better than the point approximation, it suffers from large uncertainties in the computed partial entropies and total entropies. The errors become larger as the level of approximation becomes better. The closer the two alloys are in composition, the more accurate our assumption of equal partial entropies. Unfortunately, as the compositions become closer in value, it is more difficult to resolve accurately the difference in neutron-

weighed entropies, given the uncertainties in the values of these entropies. The large error bars on the total entropy values at Cu concentrations of 78.5% and 71.5%, shown on figure 5.6, result from the small differences between the neutron-weighted entropies at alloy compositions $Cu_{82}Au_{18}$, $Cu_{75}Au_{25}$ and $Cu_{68}Au_{32}$. Unfortunately, with this method, any improvement in the approximation is negated by the magnified uncertainty in our final result. Nevertheless, it appears that the Au partial vibrational entropy per Au atom is largest at low Au concentrations.

Au Resonance Mode

The modified point approximation method, although lacking good convergence, has the ability to measure the partial entropies of each independent atomic species. It motivated the following neutron-weight correction. Each alloy composition gives us one equation of form equation 5.10. If we knew $\hat{S}_{vib}^{Au}$ we could solve for $\hat{S}_{vib}^{Cu}$ and then the vibrational entropy, using the relationship

$$S_{vib}^{Cu_x Au_{(1-x)}} = x\,\hat{S}_{vib}^{Cu} + (1-x)\,\hat{S}_{vib}^{Au} \tag{5.13}$$

We need to make a suitable guess for $\hat{S}_{vib}^{Au}$. To this end we shall examine the neutron-weighted DOS. An examination of figure 5.3 reveals certain regularities in the evolution of the neutron-weighted DOS as a function of Au concentration. For Au concentrations between 0 and 50%, we note that the peak at 9 meV grows proportionally with increasing Au concentration. Related phenomena have been observed in phonon dispersion measurements of Cu-Au [122] and Cr-W [123, 124] dilute alloys. The presence of a low-energy peak in Cu-Au alloys is well explained by the mass-defect theory of lattice dynamics [125], which we summarize here. The addition of a heavy atom to a matrix of light atoms results in a resonance mode at low energy associated with damped vibrations of the heavy atom. In the low solubility limit, the partial DOS of the heavy atom is a modestly sharp peak at the resonance energy. As the concentration of the heavy atom increases in the alloy, the partial DOS of the heavy atom broadens and develops more features. We make the assumption that the partial

DOS of Au has this form, where the resonance energy is 9 meV. We use the following relationships

$$g_{NW}(E) = k\,\hat{g}_{Cu}(E) + (1-k)\,\hat{g}_{Au}(E) \tag{5.14}$$

$$g_{Cu_xAu_{(1-x)}}(E) = x\,\hat{g}_{Cu}(E) + (1-x)\,\hat{g}_{Au}(E) \tag{5.15}$$

$$\hat{g}_d(E) = \frac{g_d(E)}{\int_0^\infty g_d(E)\,dE} \tag{5.16}$$

and allow $\hat{g}_{Au}(E)$ to be a Gaussian in energy E, of unknown width and centered at E=9 meV. We estimate the width of $\hat{g}_{Au}(E)$ from calculations by Elliott and Taylor [126]. Elliott and Taylor calculated the phonon DOS of 3 and 10% Cu-Au alloys using an analytical Green-function technique. Their results are shown in figure 5.8.

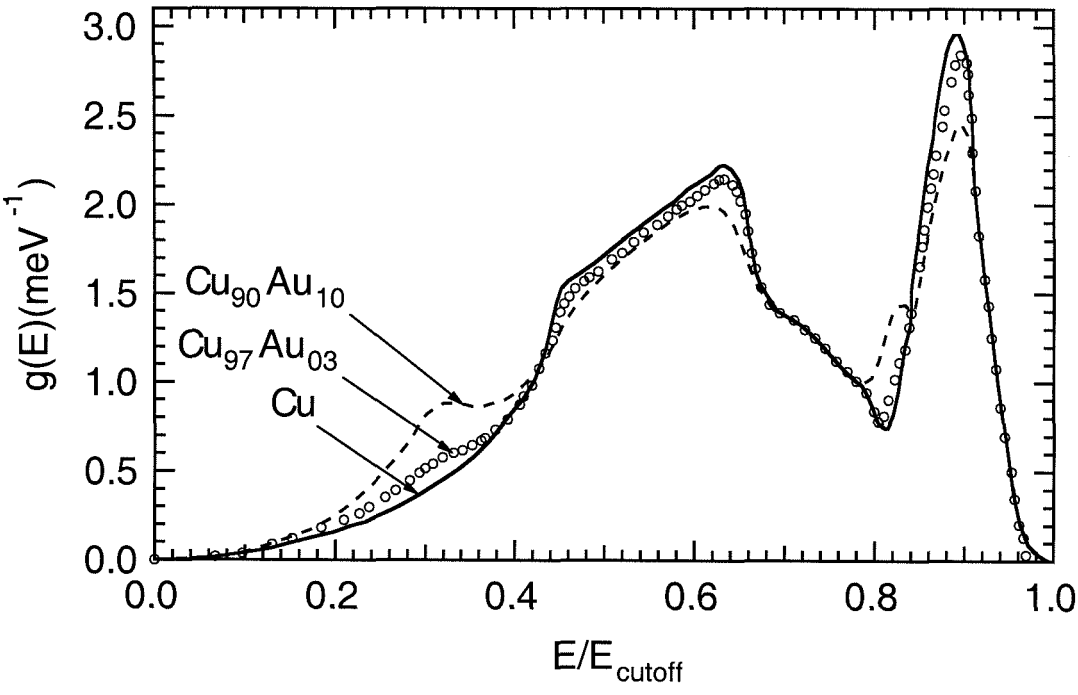

Figure 5.8: Phonon DOS of 3 and 10% Cu-Au alloys as calculated by Elliott and Taylor [126].

The DOS in figure 5.8 show a low-energy resonance peak at 9meV that grows proportionally with Au concentration. This peak is well-modeled as a Gaussian with a standard deviation of 2.5 meV. Using this width as a starting point, we extract the

Cu partial DOS, $\hat{g}_{Cu}(E)$, and total DOS $g_{Cu_xAu_{(1-x)}}(E)$ at each alloy composition. Our results for alloy composition $Cu_{96}Au_{04}$ are shown in figure 5.9.

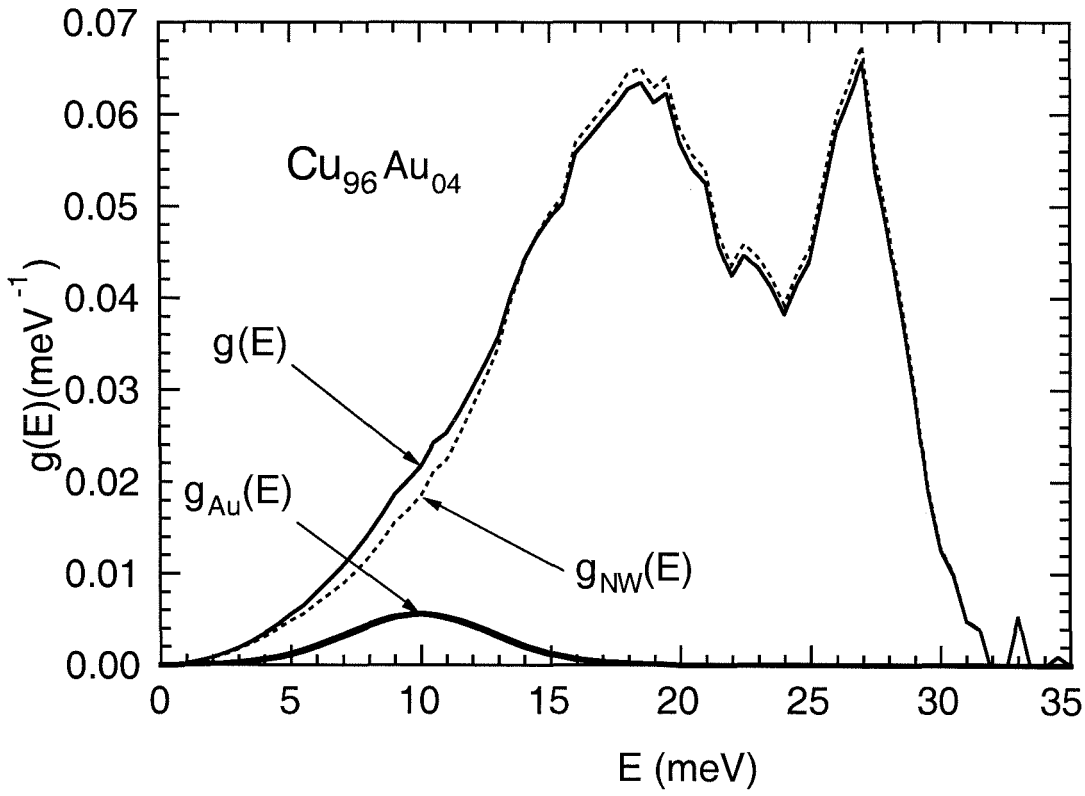

Figure 5.9: The neutron-weighted DOS, Au partial DOS and corrected DOS of $Cu_{96}Au_{04}$ alloy within the resonance peak approximation.

Although not shown in figure 5.9, the Cu partial DOS is nearly identical to the neutron-weighted DOS, $g_{NW}(E)$. Using the corrected total DOS at each alloy composition we can calculate the vibrational entropy. These values are shown in figure 5.6, and are in excellent agreement with the values from the point approximation and the modified point approximation at low Au concentrations. Our results do not depend sensitively on the width of the Gaussian that approximates the Au partial DOS. Varying the Gaussian width by a factor of two led to variations in the entropy smaller than the size of the open circles on figure 5.6.

Au Modified Resonance Mode

The resonance-peak approximation for the Au partial DOS is a poor one for alloys with high Au concentrations. This is apparent by looking at the DOS of elemental Au in figure 5.3, which bears little resemblance to a gaussian in energy centered at 9 meV. We can improve upon our scheme by assuming the Au partial DOS resembles the Gaussian resonance peak G(E) at low Au concentrations, the elemental Au DOS at high Au concentrations, and a weighted sum of the two at intermediate Au concentrations. Thus,

$$\hat{g}_{Au}^{Cu_xAu_{(1-x)}}(E) = x\,G(E) + (1-x)\,g_{vib}^{Au\ element}(E) \tag{5.17}$$

where $\hat{g}_{Au}^{Cu_xAu_{(1-x)}}(E)$ is the partial DOS of Au within an alloy of Cu concentration x. The resulting values for the vibrational entropy using this improved approximation for the Au partial DOS are shown in figure 5.6. They are very close to the resonance-peak results, with large differences at the high Au concentration alloys. Where there are differences, we expect the approximation utilizing equation 5.17 to be the more reliable.

5.3.4 Vibrational Entropy of Ordering of $L1_2$ Cu_3Au

The phonon DOS of ordered Cu_3Au and disordered Cu_3Au are shown in figure 5.10. The DOS of ordered Cu_3Au was taken from the previous work [88]. The disordered Cu_3Au DOS was derived by performing a neutron-weight correction on the neutron-weighted DOS of figure 5.3. For the ordered alloy, the phonon DOS is expected to be highly reliable due to the precision with which the neutron-weight correction is known. This neutron-weight correction is calculated directly from the Born-von Kármán lattice dynamics extracted from the measured phonon dispersions for ordered Cu_3Au. For the case of disordered Cu_3Au, no such Born-von Kármán lattice dynamics model is available. For lack of a better choice, the neutron-weight correction chosen for the disordered phase was the same used to correct the neutron-weighted DOS of the ordered phase. Although the neutron-weight corrections of the ordered and

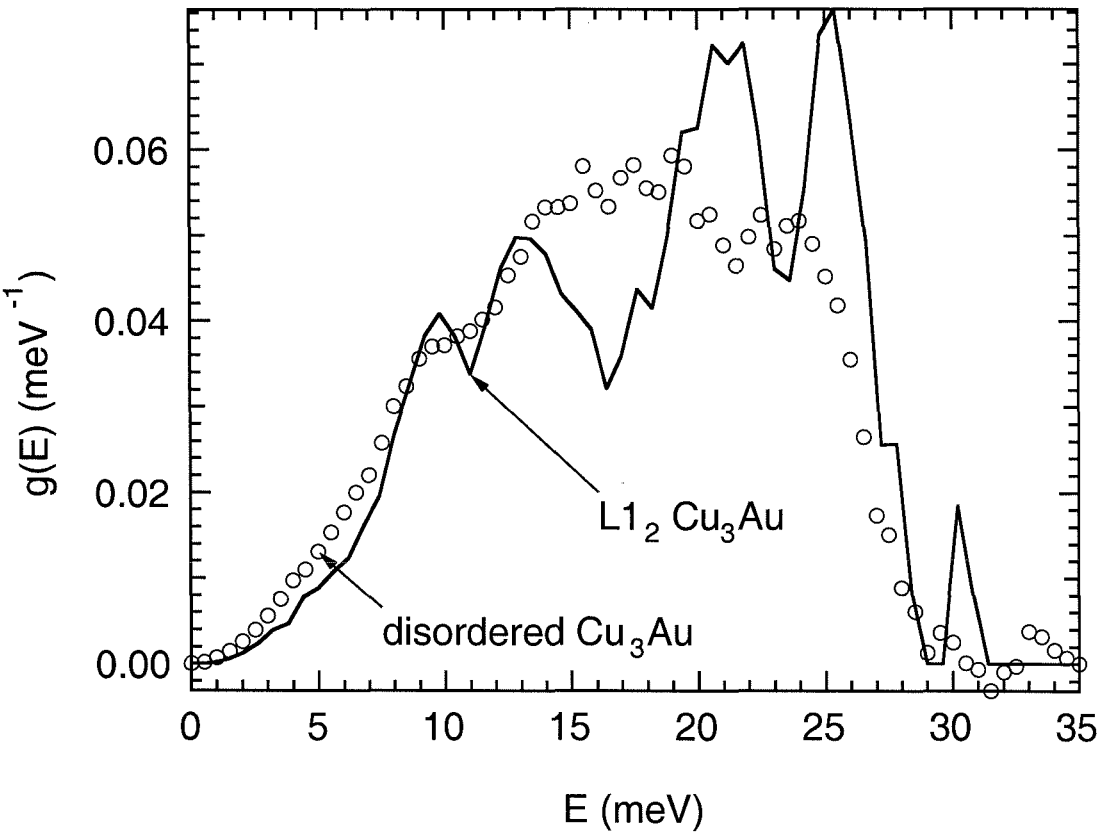

Figure 5.10: Phonon DOS of ordered and disordered Cu_3Au.

disordered phases are most likely different in detail, the use of the same correction preserves differences observed in the neutron-weighted DOS. The ΔS_{vib}^{ord} value derived from the phonon DOS shown in figure 5.10 is 0.12 k_B/atom. Our confidence in this value is low, due to the uncertainty associated with the neutron-weight correction of the DOS of the disordered phase. Better values for the vibrational entropy of ordering can be attained by calculating the neutron-weight corrected vibrational entropy of the disordered phase directly, using either the modified point approximation, modified resonance peak method or the generalized partial entropy method. This approach is implemented in section 5.4.4.

5.4 Discussion

5.4.1 Phonon DOS

The neutron-weighted phonon DOS of $Cu_xAu_{(1-x)}$ changes continuously with decreasing Cu concentration. The primary effects are twofold. Firstly, the DOS softens monotonically with increasing Au concentration. This effect can be seen most clearly in the high energy cutoff of the DOS: 31 meV for Cu and 20 meV for Au. The effect is not quite linear in Au concentration, as can be observed in figure 5.3. The DOS of $Cu_{50}Au_{50}$ terminates at 27 meV, not at 25.5 meV. Secondly, the peak at 9 meV grows rapidly with increasing Au concentration. This peak is almost certainly a resonance mode due to Au vibrations. First predicted by Rayleigh [127] and Lifshitz [128, 129, 130], the resonance mode is the low energy vibration resulting from a heavy atom substituted into a matrix of much lighter atoms. The phonons contributing to a resonance mode are expected to be composed entirely of heavy atom motions, with contributions from light atoms near the heavy impurity. Strictly speaking, resonance modes are a phenomenon associated with dilute alloys only. For the case of $Cu_xAu_{(1-x)}$, we see the persistence of a strong resonance mode up to Au concentrations of 50%. The resonance mode in Cu-Au is strongly de-emphasized in the neutron-weighted DOS because of the small scattering cross-section and large mass of the Au atom.

It is difficult to ascertain the changes of the phonon DOS at Au concentrations between 50 and 100% due to our single measurement in this region. In principle, there should be a local mode associated with the vibrations of the minority Cu atoms in a heavy Au atom matrix. Unlike the case for a Au resonance mode, these Cu vibrations should occur at high energy, perhaps even well separated from the rest of the phonon DOS. It is possible the extended tail and shoulder observed in the $Cu_{25}Au_{75}$ DOS between 23 and 25 meV are due to Cu local modes.

5.4.2 Generalized Partial Entropy Modeling

The modified point approximation was a specific case of a more generalized neutron-weight correction method. In the modified point approximation, the partial entropies of Cu and Au were modeled with two parameters. Two linear equations were then inverted to solve for the unknown parameters. In principle, the partial entropies of Cu and Au can be modeled with an arbitrary number of parameters, and any number of equations of the form 5.10 can be inverted to solve for the parameters and partial entropies. Here we are limited by the total number of different compositions we measured: eight. For a perfectly-determined system of equations, this allows up to eight parameters to model the partial entropies of Cu and Au. We choose to use four parameters: two parameters to parameterize $\hat{S}^{Cu}_{vib}$ and two for $\hat{S}^{Au}_{vib}$. The form of the model is a first-order polynomial in concentration variable x:

$$\hat{S}^{d}_{vib} = c^{d}_{0} + c^{d}_{1}\, x \tag{5.18}$$

where the parameters are the coefficients c^{d}_{0} and c^{d}_{1}. For each alloy composition $Cu_xAu_{(1-x)}$ we have one equation in four unknowns:

$$S^{NW}_{vib}(x) = k(x)\,\hat{S}^{Cu}_{vib} + (1 - k(x))\,\hat{S}^{Au}_{vib} \tag{5.19}$$

where $\hat{S}^{Cu}_{vib}$ and $\hat{S}^{Au}_{vib}$ are parameterized as shown in equation 5.18. We label each alloy composition x with an integer value i, where i=$\{1,\ldots,8\}$ and

$$\mathbf{x} = \{x_1, \ldots, x_i, \ldots, x_8\} = \{1.0, 0.96, 0.82, \ldots, 0.25, 0.0\}. \tag{5.20}$$

This system of equations is overdetermined, with four unknowns and eight equations. Generally speaking, we cannot find values for the unknowns which simultaneously solve all eight equations. However, we can find values of the unknown parameters that best solve all equations simultaneously, in a least-squares sense.

In matrix notation, we denote the system of equations as

$$[k\Phi]\,\vec{c} = \vec{S_{vib}^{NW}} \tag{5.21}$$

where

$$\vec{c} = \begin{pmatrix} c_0^{Cu} \\ c_1^{Cu} \\ c_0^{Au} \\ c_1^{Au} \end{pmatrix} \tag{5.22}$$

$$\vec{S_{vib}^{NW}} = \begin{pmatrix} S_{vib}^{NW}(Cu) \\ S_{vib}^{NW}(Cu_{96}Au_{04}) \\ \vdots \\ S_{vib}^{NW}(Au) \end{pmatrix} \tag{5.23}$$

and

$$[k\Phi]_{i,j} = \begin{cases} k(i)\,x^{(j-1)} & \text{if } j<3 \\ (1-k(i))\,x^{(j-3)} & \text{otherwise} \end{cases} \tag{5.24}$$

where $[k\Phi]_{i,j}$ is the element at row i and column j of matrix $[k\Phi]$. Matrix $[k\Phi]$ is size 8×4. The term k(i) is the value of k, computed from equation 5.11, at alloy composition i. Our definition of the matrix $[k\Phi]$ shown in equation 5.24 implements the linear parameterization of the Cu and Au partial entropies, shown in equation 5.18.

Inverting equation 5.21, we solve for the parameter vector $\vec{c}$. The inversion is done using *singular value decomposition*, which returns the unique choice of $\vec{c}$ if the number of parameters is equal to the number of unknowns or the least-squares choice of $\vec{c}$ for an overdetermined system of equations. The least squares choice of $\vec{c}$ is the $\vec{c}$ that minimizes the quantity $|\,[k\Phi]\vec{c} - \vec{S_{vib}^{NW}}\,|$. For this example, the system is overdetermined so we expect only a least squares choice of $\vec{c}$. We can solve for the partial entropies and total vibrational entropy trivially once we know the parameter-vector $\vec{c}$. In matrix notation, solving for the correct vibrational entropy is done by evaluating

$$[x\Phi]\,\vec{c} = \vec{S}_{vib} \tag{5.25}$$

where

$$[x\Phi]_{i,j} = \begin{cases} x(i)\,x^{(j-1)} & \text{if } j<3 \\ (1-x(i))\,x^{(j-3)} & \text{otherwise} \end{cases} \tag{5.26}$$

and the i^{th} element of $\vec{S}_{vib}$ corresponds to the neutron-weight corrected vibrational entropy at the i^{th} alloy composition. The term x(i) corresponds to the concentration of Cu of the i^{th} alloy. Using the parameterization of $\hat{S}^{Cu}_{vib}$ and $\hat{S}^{Au}_{vib}$ shown in equation 5.18 and the neutron-weighted entropies from all eight alloy compositions, we solve for $\vec{c} = \{c_0^{Cu}, c_1^{Cu}, c_0^{Au}, c_1^{Au}\}$.

Unfortunately, this procedure is flawed. Allowing both $\hat{S}^{Cu}_{vib}$ and $\hat{S}^{Au}_{vib}$ to be parameterized with the same functional form introduces a fatal linear dependence into matrix $[k\Phi]$. For arbitrary composition x, a row of $[k\Phi]$ has the following elements:

$$\{k, kx, (1-k), (1-k)x\} \tag{5.27}$$

These four elements are linearly dependent functions; there exists a choice of

$$\vec{c}_{null} = \{c_0^{Cu}, c_1^{Cu}, c_0^{Au}, c_1^{Au}\} \neq 0 \tag{5.28}$$

such that

$$c_0^{Cu}\,k + c_1^{Cu}\,kx + c_0^{Au}\,(1-k) + c_1^{Au}\,(1-k)x = 0 \tag{5.29}$$

Using k defined in equation 5.11, $\vec{c}_{null} = \lambda\{-0.215, 0.215, .0.69, 0.69\}$, where λ is an arbitrary constant. This can be easily verified by substitution. For any choice of λ, the following holds true:

$$[k\Phi]\vec{c}_{null} = 0 \tag{5.30}$$

The above property leads us to say that $\vec{c}_{null}$ belongs to the *nullity* of matrix $[k\Phi]$. Thus, it is impossible to find a unique choice of $\vec{c}$ that minimizes the quantity $|[k\Phi]\vec{c} - \vec{S}_{vib}^{NW}|$. An arbitrary vector $\vec{c}_{null}$ can be added to $\vec{c}$ without affecting our minimization of the quantity $|[k\Phi]\vec{c} - \vec{S}_{vib}^{NW}|$. It is sadly true that our system of equations can be both overdetermined and linearly dependent at the same time. Speaking qualitatively, it is impossible to distinguish the separate contributions to S_{vib}^{NW} from $\hat{S}_{vib}^{Cu}$ and $\hat{S}_{vib}^{Au}$ when the partial entropies are linearly dependent as shown in equation 5.29. We have the case where the behavior of a set of S_{vib}^{NW} can be equally well described with different linear models for $\hat{S}_{vib}^{Cu}$ and $\hat{S}_{vib}^{Au}$.

The linear dependence can be avoided by modifying our parameterization of $\hat{S}_{vib}^{Au}$. We set $c_1^{Au} = 0$ and solve for the least squares choice of $\vec{c} = \{c_0^{Cu}, c_1^{Cu}, c_0^{Au}\}$. This method improves upon the modified point approximation in three ways: first, we allow for a linear dependence on composition of the partial entropy of Cu, $\hat{S}_{vib}^{Cu}$. Second, we model the partial entropies of Cu and Au by fitting to all eight alloy compositions simultaneously. Lastly, the generalized method does not suffer the poor convergence of the modified point approximation: the uncertainties on $\vec{c}$ do not increase as the alloy compositions become more similar. The resulting partial entropies are shown in figure 5.7. The corrected vibrational entropy is shown in figure 5.6. We note excellent agreement between these results and the previous neutron-weight corrections to the entropy.

The success of the generalized partial entropy model depends on the parameterization of the partial entropies $\hat{S}_{vib}^{d}$. The parameterization of $\hat{S}_{vib}^{d}$ is constrained to be linear with respect to the parameters c_j^d, where $j = \{1,\ldots,N\}$. This constraint mandates the general functional form of $\hat{S}_{vib}^{d}$:

$$\hat{S}_{vib}^{d}(x) = \sum_{j=1}^{N} c_j^d \, f_j^d(x) \tag{5.31}$$

where $f_j^d(x)$ are functions of concentration variable x. We refer to f_j^d as the j^{th} *basis function* of the partial vibrational entropy of atomic species d. Additionally, the $f_j^d(x)$ must be chosen so to avoid linear dependence of $[k\Phi]$, as was seen in the case of Cu-Au

above. For the case of a binary alloy, where d={1,2}, we can state this constraint in general: The equation

$$\sum_{j=1}^{N} c_j^1(k) f_j^1(x) + c_j^2(1-k) f_j^2(x) = 0 \tag{5.32}$$

must have only one solution for arbitrary x: $c_j^d = 0$ for all j and d. Typically we want to parameterize all atomic species with the same model, so $f_j^i = f_j^k$ for all j and $i \neq k$. Using this simplification, we restate equation 5.32 in matrix-vector notation:

$$\vec{f}^T \cdot \vec{c}_2 + k\vec{f}^T \cdot \Delta\vec{c} = 0 \tag{5.33}$$

where $\vec{f}^T$ is the vector transpose of shared basis functions $f_j(x)$, $\vec{c}_d$ is the parameter vector for atomic species d and $\Delta\vec{c} = \vec{c}_1 - \vec{c}_2$. We desire equation 5.33 to have the unique solution $\vec{c}_1 = \vec{c}_2 = 0$ for arbitrary x. A set of basis functions $f_j(x)$ that both satisfy this constraint and model $\hat{S}_{vib}^d(x)$ is unknown.

5.4.3 Local Cluster Approximation

The local cluster approximation (LCA) can be used to calculate thermodynamic properties of chemically disordered materials. This theory is explained in some detail in Appendix B. The LCA can be used to parametrize the partial entropies of Cu and Au within the generalized partial entropy model. This parameterization is a poor one, since the LCA basis functions become linearly dependent beyond the point cluster. Using the LCA to interpret experimental results is motivated by the use of the LCA within the theoretical community to describe the properties of disordered crystals.

Recent theoretical work by Ozoliņš, Wolverton and Zunger [10] has provided a temperature dependent LCA model for the vibrational entropy of formation of disordered Cu-Au alloys. In this work, Ozoliņš and coauthors obtained the phonon DOS and vibrational entropy for a series of ordered Cu-Au alloys using *ab-initio* electronic-structure calculations within the local density approximation (LDA). Using results from six ordered Cu-Au alloys, Ozoliņš and coauthors found the values of cluster-

coefficients S_i that best reproduced their results. The clusters used were the empty cluster S_0, the point cluster S_1, the nearest-neighbour (NN) pair S_2, the second NN pair S_3 and the NN triangle S_4. The values for the cluster coefficients at 300 K, given in Table 5.1, were kindly provided by V. Ozoliņš [131].

	S_0	S_1	S_2	S_3	S_4
Cluster Coeffecients	0.234	0.0185	-0.108	-0.122	-0.0185

Table 5.1: LCA cluster coeffecients at 300 K from Ozoliņš, Wolverton and Zunger. Units are in k_B/atom. The cluster expansion is for the vibrational entropy of formation of disordered Cu-Au alloys [131].

Using the values given in Table 5.1 and equation B.1, we can calculate the vibrational entropy of formation of binary Cu-Au at 300 K, as a function of Cu concentration. For the case of a perfectly disordered binary system, equation B.1 simplifies to

$$S_{vib}^{formation} = S_0 + S_1(1-2c) + S_2(1-2c)^2 + S_3(1-2c)^2 + S_4(1-2c)^3 \qquad (5.34)$$

where c is the fractional concentration of Au in the alloy. Note that we include only five terms corresponding to the five clusters in our LCA sum. The terms corresponding to the NN pair and second NN pair, S_2 and S_3, have the same functional dependence on c. This occurs because in a fully disordered alloy there is no short-range chemical order, and hence no difference between first and second nearest-neighbors in the frequency of like and unlike atomic pairs. We evaluate equation 5.34 and plot the results in figure 5.11. The agreement is good with both the modified resonance peak approximation and the generalized partial entropy correction. The LCA results are smaller than those of the modified point approximation for Cu rich alloys. This difference is also found between the LCA and modified resonance peak approximation.

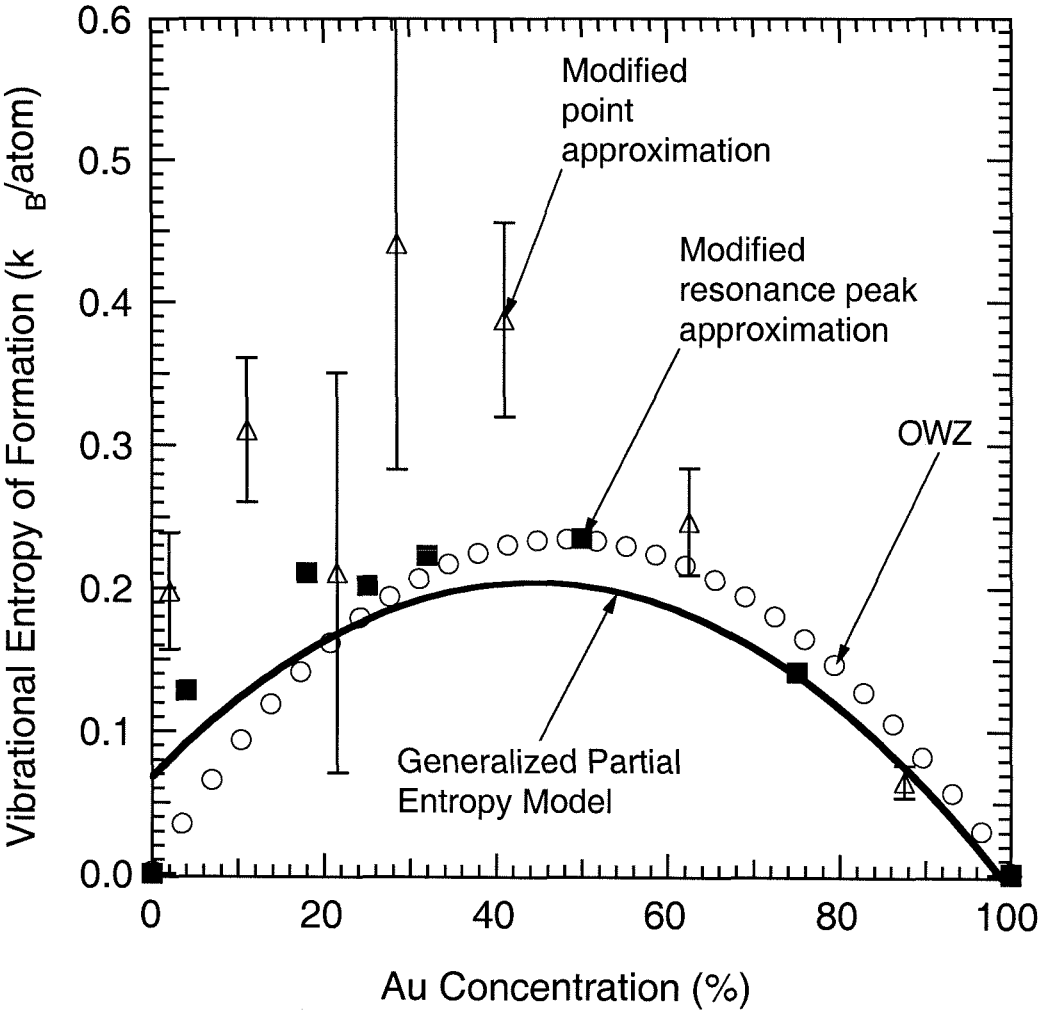

Figure 5.11: Vibrational entropy of formation of disordered Cu-Au alloys at 300 K. The circles marked OWZ are the LCA results by Ozoliņš, Wolverton and Zunger.

5.4.4 Vibrational Entropy of Ordering of Cu_3Au

The phonon DOS of ordered and disordered Cu_3Au differ substantially, as shown in figure 5.10. The DOS of the ordered alloy exhibits large Van-Hove singularities at 9, 13, 20 and 25 meV. The DOS of the disordered alloy has one very broad central feature at 16 meV, and two small peaks at 10 and 24 meV. The high-energy cutoff is the same for both the ordered and disordered DOS.

The vibrational entropy of disordering calculated from the phonon DOS of figure 5.10 is half the size of the value derived from the phonon dispersion measurements of Katano et al.[56] and is in good agreement with the calorimetric estimate. How-

ever, we have low confidence in the vibrational entropy of disordering calculated from the lattice dynamics corrected phonon DOS. In figure 5.12 we compare our phonon DOS of disordered Cu_3Au with that of Katano and coauthors.

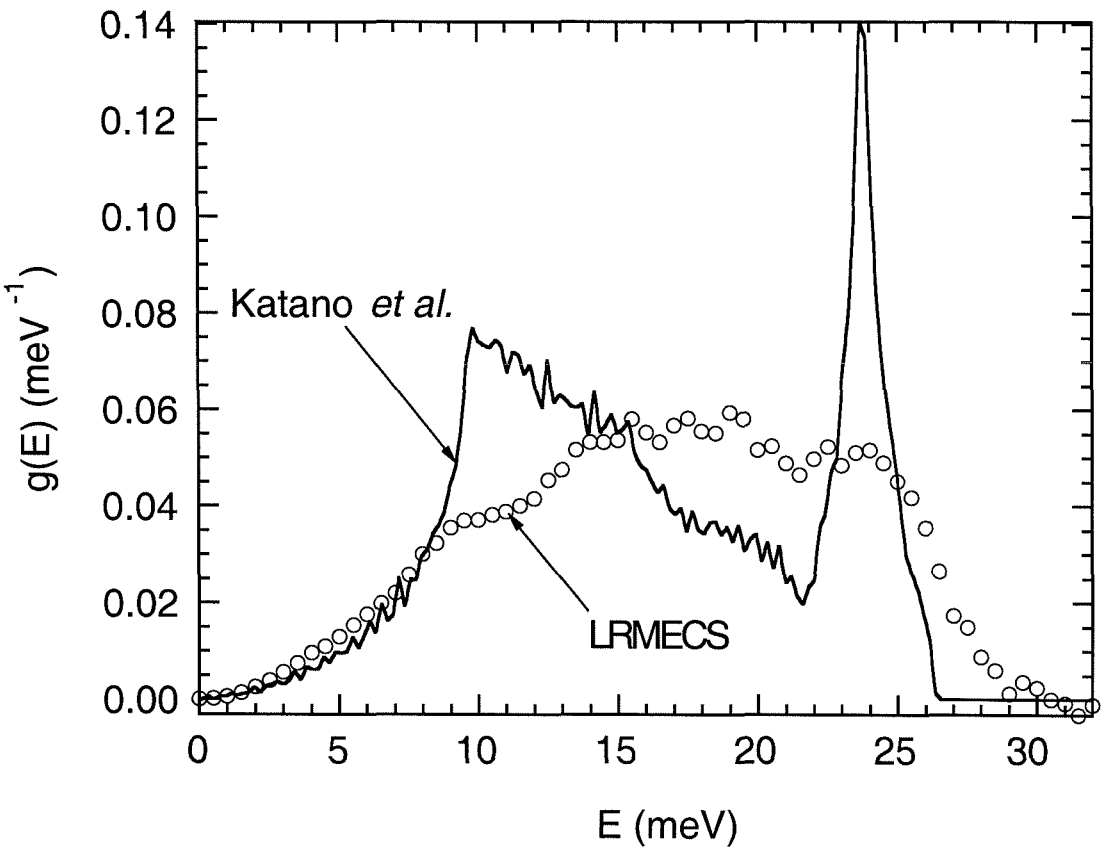

Figure 5.12: Phonon DOS of disordered Cu_3Au derived from phonon dispersions.

The lack of agreement is notable, and is due largely to the inaccuracies introduced by the virtual crystal approximation. The virtual crystal approximation assumes a single atomic species only, where the atomic mass is the average of the real crystal. This assumption allows a phonon DOS to be modeled using a simple fcc unit cell and measured phonon dispersions. Our results are a *direct* measurement of the phonon DOS, with some small uncertainty introduced by the neutron-weight correction.

The vibrational entropy of disordering depends sensitively on the phonon DOS of both the ordered and disordered phases of Cu_3Au. The DOS of ordered Cu_3Au is known more reliably than the DOS of the disordered phase, due to the more reliable neutron-weight correction of the ordered phase. Our value of ΔS_{vib}^{ord} derived

from the phonon DOS has some uncertainty associated with it due to the neutron-weight correction of the disordered phase. Using the correction methods discussed in section 5.3.3, we show the values of ΔS_{vib}^{ord} in Table 5.2.

Neutron-weight Correction	$\Delta S_{vib}^{ord}(k_B/atom)$
Point Approximation	0.33
Modified Point Approximation	0.35±0.2
Resonance Peak	0.25
Modified Resonance Peak	0.25
Generalized Partial Entropy Model	0.24
$L1_2$ Born-von Kármán Lattice Dynamics	0.12
Ozoliņš, Wolverton and Zunger	0.06

Table 5.2: ΔS_{vib}^{ord} of Cu_3Au as a function of neutron-weight correction of disordered phase. Uncertainties due to neutron-counting statistics are $\pm 0.02\,k_B$/atom, unless otherwise stated.

The resonance peak, modified resonance peak and generalized partial entropy corrections closely agree with each other and are twice as large as the value of ΔS_{vib}^{ord} derived from the lattice dynamics corrected phonon DOS. The phonon DOS results are of low confidence due to the use of the ordered phase lattice dynamics to correct the neutron-weighted DOS of the disordered phase. The point approximation yields the largest result, but this approximation is the least sophisticated so we disregard it in favor of the other corrections. The modified point approximation agrees within error bars with the remaining corrections. Of these corrections, the modified point approximation and generalized partial entropy model are the most accurate in principle, but the modified point approximation is more difficult in practice.

5.5 Conclusions

The neutron-weighted phonon DOS of six disordered Cu-Au alloys have been measured at 300 K. We observe an Au resonance mode at 9 meV in Cu rich alloys. The vibrational entropy of the disordered alloy as a function of composition has been successfully extracted from the neutron-weighted DOS, and is in general agreement with LCA results from Ozoliņš, Wolverton and Zunger. The partial vibrational entropies

of Cu and Au are smoothly varying as a function of composition. This allows for a variety of neutron-weight corrections to the vibrational entropy using simple models for the partial vibrational entropies of Cu and Au. The failure of the generalized partial entropy model shows us that it is impossible to uniquely extract linear models of the Au and Cu partial vibrational entropies, as a function of alloy composition, from any given set of neutron-weighted DOS.

We estimate the vibrational entropy of disordering, ΔS_{vib}^{ord} in Cu_3Au as 0.24 ± 0.02 k_B/atom, at 300 K. The vibrational entropy of disordering at T_c might be different, depending on how the phonon DOS of the two phases change between 300 and 663 K. Our results are four times larger than the calculations of Ozoliņš, Wolverton and Zunger.

Chapter 6 Conclusions

6.1 Science and Methods

In this thesis we explored the importance of vibrational entropy on phase stability in metals and alloys. Each chapter has dealt with a specific alloy or alloy system, and has focused upon the vibrational entropy contribution to the thermodynamics of interest. Nevertheless, we find strong scientific connections that were not expected beforehand. In chapter 3 we found vibrational entropy to be the driving force for the martensitic transformation in NiTi. Lattice dynamics simulations in NiTi and high temperature Zr show that the large vibrational entropy of the low-temperature bcc phase is due to a large number of low energy acoustic phonon. These acoustic phonons shift to higher energy at higher temperatures, which is the opposite behavior expected from the volume expansion alone at high temperature. The temperature dependence of phonon energies in bcc metals is revisited in chapter 4. Measurements of the phonon DOS of V at high temperature show that phonon-phonon scattering at high temperature counteracts the phonon softening expected from thermal expansion.

In chapter 5 we develop a novel methodology for the calculation of vibrational entropy from the neutron-weighted phonon DOS in chemically disordered alloys. The approach relies upon modelling the vibrational entropy contributions of each atomic species as a function of alloy composition. The advantage of dealing with the vibrational entropies directly is that the partial vibrational entropy of each species is a slowly-varying and smooth function of composition. In contrast, the partial phonon DOS of each species is difficult to parameterize simply as a function of composition. One can use the local cluster approximation (LCA), or cluster variation method, to model the partial vibrational entropies. This approach is explored more fully in Appendix B. We conclude that it is impossible to uniquely extract best-fit linear models for the partial vibrational entropies from a set of neutron-weighted phonon DOS.

This limitation and its qualifications inform our understanding of the usefulness of the neutron-weighted DOS and entropy.

Other specific conclusions have been sufficiently explained in each individual chapter, and we shall not revisit them here. Chapters 2, 3, 4 and 5 have focused on the science. Here we wish to examine the experimental methodology.

6.1.1 Method 1

The most straightforward measurement of the phonon DOS is the use of a triple-axis spectrometer at constant Q on an incoherently scattering polycrystalline element. Triple-axis spectrometers work in conjuction with reactor sources. This method allows the direct measurement of the phonon DOS, with no approximations in the data analysis. One can measure the DOS and hence the vibrational entropy limited only by the energy resolution of the spectrometer and the time one allows for good counting statistics. One can extend this method with almost equal accuracy to alloys where each atomic species has equal neutron-weight, such as Co-V alloys. In this case we introduce errors when we neglect the individual Debye-Waller corrections in favor of an average Debye-Waller correction. Our study on V in chapter 4 employed this method. Limitations of this method are the small number of elements and miniscule number of alloys that satisfy the requirements of incoherent scattering and equal neutron-weighting.

6.1.2 Method 2

The second-easiest neutron scattering experiment is the use of a time-of-flight (TOF) spectrometer to measure the phonon DOS of a polycrystalline element. TOF neutron spectrometers need a pulsed source (spallation source) to achieve energy resolution. The broad sampling of scattering at different Q allows the use of samples that have coherent or mixed coherent-incoherent scattering. This method allows the direct measurement of the phonon DOS, with substantial approximations in the data analysis. These approximations are sufficiently accurate to allow differential measurements

of the vibrational entropy and phonon DOS. The data analysis and approximations needed for a TOF measurement are not trivial, and are explained in some detail in Appendix A. The methodology outlined in this appendix, combined with its experimental verification in chapters 3 and 5, is a large part of the scientific contribution of this thesis. The measurement of the phonon DOS of elemental Cu in chapter 5 is a good example of this method. The advantage to this method is that one can use it on any nearly any metal in the periodic table, although one is better off using a triple-axis spectrometer for samples that exhibit pure incoherent scattering.

6.1.3 Method 3

The most difficult neutron scattering experiment is the use of a TOF spectrometer to measure the vibrational entropy of a polycrystalline alloy. This experiment has all the difficulties of Method 2 and adds to them the difficulty of implementing a neutron-weight correction to the neutron-weighted DOS. The neutron-weight correction to the DOS can range from the difficult (the use of Born-von Kármán lattice dynamics in NiTi) to the near-impossible (chemically disordered Cu-Au alloys). Neutron-weight correcting the vibrational entropy is a more feasible task. Despite the difficulty, this method is applicable to almost all alloys. In principle, a high resolution TOF spectrum has sufficient information to extract the lattice dynamics near-uniquely from a polyatomic coherently scattering polycrystalline sample. Limitations on the quality of current spectrometers and the sophistication of our data analysis tools make this goal a distant one.

The three methods listed above all share some common limitations. Some elements (Cd, Rh, Gd, ^{235}U) are prohibitively strong neutron absorbers, and their presence, even in small quantities, will eliminate any neutron signal from the sample. Other elements (Au, Co) have sufficiently unfavorable ratios of neutron scattering to absorption cross-sections that only small samples combined with prohibitively long measurement times will yield good data.

An understanding of these practical limitations is useful for designing productive

experiments. In the next section I propose three broad areas of future scientific study, specifically optimized for one of the experimental methods outlined above. My work in chapters 2, 3, 4 and 5 show why these studies will be interesting.

6.2 Future Work

6.2.1 Temperature Dependence of the Phonon DOS

Measuring the phonon DOS of elements is much easier than for alloys. However, the lattice dynamics, phonon DOS and vibrational entropy of almost all elements has already been measured ... *at room temperature*. In chapter 4 we show how the temperature and volume dependent phonon DOS, combined with measurements of the temperature dependent thermal expansion and bulk modulus, can be used to determine the temperature dependent phonon DOS at fixed volume. A calculation of the temperature and volume dependent electronic DOS or electronic entropy is also required. The temperature dependence (at constant volume) of the phonon DOS must be caused by either electron-phonon scattering or phonon-phonon scattering. If the latter, then the excess phonon entropy associated with the temperature shifts of the DOS is identical with the anharmonic vibrational entropy. The temperature dependence of the phonon DOS of the elements has, in general, not been measured. In addition to our work, Manley and coauthors [132] have recently measured the temperature dependence of the phonon DOS of U up to 1213 K. They used a calculation of the total vibrational power spectrum to show that the softening observed in the DOS of U was harmonic, not anharmonic.

The use of polycrystalline elements greatly reduces the time needed for sample preparation and characterization. Beam time on a TOF instrument at a neutron spallation source will be needed for most samples, as described in Method 2. In addition, a reliable TOF compatible furnace that operates at high temperature will also be needed. The use of elemental samples eliminates the need for a neutron-weight correction in the data analysis, thus removing a major obstacle associated with the

measurement of the phonon DOS using neutron scattering.

6.2.2 Vibrational Entropy of Alloying in the Dilute Limit

The vibrational entropic effect of dilute alloying in metals has long been neglected. Although this area has attracted lattice dynamical interest from the theoretical community (see sections 5.3.3 and 5.4.1), the thermodynamic importance has gone unexplored both theoretically and experimentally. What little experimental evidence exists shows promise. In Table 2.2 we observe that the dilute alloying of Pt in V causes an enormous vibrational effect, while Cr in V does very little. Within the Einstein approximation, one might expect a pure mass effect of placing Pt in V given by

$$\Delta S_{vib}^{alloy} = c\frac{3}{2}k_B \ln(\frac{M_{Pt}}{M_V}) \tag{6.1}$$

where c is the concentration of Pt and M is the atomic mass. For $c = 0.05$ we expect $\Delta S_{vib}^{alloy} = 0.1$ k_B/atom. The value calculated from the phonon DOS is 0.4 k_B/atom. An effect in excess of that predicted by the change in mass between the solute and solvent atoms must be caused by a change in the force constants of the alloys. In turn, a change in the force constants is caused by a change in the bonding, or electronic-structure between the element and the alloy. A reasonable experiment would be to systematically measure the effect of dilute alloying as a function of solute atom. One could look for systematic effects as a function of solute atom radius, mass and electron number.

This experiment is well-suited for inelastic neutron scattering. By working in the dilute alloy limit we avoid the use of a neutron-weight correction. To a good first approximation, the neutron-weighed DOS and the real phonon DOS are identical when the concentration of impurity species is low. What we look for is large changes in the phonon modes of the majority species caused by a small concentration of solute atoms. This sort of effect is readily observed using Methods 1 or 2. Measurements could be confined to room temperature, and the data analysis and sample preparation

are greatly simplified by using dilute alloy samples. A good choice of solvent atom would be an element that had good neutron-scattering characteristics (low absorption, large cross-section) as well as metallurgical ones (readily alloys, high ductility).

6.2.3 Fitting Lattice Dynamics to the Phonon DOS

The vibrational entropy of a solid can be derived solely from knowledge of the phonon density-of-states. The phonon DOS is not a unique description of the vibrational excitations in a solid. Phonons (in a translationally periodic crystal) have two quantum labels: energy and wave-vector. Knowledge of the energy as a function of wave-vector constitutes a complete harmonic description of the phonons in a periodic crystal. Traditional methods of measuring the phonon dispersions are time-consuming and not comprehensive: a high quality, large single crystal and considerable time on a triple-axis neutron spectrometer are both needed. Time constraints mandate that only phonon dispersions along a few high symmetry directions are measured. The phonon-dispersions along other directions are inferred by using a Born-von Kármán model to fit the measured data, then arbitrary lattice dynamics information can be calculated using the model.

Alternatively, one can fit measurements of the neutron-weighted phonon DOS (measured using Methods 1, 2 or 3) to a Born-von Kármán lattice dynamics model. This procedure is used in chapter 3 to arrive at a neutron-weight correction for NiTi. Of course, the difficulty with this scheme is that there exists more than one set of phonon dispersions that give the same phonon DOS. In principle, even a perfect fitting routine will be unable to distinguish uniquely which set of force constants is the correct one for the measured data. This same criticism can be leveled at the more traditional method using measured phonon dispersions. In that case, as in ours, there exists more than one set of force constants that equally well describe the measured data. Recent work on the validity of this approach shows that different sets of converged force constants vary little from each other, and thus one can reasonably hope to extract meaningful lattice dynamics data from neutron-weighted phonon DOS.

The simplest implentation of this approach is the following: choose a set of force constants, calculate the neutron-weighted phonon DOS with the model, then compare the model DOS with the experimental DOS. Adjust the force constants, then repeat until the model DOS and experimental DOS are converged. There are numerous practical considerations that have a large effect on the accuracy of this procedure. First, the calculated force-constants can only be as good as the quality of the experimental DOS. A measured DOS with few sharp features (due to poor energy resolution) and uncertain neutron-weighting can yield only a few trustworthy force-constants. Second, the mechanical fitting routine is capable of fitting the measured DOS to a much higher degree of accuracy than is called for, considering the likely error-bars on the measured DOS. One's fitting program might spend much of its time choosing the correct set of fifth-nearest force constants that improves the quality of fit by a few tenths of a percent ... even though the measured DOS has uncertainties of a few percent! It seems necessary to use as few force constants as can give an adequate fit to the data. For typical TOF spectra my experience shows that one should almost never go beyond the third-nearest-neighbor force constants. One should also repeat the fitting procedure many times with different starting guesses...the different sets of converged force-constants will give some idea of the uncertainties in the force-constants. Of course, one should always double-check one's results using physical intuition. The first-nearest neighbour force constants should be larger than the second, which should be larger than the third. When possible, the force constants should be compared to a related system where the lattice dynamics are known. Finally, the tensorial force constants should not stray too far from central-force behavior for close-packed crystal structures, although invar alloys may be an exception.

The mechanical fitting of inelastic scattering data to a model can be greatly improved upon. First, by fitting the model directly to the raw data one can eliminate the large uncertainties introduced by treating the coherent scattering in the incoherent approximation. This would require, for the case of the Born-von Kármán model, calculating correctly the incoherent and coherent single and multiple-phonon scattering contributions as a function of neutron wave-vector, energy transfer and temperature.

This is no trivial task, and would require large modifications to an existing lattice-dynamics code base, which typically calculate phonon dispersions and phonon DOS. Secondly, one should implement a fitting routine that is sensitive to the estimated neutron counting statistics. The fitting routine should stop once it has found a set of force-constants that fit the raw data to within the error bars on the data. Thirdly, the fitting routine should be robust and fast enough to achieve convergence in a reasonable amount of time. Of the two, writing fast code is more feasible than writing robust code. N-dimensionsal function optimization (minimization) is a notorious difficult task, and even the best codes are very sensitive to the starting guess and give only local minima. With a very fast routine, one could minimize a few hundred times and find the best set of converged force-constants.

Modeling of inelastic neutron-scattering data is still in its infancy. No equivalent of the Rietveld-refinement method, applicable in elastic scattering, exists for inelastic scattering. Our ability to measure vibrational properties of materials is rapidly falling behind our ability to predict vibrational properties using *ab-initio* theory. The potential for growth in this research area is enormous and promises a large experimental reward: the measurement of the phonon DOS, lattice dynamics and vibrational entropy of arbitrary materials.

Appendix A Neutron Scattering Analysis from TOF Instruments

A common task is the measurement of the vibrational entropy through time-of-flight (TOF) inelastic neutron-scattering. In order to calculate the vibrational entropy we extract the phonon density-of-states (DOS) from the inelastic neutron-scattering spectra.

A.1 TOF Spectrometer

The (neutron-weighted) phonon DOS can be derived from TOF inelastic neutron scattering. This appendix explains how to derive the phonon DOS from TOF inelastic neutron-scattering data. In figure A.1 we show a schematic view of a TOF spectrometer.

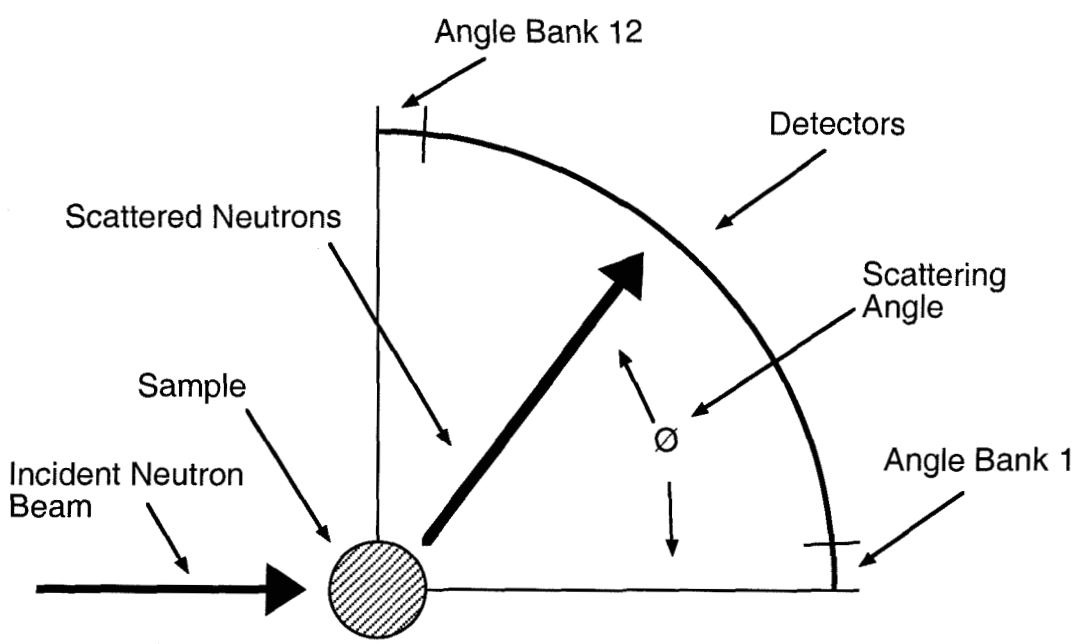

Figure A.1: Schematic diagram of time-of-flight neutron spectrometer.

The incident neutron beam shown in figure A.1 is pulsed and monochromatic.

A small percentage of the incident neutron pulse is scattered from the sample, with the majority of the incident neutrons continuing through the sample unaffected. A near-continuous array of detectors are arranged in a circular arc to one side of the sample. These detectors capture the small number of neutrons that are scattered in their direction. A typical neutron-scattering experiment runs for many thousands of pulses in order to generate sufficient scattered neutrons, and hence good statistics (signal to noise ratio). For a spallation neutron source generating pulses at a few tens of hertz, a single TOF spectra will run for the better part of a day.

For an isotropic sample, or an untextured polycrystalline bulk sample, the scattered neutron intensity only depends upon the scattering angle ϕ. At the LRMECS spectrometer at the Intense Pulsed Neutron Source (IPNS) at Argonne National Laboratory, the detectors cover an angle ϕ from $-10\,^\circ$ to $+120\,^\circ$. The distance from the sample to the detectors combined with the detector timing gives the velocity, and hence the kinetic energy, of the scattered neutron. The location of the detector that records the scattered neutron gives the scattering angle ϕ of the scattered neutron. The neutron-scattering angle ϕ combined with the scattered and incident neutron energies gives the value $\mathbf{k}$, where $\mathbf{k} = \mathbf{k}_i - \mathbf{k}_f$. This vector equality is illustrated in figure A.2.

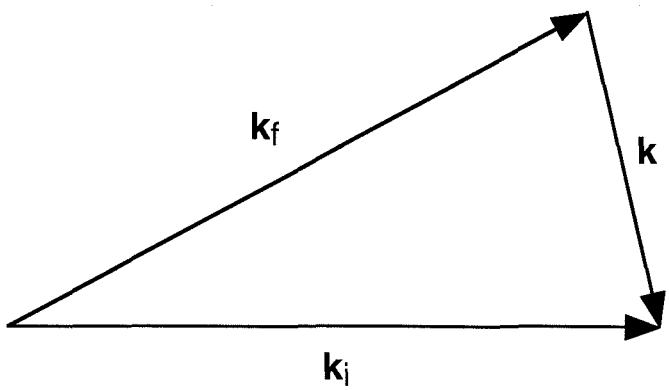

Figure A.2: Relationship between $\mathbf{k}$, $\mathbf{k}_i$ and $\mathbf{k}_f$ neutron wavectors.

The values $\mathbf{k}_i$ and $\mathbf{k}_f$ are the incident and scattered neutron wave-vectors. The wavevector of a neutron propagating in space is given by the neutron kinetic energy E, where

$$E = 2.072\kappa^2 \tag{A.1}$$

E is the neutron energy in meV and κ is the magnitude of $\mathbf{k}$ in inverse angstroms. We use interchangeably Q and κ, where κ= Q. The vector $\mathbf{k}$ points in the same direction as the velocity vector of the neutron.

Each scattered neutron can be labeled by its energy loss and its detection angle. Alternatively, each scattered neutron can be labeled by energy loss and $\mathbf{k}$. In practice, the neutron counts are grouped into bins of finite energy and angle width. This is done to improve the neutron-counting statistics, and for sufficiently narrow bins does not introduce errors into the data analysis. Two detector angle banks are shown in figure A.1, and are labeled banks 1 and 12. At the LRMECS TOF instrument, the default angle binning is done in increments of ten degrees, for a total of 12 angle bins (banks). The relationship between angle-bank, energy gain and κ is shown in figure A.3.

The raw data are labeled by angle-bank and energy-transfer. This information, combined with figure A.3, is sufficient to extract the scattering-vector magnitude κ. The most elegant presentation of the scattering data is of a three-dimensional surface, where neutron-scattering counts are plotted as a function of the in-plane scattering angle and energy-transfer. In figure A.4 we show a constant angle "slice" of this scattering surface for an FeAl sample, taken on the LRMECS spectrometer at IPNS. The quantity S(Q,E) is proportional to the neutron counts per unit time multiplied by the factor k_i/k_f, where k_i is the magnitude of the vector $\mathbf{k}_i$ and k_f is the magnitude of the vector $\mathbf{k}_f$.

It is usually more convenient to preserve the data as a group of two-dimensional data sets, each corresponding to a constant scattering-angle slice of the three-dimensional scattering surface. The scattering-vector magnitude κ can be calculated from the scattering angle and energy transfer using the following equation:

$$\kappa = \left[\{2E_i - x - 2E_i(1 - x/E_i)\cos(\phi)\}/2.072\right]^{\frac{1}{2}} \tag{A.2}$$

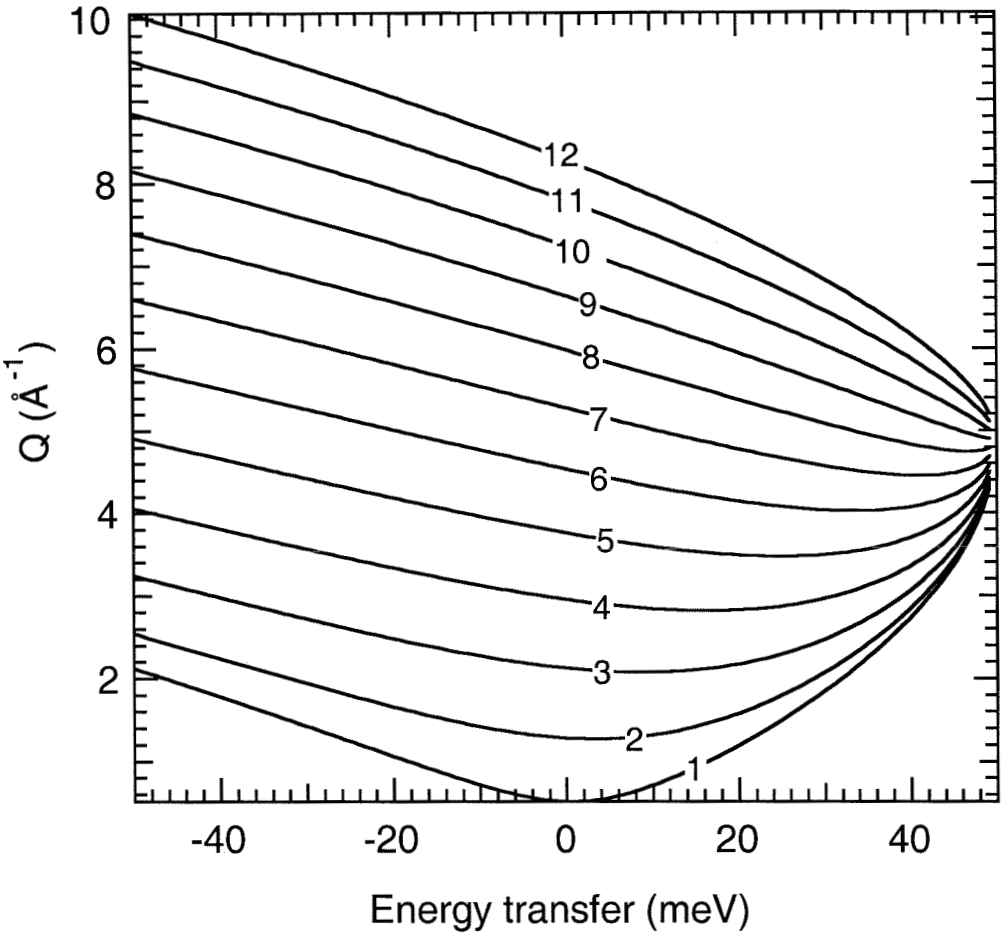

Figure A.3: Q as a function of angle-bank and energy gain for a TOF spectrometer. The curves are labeled by angle-bank. The incident neutron energy is 50 meV.

where E_i is the incident neutron energy in meV, x is the neutron energy-transfer in meV, ϕ is the scattering angle and κ is the scattering-vector magnitude in inverse angstroms.

In figure A.5 we show representative constant scattering-angle slices of the scattering surface of a chemically ordered FeAl specimen with a 2% vacancy concentration. The twelfth and fourth angle-banks correspond to median scattering angles of 115 and 35°, respectively.

The off-scale peak between −4 and +4 meV neutron-energy loss is due to elastic scattering processes. Although phonon scattering does occur in this energy range, the elastic scattering is greater by several orders of magnitude and we effectively lose all information on the phonon scattering in this energy region.

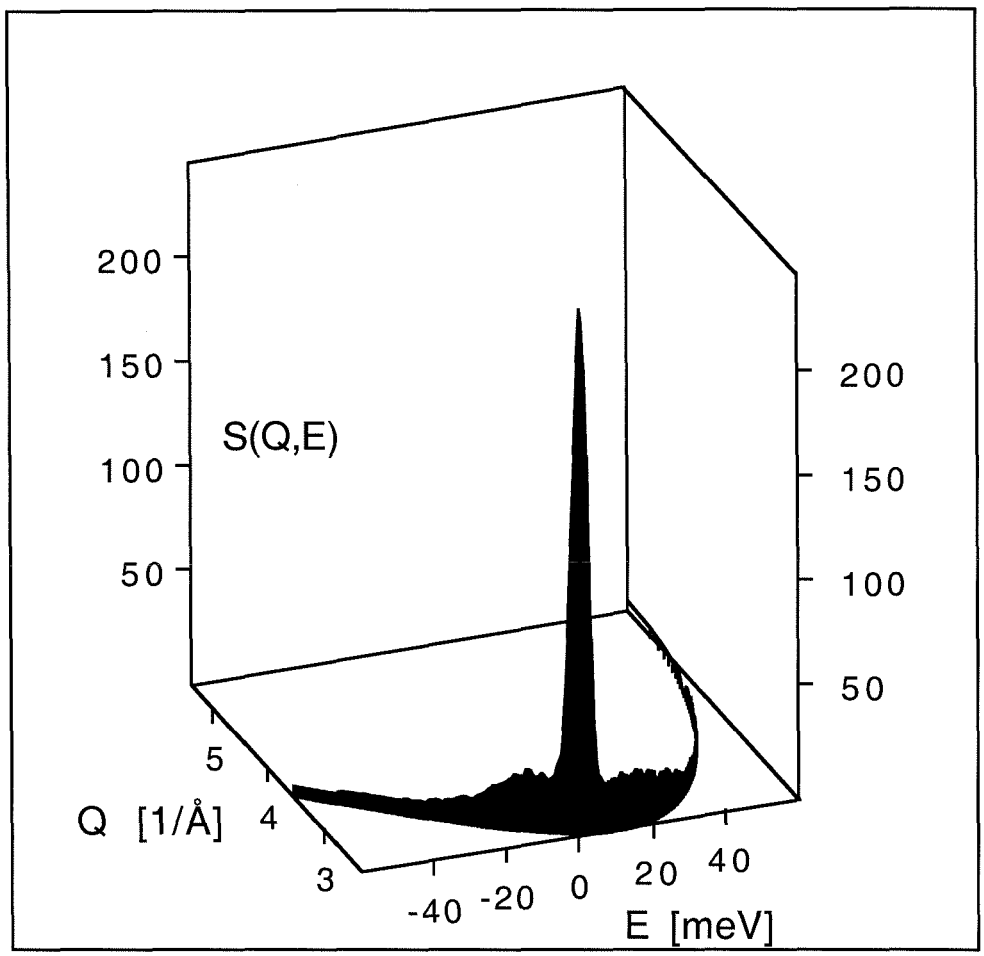

Figure A.4: Scattering surface, S(Q,E), for the third angle-bank of an FeAl sample containing 2% vacancies. Data taken on LRMECS spectrometer at IPNS. The incident energy is 60 meV.

The scattering to the left and right-hand sides of the elastic peak represent neutrons that have either gained or lost energy during the scattering process. The signal is larger from the right-hand side of the elastic peak (positive energy-loss) because it is easier for monochromatic neutrons to lose energy to a phonon than it is for a phonon to impart energy to the incident neutrons. Because of the far superior signal in the positive energy-loss portion of the data, we confine our data analysis to this region only.

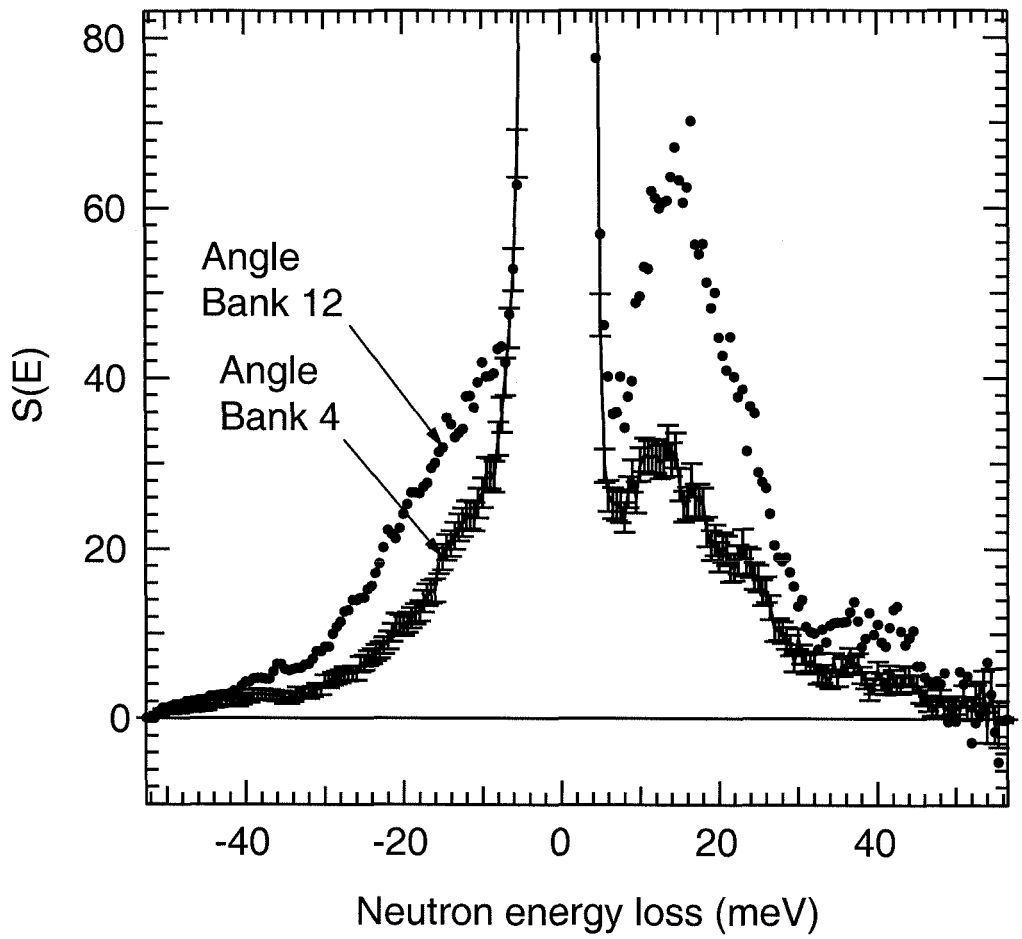

Figure A.5: Neutron data (background corrected) from the twelfth and fourth anglebanks of the LRMECS TOF spectrometer. The sample is chemically ordered B2 FeAl, with a 2% vacancy concentration. Incident neutron energy is 60 meV.

A.2 Data Analysis

Proceeding from the scattering surface data taken by the TOF spectrometer to the phonon DOS is a multi-step, iterative procedure. In figure A.6 we illustrate the process in a flowchart.

One must have at least two and optionally three data sets in order to proceed reliably with the data analysis. First, the inelastic TOF spectra of the sample must be measured. Second, some sort of background spectra must be measured, at conditions that are close as possible to the conditions present when the sample data was taken. At the LRMECS spectrometer, this is usually accomplished by removing the sample from the Al sample can and recording the resultant TOF spectra. One

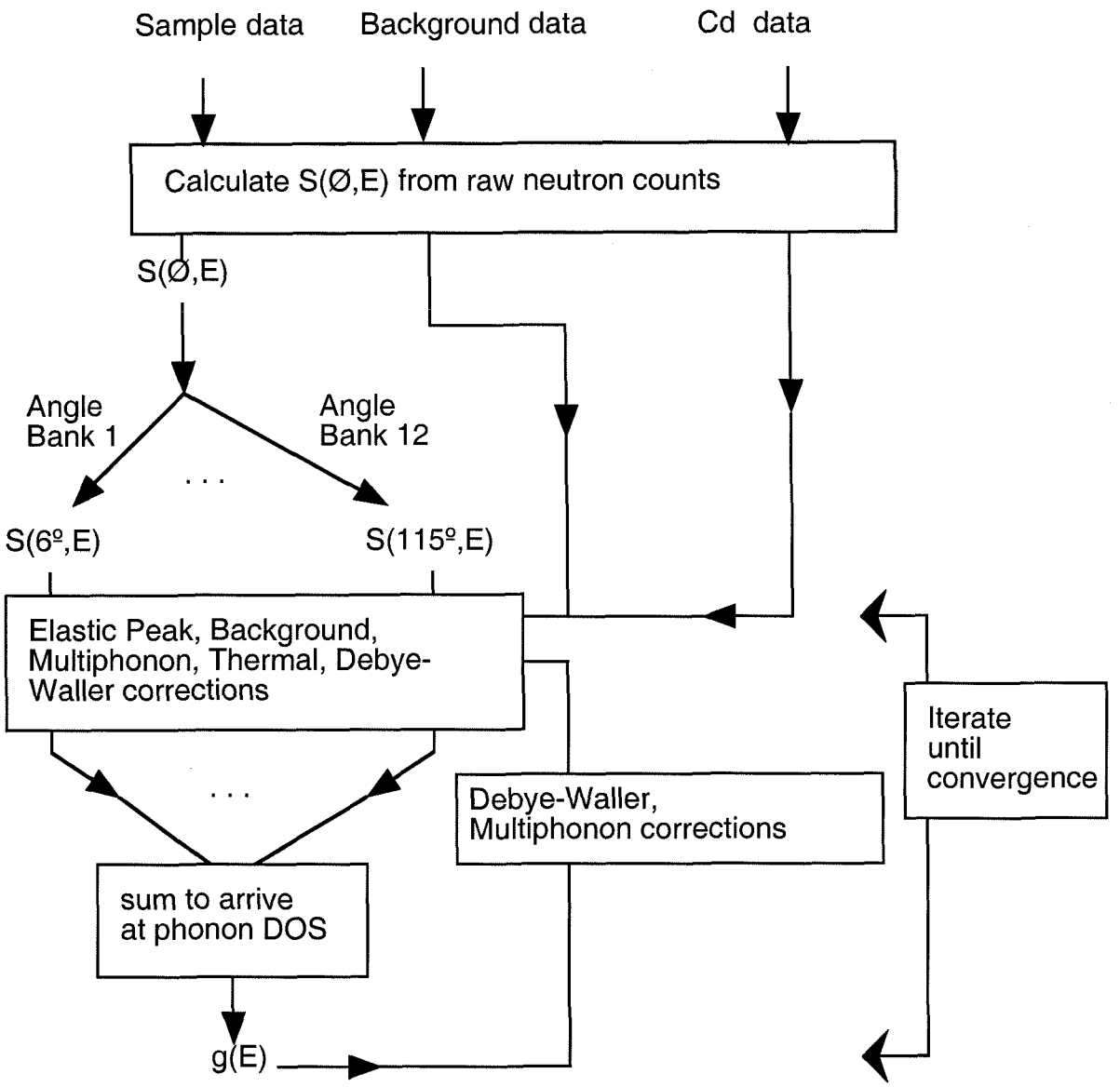

Figure A.6: Neutron data analysis flowchart. Data analysis proceeds from the raw neutron counts (top of the chart) to the phonon DOS (bottom of the chart).

can improve upon the background correction by taking a TOF spectra of a 100% absorbing sample. At the LRMECS spectrometer, this is usually accomplished by replacing the sample with a plate of Cd, which is completely opaque to thermal neutrons. The sample, empty-can and Cd data are transformed from the raw counts to their $S(\phi, E)$ representation, which also adjusts the raw neutron counts for variations in detector effeciencies. This step is performed on LRMECS data using the iliad code, written and maintained by Ray Osbourne. The iliad code also transforms the 3-dimensional surface representation of the scattering spectra into a more practical group of two-dimensional data sets. Each data set represents a constant-angle "slice" of the scattering surface, where the slice sums the neutron counts over a ten-degree scattering angle.

A.3 Background Correction

Once the data has been transformed into the $S(\phi, E)$ representation, the background corrections can be performed. The simplest background correction simply subtracts the empty-can data, S_{bg}, from the sample data, S_{sample}.

$$S_{cor} = S_{sample} - S_{bg} \tag{A.3}$$

This procedure is an over-correction, since the background with the sample in place is somewhat smaller than the measured background. The background counts are proportional to the incident neutron flux, but the sample absorbs and scatters a certain percentage of the incident neutrons. Thus the true background counts can be approximated by attenuating the measured background by an amount equal to the scattering strength of the sample

$$S_{cor} = S_{sample} - (1 - f)S_{bg} \tag{A.4}$$

where f is the percentage of the incident neutron flux that the sample scatters and absorbs. Typical values for f are between 0.05 and 0.1. This procedure is adequate

but can be improved upon. We can divide the background counts into two types: originating from scattering before the sample and after the sample. Background counts of the former type do not undergo the (1–f) attenuation shown in equation A.4. Background counts of the latter type do undergo the (1–f) attenuation. The Cd background measurement allows us to separate the latter from the former. Using the Cd data, we calculate the background correction as

$$S_{cor} = S_{sample} - (1 - f)\{S_{bg} - S_{Cd}\} - S_{Cd} \tag{A.5}$$

where S_{Cd} is the scattering from the Cd run. In practice, the Cd signal is near zero, so the corrections A.4 and A.5 are identical. It is more important to calculate f correctly for each angle-bank, which requires knowing the thickness and geometry of the specimen.

Before the phonon DOS can be derived from the data, the multi-phonon scattering contribution must be subtracted from the data. The multi-phonon scattering increases with temperature and κ. Multi-phonon scattering arises when more than one-phonon participates in a single neutron-scattering event. The multi-phonon scattering can be calculated from the phonon DOS. We use an iterative procedure to arrive at both the multi-phonon contribution and the phonon DOS, where the phonon DOS is used to calculate the multi-phonon scattering and then the new phonon DOS. This procedure is iterated until convergence. We calculate the multi-phonon scattering within the incoherent, virtual-crystal approximation. This is the only approach possible without detailed knowledge of the lattice dynamics of the crystal. We explain this method below.

A.4 Thermal and Multiphonon Corrections

The partial differential cross-section for a harmonic Bravais lattice is given in the incoherent approximation as [61, 60]

$$\left(\frac{\partial^2\sigma}{\partial\Omega\partial E}\right)^{inc} = \frac{\sigma_{inc}}{4\pi}\frac{k'}{k}\frac{N}{2\pi\hbar}e^{-2W}\int e^{\langle UV\rangle}e^{(-i\omega t)}dt\ , \qquad (A.6)$$

where $U = -i\kappa\cdot\mathbf{u}(0)$ and $V = i\kappa\cdot\mathbf{u}(t)$. The variables $\mathbf{u}(t)$, σ_{inc}, k', k, N, W, and $E = \hbar\omega$ are, respectively, the atomic displacement from equilibrium at time t, incoherent scattering cross-section, final and initial neutron wave-vector magnitudes, number of atoms in the crystal, Debye-Waller factor and energy transfer. Although the one-phonon expansion of equation A.6 is a good approximation for small momentum transfer, the higher order multi-phonon terms cannot be neglected at higher scattering vectors, where the incoherent approximation is more reliable. The TOF spectra were measured at constant scattering angle, not constant scattering vector. The scattering vector therefore varies with energy transfer, and this dependence is different for each angle bank. Evaluating equation A.6 while retaining the dependence of κ on ω, the following expression is obtained for the incoherent inelastic n-phonon double-differential scattering cross-section:

$$\left(\frac{\partial^2\sigma}{\partial\Omega\,\partial E}\right)^{inc}_{n-phonon} = \frac{\sigma_{inc}}{4\pi\hbar}\frac{k'}{k}\frac{N}{n!}e^{-2W}\left(\frac{3\hbar}{2m}\right)^n[P(\omega)]^{n-convolution}\ , \qquad (A.7)$$

where m denotes the mass of the scatterer,

$$P(\omega) = \frac{\langle(\kappa\cdot\mathbf{e}_s)^2\rangle_\omega}{\omega}g(\hbar\omega)\langle n_\omega + 1\rangle + \frac{\langle(\kappa\cdot\mathbf{e}_s)^2\rangle_{-\omega}}{-\omega}g(-\hbar\omega)\langle n_{-\omega}\rangle\ , \qquad (A.8)$$

and

$$\left(\frac{\partial^2\sigma}{\partial\Omega\,\partial E}\right)^{inc}_{inelastic} = \sum_{n=1}^{\infty}\left(\frac{\partial^2\sigma}{\partial\Omega\,\partial E}\right)^{inc}_{n-phonon}\ . \qquad (A.9)$$

The index s specifies a single vibrational mode and the notation $\langle\ldots\rangle_\omega$ denotes an average over all vibrational modes with frequency ω. The variable $\mathbf{e}_s$ is the phonon polarization vector of mode s. The function g is, as usual, the normalized phonon DOS. The notation $[f]^{n-convolution}$ specifies the sequential convolution of n instances of the function f. For example,

$$[\mathrm{P}(\omega)]^{1-\mathrm{convolution}} \equiv \mathrm{P}(\omega) \tag{A.10}$$

and

$$[\mathrm{P}(\omega)]^{2-\mathrm{convolution}} = \int_{-\infty}^{\infty} \mathrm{P(x)P}(\omega - \mathrm{x})\mathrm{dx}. \tag{A.11}$$

The term $\langle(\kappa \cdot \mathbf{e}_s)^2\rangle_\omega$ simplifies to $\frac{1}{3}\kappa(\omega)^2$ for a crystal with cubic symmetry, which was the case for all our samples.

As is seen from equation A.7, the phonon DOS is obtained easily from the 1-phonon cross-section. The latter was derived in an iterative process from the measured spectra by evaluating equation A.7 for the 1–5-phonon contributions, fitting their sum [equation A.9] to the corrected data and subtracting the 2–5 multi-phonon contributions from the spectrum. In figure A.7 we show the 2–5 and 1–5 phonon fits to the S(E) spectrum, at the twelfth angle-bank, for an FeAl sample at 300 K.

The 2–5 phonon contributions, collectively known as the multiphonon scattering, are considerable at room temperature. It is sufficient to sum the multiphonon scattering to 5-phonon events since the n-phonon scattering rapidly goes to zero for large n. The 1–5 phonon contribution as calculated using equation A.7 fitted remarkably well the TOF spectra shown in figure A.7. This is surprising for a model which assumes a single mass and scattering factor for an average atom, as well as neglecting the coherent-scattering entirely. Nevertheless, since the multiphonon scattering is essentially featureless, the above procedure yields a sufficiently accurate correction for multiphonon scattering.

The remaining intensity was then corrected for the elastic-peak, thermal and Debye-Waller factors. Mean square displacements (for use in the Debye-Waller factor) are calculated self-consistently. The sum of the corrected intensities from all 12 angle banks gives the phonon DOS. By summing over the angle banks, we ensure that a large portion of reciprocal space is sampled at each phonon energy. This is necessary in order to account for any coherent-scattering present in the sample. For a sample that exhibits purely incoherent scattering, the entire TOF spectra is redundant. In

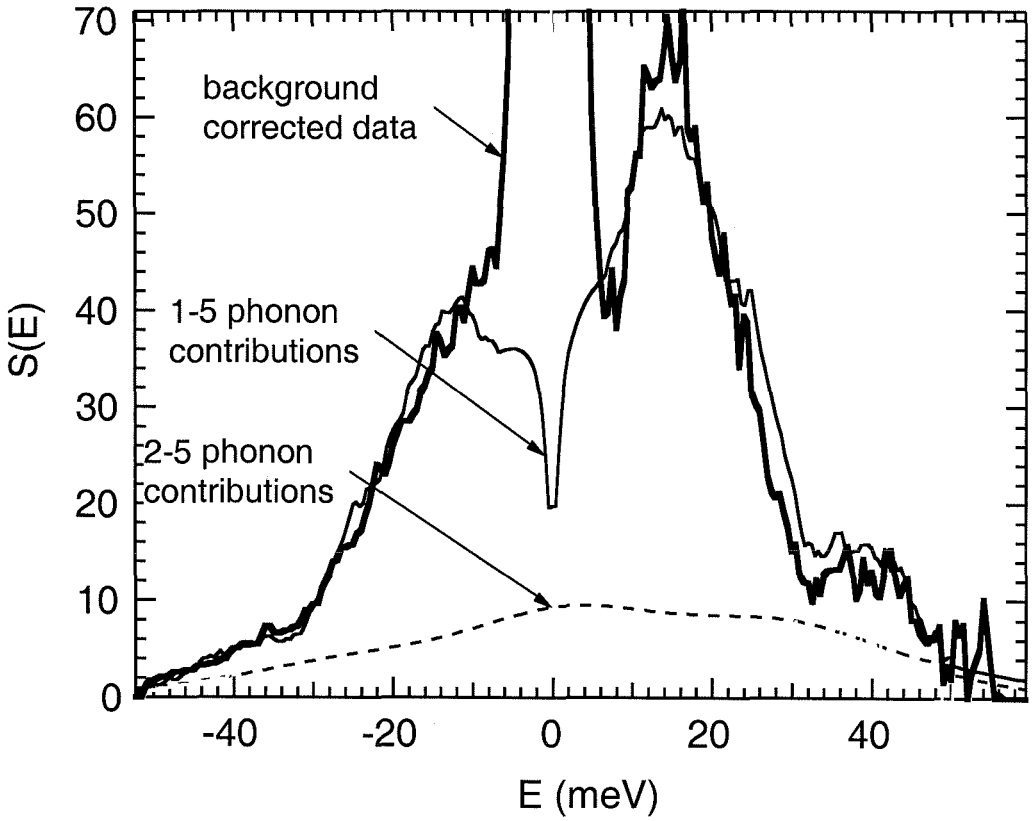

Figure A.7: S(E), 2–5 phonon and 1–5 phonon fits to neutron scattering spectra of 12^{th} angle bank of an FeAl sample containing 2% vacancies. The 1–5 and 2–5 phonon contributions are calculated self consistently using equation A.7.

this case, equation A.7 involves no approximations and the phonon DOS can be independently derived from each angle-bank spectra. Most samples exhibit significant coherent-scattering, which requires the phonon DOS to be extracted by averaging (or summing) the contributions from each angle-bank.

The resulting phonon DOS was then used to re-evaluate equation A.7 to obtain the multiphonon scattering and Debye-Waller factor. This procedure is iterated until the DOS, multi-phonon and Debye-Waller factors converge. The first iteration can be calculated by ignoring the multi-phonon scattering and providing a suitable guess for the Debye-Waller factor.

A.5 Neutron-Weight Corrections

Strictly speaking, the phonon DOS arrived at using the procedure outlined above and in figure A.6 is not the true phonon DOS, but rather the neutron-weighted DOS. The neutron-weighted DOS is identical with the phonon DOS for an elemental scatterer. This is not the case for a sample that contains more than one type of atom, or scatterer. The neutron-weighted phonon DOS is rigorously defined in equation 3.2, which is provided again here:

$$g_{NW}(E) \propto \sum_{d} g_d(E) \exp(-2W_d) \exp(2W) \frac{\sigma_d}{m_d} \tag{A.12}$$

where $\exp(-2W_d)$,σ_d and m_d are the Debye-Waller factor, total scattering cross-section and mass of atom d. The Debye-Waller factor is an explicit function of $g_d(E)$. The term $\exp(2W)$ is the average Debye-Waller correction; this is calculated from the self-consistent neutron-weighted DOS. The factor $\exp[2(W - W_d)]$ is approximately unity. For the case where σ_d/m_d is the same for all species d, $g_{NW}(E) \approx g(E)$.

The error introduced by calculating the multi-phonon scattering self-consistently using the neutron-weighted DOS, rather than the true phonon DOS, is small. This can be qualitatively verified by examining how well the 1–5 phonon scattering, as calculated using equation A.7, fits the experimental data. In figure A.7 we observe a good fit between the 1–5 phonon contribution calculated using the neutron-weighted DOS and the experimental data. This agreement raises our confidence in the accuracy of the 2–5 phonon contribution.

Arriving at the true phonon DOS from the neutron-weighted phonon DOS is beyond the scope of this appendix. Various methods have been discussed in chapters 3 and 5, with varing degrees of universality. As we mentioned in section 6.2.3, the neutron-weight correction as well as other approximations involved in the data analysis can be overcome by fitting a dynamics model to the neutron-scattering data directly. Although this approach is both scientifically and computationally demanding, we foresee no better method for extracting the vibrational dynamics from inelastic neutron scattering measurements.

Appendix B Local Cluster Approximation

The local cluster approximation (LCA), and its extension to the cluster variation method, is a technique for modeling ground-state thermodynamic properties of crystals. Although best known for very successfully calculating the correct configurational entropy of ordering [13], the LCA in principle can be used to calculate any lattice property. A lattice property is a property of a solid which is a unique function of the location of all the atoms in the solid. Most lattice properties can be shown to be thermodynamic ground-state variables, including the vibrational entropy. Within the LCA the vibrational entropy S_{vib} can be represented by

$$S_{vib} = S_0 + S_1 \sum_{\sigma_1} \phi(\sigma_1) + S_2 \sum_{\sigma_2} \phi(\sigma_2) + S_3 \sum_{\sigma_3} \phi(\sigma_3) + \dots \tag{B.1}$$

where the S_i are the cluster coefficients associated with cluster i, σ_i is the i^{th} cluster type and $\phi(\sigma_i)$ is the spin-product over cluster σ_i. Examples of clusters are single atoms, all first-neighbor-neighbor pairs, all second-nearest-neighbor pairs or all first-nearest-neighbor tetrahedrons. The function ϕ is a multiplicative spin-product over a particular cluster of type σ_i

$$\phi(\sigma) = \prod_{j=1}^{N} \lambda_j \tag{B.2}$$

where there are N atoms in cluster σ and λ_j is the spin value associated with the j^{th} atom in cluster σ. For the case of a binary alloy, we let species A have spin $+1$ and species B have spin -1. The spin product ϕ of a first-nearest-neighbour cluster would have four possible values because there are four ways to occupy a first-nearest neighbour pair in a binary alloy: $(-1)(-1), (-1)(+1), (+1)(+1)$ and $(+1)(-1)$. These products are twofold degenerate, and ϕ would either be $+1$ or -1, depending on the

occupancy of the pair cluster. In general, for a binary alloy, ϕ is one of two values, -1 or $+1$, for any arbitrary occupancy of any arbitrary cluster.

The summations $\sum_{\sigma_i} \phi$ in equation B.1 are over all clusters of type σ_i in the crystal. For the case of $\sum_{\text{point}} \phi(\text{point})$, where "point" is the single atom cluster, this sum is identically zero for a binary alloy of composition 50%. This can be shown in the following fashion: The spin-product ϕ takes on the value -1 for atom A and $+1$ for atom B. We sum ϕ over all point clusters in the crystal. Every point cluster is simply every atom, and thus the sum $\sum_{\text{point}} \phi(\text{point})$ equals $(N/2)(-1) + (N/2)(+1) = 0$, where N is the number of atoms in the crystal. For a binary alloy of composition 75%, this same sum would be $-\frac{N}{2}$, and for 25% it is $+\frac{N}{2}$.

The cluster coefficients S_i do not depend on the occupancy of the cluster, but vary as a function of cluster type. For temperature or pressure dependent data, we allow S_i to depend on temperature and pressure. The coefficients S_i are the variable parameters in the LCA, and they are to be solved for or fitted to, depending on the model.

The equality in equation B.1 is exact if we allow the right-hand side to sum over all possible clusters in the crystal. In practice, we cut off the summation at some finite cluster size and thus arrive at a "cluster approximation" or "cluster expansion." When we are solving for the coeffecients S_i, we introduce error into the values of these parameters by truncating the sum at some finite cluster size. The power of the LCA is in the quick convergence of the right-hand side of equation B.1; however, fast convergence requires an intelligent guess of the clusters that contribute most significantly to the sum. This guess is facilitated by a strong connection between the individual elements of the LCA sum and our physical intuition about the lattice property in question. For most lattice properties, short-range physical interactions predominate, with longer-range interactions contributing less. Within the LCA model this means that smaller, more localized clusters are more important than larger, more diffuse clusters. For this reason, the LCA always includes terms for the point and first-nearest neighbour pair. Typical additional clusters are the first-nearest neighbour triplet and tetrahedra.

For the case of the vibrational entropy, it is unclear how quickly the LCA converges. The vibrational entropy depends on the energies of the phonons in a crystal, and phonons are notoriously long-ranged excitations. A typical high-quality Born-von Kármán model of an elemental metal will have significant force interactions between sixth-nearest neighbour (or farther) pairs. There is reason to hope that the vibrational *entropy*, however, can be expressed accurately with clusters of smaller size than the range of the force constants needed in a Born-von Kármán model [14].

Bibliography

[1] V. Sears, E. Svensson, and B. Powell, Canadian Journal of Physics **73**, 726 (1995).

[2] G. Grimvall and J. Rosén, International Journal of Thermophysics **4**, 139 (1983).

[3] A. V. Langeveld and J. Neimantsverdriet, Surface Science **178**, 880 (1986).

[4] S. J. Clark and G. J. Ackland, Physical Review B **48**, 10899 (1993).

[5] T. B. Massalski, P. R. Hiroaki Okamoto, and L. K. Subramanian, editors, *Binary Alloy Phase Diagrams*, Second ed. (ASM Int., Materials Park, OH, 1990).

[6] M. E. Manley, *From Elementary Excitations to Microstructures: The thermodynamics of metals and alloys across length scales*, PhD dissertation, California Institute of Technology, Materials Science, 2001.

[7] O. Eriksson, J. M. Wills, and D. C. Wallace, Physical Review B **46**, 5221 (1992).

[8] E. G. Moroni, G. Grimvall, and T. Jarlborg, Physical Review Letters **76**, 2758 (1996).

[9] V. Ozolins and M. Asta, Physical Review B **86**, 448 (2001).

[10] V. Ozolins, C. Wolverton, and A. Zunger, Physical Review B **58**, 5897 (1998).

[11] D. C. Wallace, *Thermodynamics of Crystals* (Dover, Mineola, New York, 1998).

[12] J. M. Sanchez and D. de Fontaine, Physical Review B **17**, 2926 (1978).

[13] R. Kikuchi, Physical Review **81**, 988 (1951).

[14] A. van de Walle and G. Ceder, Physical Review B **61**, 5972 (2000).

[15] F. Ducastelle, *Order and Phase Stability in Alloys*, Cohesion and Structure Vol. 3 (Elsevier Science Publishers, Amsterdam, 1991).

[16] N. Saunders and A. P. Miodownik, Materials Science and Technology **4**, 768 (1988).

[17] H. J. Fecht, M. X. Zhang, Y. A. Chang, and J. H. Perepezko, Metallurgical Transactions A **20A**, 795 (1989).

[18] L. Kaufman and B. Ditchek, Journal of Less-Common Metals **168**, 115 (1991).

[19] R. Bormann and K. Zoltzer, Physics Status Solidi **131**, 691 (1992).

[20] E. Ising, Zitschrift fir Physik **31**, 253 (1925).

[21] W. L. Bragg and E. J. Williams, Proc. Royal. Soc. A **145**, 699 (1934).

[22] W. L. Bragg and E. J. Williams, Proc. Royal Soc. A **151**, 540 (1935).

[23] D. de Fontaine, Solid State Physics **34**, 73 (1979).

[24] A. G. Khachaturyan, *Theory of Structural Transformations in Solids* (John Wiley and Sons, Inc., New York, 1983).

[25] K. Terakura, T. Oguchi, T. Mohri, and K. Watanabe, Physical Review B **35**, 2169 (1987).

[26] A. A. Mbaye, L. G. Ferreira, and A. Zunger, Physical Review Letters **58**, 49 (1987).

[27] M. Sluiter, D. de Fontaine, R. Guo, X. Q.and Podloucky, and A. J. Freeman, Physical Review B **42**, 10460 (1990).

[28] C. Booth and J. S. Rowlinson, Transanctions of the Faraday Society **51**, 463 (1955).

[29] P. J. Wojtowcz and J. G. Kirkwood, Jour. Chem. Physics **33**, 1299 (1960).

[30] H. Bakker, Philosophical Magazine A **45**, 213 (1982).

[31] H. Bakker and C. Tuijn, Journal of Physics C **19**, 5585 (1986).

[32] J. M. Sanchez, J. P. Stark, and V. L. Moruzzi, Physical Review B **44**, 5411 (1991).

[33] A. F. Guillermet and G. Grimvall, J. Phys. Chem. Solids **53**, 105 (1992).

[34] J. Okamoto, C. Ahn, and B. Fultz, Temperature-dependent EXELFS of Al K and Fe L23 edges in chemically disordered and D03 ordered Fe_3Al, in *Microbeam Analysis*, edited by J. Michael and P. Ingram, p. 56, San Francisco Press, 1990.

[35] L. Anthony, J. K. Okamoto, and B. Fultz, Physical Review Letters **70**, 1128 (1993).

[36] L. Anthony, L. J. Nagel, J. K. Okamoto, and B. Fultz, Physical Review Letters **73**, 3034 (1994).

[37] L. Nagel, L. Anthony, and B. Fultz, Philosophical Magazine Letters **72**, 421 (1995).

[38] B. Fultz, L. Anthony, L. J. Nagel, R. M. Nicklow, and S. Spooner, Physical Review B **52**, 3315 (1995).

[39] B. Fultz *et al.*, Physical Review B **52**, 3280 (1995).

[40] G. D. Garbulsky and G. Ceder, Physical Review B **49**, 6327 (1994).

[41] J. D. Althoff, D. Morgan, D. de Fontaine, M. Asta, and S. M. Foiles, Physical Review B , R5705 (1997).

[42] R. Ravelo *et al.*, Physical Review B **57**, 862 (1998).

[43] S. R. Harris, D. H. Pearson, C. M. Garland, and B. Fultz, J. Mater. Res. **6**, 2019 (1991).

[44] S. Gialanella, S. B. Newcomb, and R. W. Cahn, *Ordering and Disordering in Alloys* (Elsevier Applied Science, London, 1992).

[45] F. Cardellini, C. Fabrizio, G. Mazzone, A. Montone, and V. Rosato, J. Mater. Res. **8**, 2504 (1993).

[46] G. F. Zhou, M. J. Zwanenburg, and H. Bakker, J. Appl. Phys. **78**, 3438 (1995).

[47] L. Nagel, L. Anthony, J. K. Okamoto, and B. Fultz, Journal of Phase Equilibria **18**, 551 (1997).

[48] W. G. Stirling, R. A. Cowley, and M. W. Stringfellow, Journal of Physics F **2**, 421 (1972).

[49] D. M. Paul, R. A. Cowley, and B. W. Lucas, Journal of Physics F **9**, 39 (1979).

[50] C. Stassis, F. X. Kayser, C.-K. Loong, and D. Arch, Physical Review B **24**, 3048 (1981).

[51] P. H. Dederichs, H. Schober, and D. J. Sellmyer, *Metals: Phonon States, Electron States and Fermi Surfaces*, Landolt-Börnstein Numerical Data and Functional Relationships in Science and Technology Vol. III/13a (Springer-Verlag Berlin, New York, 1981).

[52] E. Fawcett, R. Griessen, W. Joss, and W. Kress, *Metals: Phonon States, Electron States and Fermi Surfaces*, Landolt-Börnstein Numerical Data and Functional Relationships in Science and Technology Vol. III/13b (Springer-Verlag Berlin, New York, 1983).

[53] I. M. Robertson, Solid State Communications **53**, 901 (1985).

[54] M. Mostoller *et al.*, Physical Review B Condensed Matter **40**, 2856 (1989).

[55] Y. Noda, Y. Endoh, S. Katano, and M. Iizumi, Physica B & C **120**, 317 (1983).

[56] S. Katano, M. Iizumi, and Y. Noda, Journal Of Physics F Metal Physics **18**, 2195 (1988).

[57] L. Anthony, L. Nagel, and B. Fultz, Vibrational entropy differences in intermetallic compounds from phonon densities of states, in *Solid-Solid Phase Transformations The Minerals, Metals & Materials Society*, edited by W. Johnson, J. Howe, D. Laughlin, and W. Soffa, 1994.

[58] Y. Noda and Y. Endoh, Journal of the Physical Society of Japan **57**, 4225 (1988).

[59] I. M. Robertson, Journal of Physics: Condensed Matter **3**, 8181 (1991).

[60] W. Marshall and S. W. Lovesey, *Theory of Thermal Neutron Scattering* (Clarendon Press, Oxford, 1971).

[61] G. L. Squires, *Introduction to the Theory of Thermal Neutron Scattering* (Dover Publications, Inc., New York, 1978).

[62] W. Hume-Rothery and G. V. Raynor, *The Structure of Metals and Alloys* (Institute of Metals, London, 1962).

[63] A. Miedema, Philips Technical Review **36** (1976).

[64] A. Miedema, F. de Boer, and R. Boom, CALPHAD **1**, 341 (1977).

[65] A. Miedema, P. de Chatel, and F. de Boer, Physica **100B**, 1 (1980).

[66] D. Pettifor, *Bonding and structure of molecules and solids* (Clarendon Press, Oxford, 1995).

[67] C. Bechman, W. Wallace, and R. Craig, Philosophical Magazine **27**, 1249 (1973).

[68] M. Podgorny, Physical Review B **43**, 11300 (1991).

[69] P. Villars and L. Calvert, *Pearson's Handbook of Crystallographic Data for Intermetallic Phases*, 2 ed. (ASM International, Materials Park, OH, 1991).

[70] A. Kashyap, T. Nautiyal, and S. Auluck, Physica B **193**, 248 (1994).

[71] K. Tanaka and M. Koiwa, Intermetallics **4**, S29 (1996).

[72] B. Fultz, T. A. Stephens, W. Sturhahn, W. Toellner, and E. E. Alp, Physical Review Letters **80**, 3304 (1998).

[73] E. Teatum, J. K.A. Gschneidner, and J. Waber, Los Alamos Scientific Laboratory of the University of California Report No. LA-4003, 1968 (unpublished).

[74] C. Kittel, *Introduction to Solid State Physics*, 7 ed. (John Wiley & Sons, Inc., New York, 1996).

[75] Y. Touloukian, R. K. Kirby, R. E. Taylor, and P. D. Desai, editors, *Thermal Expansion: Metallic Elements and Alloys*, Thermophysical Properties of Matter Vol. 12 (IFI/Plenum, New York, 1975).

[76] G. Michal and R. Sinclair, Acta Crysta. **B37**, 1803 (1981).

[77] P. McCormick and Y. Liu, Acta Metallurgica et Materialia **42**, 2407 (1994).

[78] G. Johari, J. McAnanama, and G. Sartor, Philosophical Magazine B **74**, 243 (1996).

[79] E. Obradó, L. Manosa, and A. Planes, Physical Review B **56**, 20 (1997).

[80] P. Moine, J. Allain, and B. Renker, Journal Of Physics F: Metal Physics **14**, 2517 (1984).

[81] S. Satija and S. Shapiro, Physical Review B **29**, 6031 (1984).

[82] H. Tietze, M. Mullner, and B. Renker, Journal of Physics C: Solid State Physics **17**, L529 (1984).

[83] H. Tietze, M. Mullner, P. Selgert, and W. Assmus, Journal of Physics F: Metal Physics **15**, 263 (1985).

[84] G. Herget, M. Mullner, J. B. Suck, R. Schmidt, and H. Wipf, Europhysics Letters **10**, 49 (1989).

[85] Y. Touloukian and E. Buyco, editors, *Specific Heat: Metallic Elements and Alloys*, Thermophysical Properties of Matter Vol. 4 (IFI/Plenum, New York, 1970).

[86] G. Airoldi, G. Bellini, and C. Difrancesco, Journal Of Physics F: Metal Physics **14**, 1983 (1984).

[87] D. Li, X. Wu, and T. Ko, Philosophical Magazine A **63**, 603 (1991).

[88] P. Bogdanoff, B. Fultz, and S. Rosenkranz, Physical Review B **60**, 1 (1999).

[89] G. L. Zhao and B. N. Harmon, Physical Review B **48**, 2031 (1993).

[90] R. Bruinsma, Physical Review B **25**, 2951 (1982).

[91] O. Mercier, K. N. Melton, G. Gremaud, and J. Hagi, Journal of Applied Physics **51**, 1833 (1980).

[92] G. Bihlmayer, R. Eibler, and A. Neckel, Physical Review B **50**, 13113 (1994).

[93] J. Trampenau, W. Petry, and A. Heiming, Physica B **180 & 181**, 363 (1992).

[94] F. Guthoff *et al.*, Physical Review B **47**, 2563 (1993).

[95] T. Makita, A. Nagasawa, Y. Morii, N. Minakawa, and H. Ohno, Physica B **213 & 214**, 430 (1995).

[96] J. Neuhaus, W. Petry, and A. Krimmel, Physica B **234–236**, 897 (1997).

[97] T. Ohba, Phase Transitions **69**, 289 (1999).

[98] A. Heiming *et al.*, Physical Review B **43**, 10948 (1991).

[99] O. L. Anderson, editor, *Equations of State of Solids for Geophysicists and Ceramic Science* (Oxford, New York, 1995).

[100] F. Guthoff, B. Hennion, C. Herzig, W. Petry, and H. Schober, Journal of Physics: Condensed Matter **6**, 6211 (1994).

[101] J. Trampenau, W. Petry, and C. Herzig, Physical Review B **47**, 3132 (1993).

[102] W. Petry *et al.*, Physical Review B **43**, 10933 (1991).

[103] R. S. Carter, D. J. Hughes, and H. Palevsky, Physical Review **104**, 271 (1956).

[104] A. T. Stewart and B. N. Brockhouse, Rev. Mod. Phys. **30**, 250 (1958).

[105] C. M. Eisenhauer, I. Pelah, D. J. Hughes, and H. Palevsky, Physical Review **109**, 1046 (1958).

[106] K. C. Turberfield and P. A. Egelstaff, *Inelastic scattering of neutrons in solids and liquids* (IAEA, Vienna, 1961).

[107] K. C. Turberfield and P. A. Egelstaff, Physical Review **127**, 1017 (1962).

[108] N. A. Chernoplekov, M. G. Zemlyanov, and A. G. Chicherin, Sov. Phys. JETP **16**, 1472 (1963).

[109] M. G. Zemlyanov, Y. M. Kagan, N. A. Chernoplekov, and A. G. Chicherin, *Inelastic scattering of neutrons in solids and liquids* (IAEA, Vienna, 1966).

[110] R. Haas, W. Kley, K. H. Krebs, and R. Rubin, *Inelastic scattering of neutrons in solids and liquids* (IAEA, Vienna, 1963).

[111] I. Pelah *et al.*, *Inelastic scattering of neutrons in solids and liquids* (IAEA, Vienna, 1963).

[112] B. Mozer, K. Otnes, and H. Palevsky, *Lattice Dynamics* (Pergamon Press, Oxford, 1965).

[113] W. Gläser, F. Carvalho, and G. Ehret, *Inelastic scattering of neutrons in solids and liquids* (IAEA, Vienna, 1965).

[114] D. I. Page, Proc. Phys. Soc. **91**, 76 (1967).

[115] M. Kamal, S. S. Malik, and D. Rorer, Physical Review B **18**, 1609 (1978).

[116] H. Frase, B. Fultz, and J. L. Robertson, Physical Review B **57**, 898 (1998).

[117] Y.-Y. Ye, Y. Chen, K.-M. Ho, B. N. Harmon, and P.-A. Lindgard, Physical Review B **58**, 1769 (1998).

[118] P. A. Flinn, G. M. McManus, and J. A. Rayne, Jour. of Chem. Solids **15**, 189 (1960).

[119] D. T. Hawkins and R. Hultgren, J. Chem. Thermodynamics **3**, 175 (1971).

[120] J. W. Lynn, H. G. Smith, and R. M. Nicklow, Physical Review B **8**, 3493 (1973).

[121] E. C. Svensson, B. N. Brockhouse, and J. M. Rowe, Physical Review **155**, 619 (1967).

[122] E. C. Svensson and W. A. Kamitakahara, Canadian Journal of Physics **49**, 2291 (1971).

[123] R. M. Cunningham, L. D. Muhlestein, W. M. Shaw, and C. W. Tompson, Physical Review B **2**, 4864 (1970).

[124] H. Bjerrum Møller and A. R. Mackintosh, Physical Review Letters **15**, 623 (1965).

[125] A. A. Maradudin, E. W. Montroll, G. H. Weiss, and I. P. Ipatova, *Theory of Lattice Dynamics in the Harmonic Approximation*, Solid State Physics Vol. Supplement 3, Second ed. (Academic Press, New York, New York, 1971), section 7, pp. 353–514.

[126] R. J. Elliott and D. W. Taylor, Proc. Roy. Soc. A **296**, 161 (1967).

[127] Rayleigh, *Theory of Sound* (Dover, New York, 1945).

[128] I. M. Lifshitz, J. Phys. USSR **7**, 215 (1943).

[129] I. M. Lifshitz, J. Phys. USSR **7**, 249 (1943).

[130] I. M. Lifshitz, J. Phys. USSR **8**, 289 (1944).

[131] V. Ozolins, Private communication, 2000.

[132] M. E. Manley *et al.*, Phys. Rev. Lett. **86**, 3076 (2001).